ARMY RESEARCH LABORATORY

Introduction to Shaped Charges

by William Walters

ARL-SR-150 **March 2007**

Approved for public release; distribution is unlimited.

NOTICES

Disclaimers

The findings in this report are not to be construed as an official Department of the Army position unless so designated by other authorized documents.

Citation of manufacturer's or trade names does not constitute an official endorsement or approval of the use thereof.

Destroy this report when it is no longer needed. Do not return it to the originator.

Army Research Laboratory
Aberdeen Proving Ground, MD 21005-5069

ARL-SR-150 **March 2007**

Introduction to Shaped Charges

William Walters
Weapons and Materials Research Directorate, ARL

Approved for public release; distribution is unlimited.

REPORT DOCUMENTATION PAGE

Form Approved
OMB No. 0704-0188

Public reporting burden for this collection of information is estimated to average 1 hour per response, including the time for reviewing instructions, searching existing data sources, gathering and maintaining the data needed, and completing and reviewing the collection information. Send comments regarding this burden estimate or any other aspect of this collection of information, including suggestions for reducing the burden, to Department of Defense, Washington Headquarters Services, Directorate for Information Operations and Reports (0704-0188), 1215 Jefferson Davis Highway, Suite 1204, Arlington, VA 22202-4302. Respondents should be aware that notwithstanding any other provision of law, no person shall be subject to any penalty for failing to comply with a collection of information if it does not display a currently valid OMB control number.
PLEASE DO NOT RETURN YOUR FORM TO THE ABOVE ADDRESS.

1. REPORT DATE *(DD-MM-YYYY)*	2. REPORT TYPE	3. DATES COVERED (From - To)
March 2007	Final	September 2006–February 2007

4. TITLE AND SUBTITLE
Introduction to Shaped Charges

5a. CONTRACT NUMBER

5b. GRANT NUMBER

5c. PROGRAM ELEMENT NUMBER

6. AUTHOR(S)
William Walters

5d. PROJECT NUMBER
AH80

5e. TASK NUMBER

5f. WORK UNIT NUMBER

7. PERFORMING ORGANIZATION NAME(S) AND ADDRESS(ES)
U.S. Army Research Laboratory
ATTN: AMSRD-ARL-WM-TC
Aberdeen Proving Ground, MD 21005-5069

8. PERFORMING ORGANIZATION REPORT NUMBER
ARL-SR-150

9. SPONSORING/MONITORING AGENCY NAME(S) AND ADDRESS(ES)

10. SPONSOR/MONITOR'S ACRONYM(S)

11. SPONSOR/MONITOR'S REPORT NUMBER(S)

12. DISTRIBUTION/AVAILABILITY STATEMENT
Approved for public release; distribution is unlimited.

13. SUPPLEMENTARY NOTES

14. ABSTRACT
This report contains a presentation given at the U.S. Army Research Laboratory (ARL) as a 3-hr lecture introducing and presenting the basic principles of the shaped-charge concept. The lectures were given at ARL, Aberdeen Proving Ground, MD, on 8 January and 16 January 2007 for ARL personnel.

15. SUBJECT TERMS
shaped charge, penetration, EFP, liner materials, jet formation, hemispherical liners

16. SECURITY CLASSIFICATION OF:			17. LIMITATION OF ABSTRACT	18. NUMBER OF PAGES	19a. NAME OF RESPONSIBLE PERSON
					William Walters
a. REPORT	b. ABSTRACT	c. THIS PAGE			19b. TELEPHONE NUMBER (*Include area code*)
UNCLASSIFIED	UNCLASSIFIED	UNCLASSIFIED	UL	124	410-278-6062

Standard Form 298 (Rev. 8/98)
Prescribed by ANSI Std. Z39.18

Contents

List of Figures **iv**

1. Introduction **1**

Distribution List **108**

List of Figures

Figure 1. Topics. 1
Figure 2. Topics (continued). 2
Figure 3. Suggested reading. 2
Figure 4. The Munroe effect. 3
Figure 5. The Munroe effect (continued). 3
Figure 6. The lined-cavity effect. 4
Figure 7. The nomenclature for a shaped-charge configuration. 4
Figure 8. Detonation stages of a typical shaped charge. 5
Figure 9. Liner collapse and jet formation. 5
Figure 10. Liner collapse. 6
Figure 11. Collapse of a shaped charge with a hemispherical liner. 6
Figure 12. Collapse of a shaped charge with a hemispherical liner (continued). 7
Figure 13. Collapse of a shaped charge with a hemispherical liner (continued). 7
Figure 14. High-speed camera viewing the collapse of a shaped charge with a conical liner. 8
Figure 15. High-speed camera viewing the collapse of a shaped charge with a conical liner (continued). 8
Figure 16. High-speed camera viewing the collapse of a shaped charge with a conical liner (continued). 9
Figure 17. High-speed camera viewing the collapse of a shaped charge with a conical liner (continued). 9
Figure 18. High-speed camera viewing the collapse of a shaped charge with a conical liner (continued). 10
Figure 19. High-speed camera viewing the collapse of a shaped charge with a conical liner (continued). 10
Figure 20. High-speed camera viewing the collapse of a shaped charge with a conical liner (continued). 11
Figure 21. Collapse of a shaped charge with a conical liner after particulation. 11
Figure 22. Collapse of a shaped charge with a conical liner prior to particulation. 12
Figure 23. The jet from a shaped charge with a hemispherical liner at late times. 12
Figure 24. The jet from a shaped charge with a hemispherical liner at very late times. 13
Figure 25. The effect of apex angle on the jet formation. 13
Figure 26. Shaped-charge liner designs. 14

Figure 27. Shaped-charge liner designs (continued).....14
Figure 28. Waveshaping concepts. 15
Figure 29. Warhead with ogive.....15
Figure 30. Linear and circular lined shaped-charge configurations. 16
Figure 31. Misnomers. 16
Figure 32. Misnomers (continued).....17
Figure 33. Jet temperature references. 17
Figure 34. The family of high-explosive warheads. 18
Figure 35. Wireline perforating-wellbore schematic. 18
Figure 36. Perforator hardware. 19
Figure 37. Perforator types. 19
Figure 38. Jet from a powder liner.....20
Figure 39. Jet from a powder liner (continued). 20
Figure 40. Jet from a powder liner (continued). 21
Figure 41. Geometry of the collapse process.....21
Figure 42. Velocities with respect to a fixed coordinate system. 22
Figure 43. Velocities referred to a coordinate moving with velocity V_1. 22
Figure 44. The Birkhoff theory. 23
Figure 45. Birkhoff's geometry. 23
Figure 46. Relationship between $\vec{V}_o$, the liner collapse velocity, $\vec{V}$ the collapse velocity relative to the collision point, and $\vec{V}_1$ the collision point velocity. 24
Figure 47. The velocities.....24
Figure 48. The jet and slug velocities. 25
Figure 49. Conservation of mass yields as in the steady state theory.....25
Figure 50. Calculation of the collapse angle.....26
Figure 51. Calculation of the collapse angle (continued). 26
Figure 52. Calculation of the collapse angle (continued). 27
Figure 53. Calculation of the collapse angle (continued). 27
Figure 54. The Taylor angle concept. 28
Figure 55. Taylor's geometry. 28
Figure 56. The Taylor angle.....29
Figure 57. Liner collapse. 29
Figure 58. Liner projection angle by the simple Taylor relation (steady) and the unsteady theory. 30

Figure 59. Liner collapse, velocity formulas. 30
Figure 60. Liner collapse, velocity formulas (continued). 31
Figure 61. Turning-angle formulas. 31
Figure 62. Liner acceleration. 32
Figure 63. Liner acceleration (continued). 32
Figure 64. The jet-tip velocity. 33
Figure 65. Extensions of the theory. 33
Figure 66. Radiographs of jets from two typical conical charges. 34
Figure 67. Supersonic wedge collapse, jetless configuration, stiffened gas. 34
Figure 68. Comparison of jets from supersonic and subsonic collapse. 35
Figure 69. Comparison of jets from supersonic and subsonic collapse (continued). 35
Figure 70. The bulk speed of sound. 36
Figure 71. Jetting criterion for plane axisymmetric cases. 36
Figure 72. Jet/no jet curve for wedge collapse of a stiffened gas. 37
Figure 73. Cohesive jet criterion. 37
Figure 74. The 81.3-mm liner. 38
Figure 75. The jet collapse and formation. 38
Figure 76. Liner drawing. 39
Figure 77. Collapse angle vs. liner position. 39
Figure 78. Deflection angle (Phi) vs. liner position. 40
Figure 79. Collapse velocity vs. liner position. 40
Figure 80. Jet formation velocities vs. liner position. 41
Figure 81. Jet velocity vs. liner position. 41
Figure 82. Cumulative jet mass vs. jet velocity. 42
Figure 83. Cumulative KE vs. jet velocity. 42
Figure 84. Cumulative momentum vs. jet velocity. 43
Figure 85. Experimental study of jet formation, objective. 43
Figure 86. Comparison of HELP and EPIC-2 computer code simulations of jet formation from a hemispherical liner charge for the point initiation case at t = 56 μs after detonation. 44
Figure 87. HELP code simulations of jet formation from a hemispherical liner charge for the initiation case at t = 67 μs after detonation. 44
Figure 88. DEFEL code simulation of a thick-pole, tapered-wall, hemispherical liner charge. ..45
Figure 89. Experimental verification. 45

Figure 90. The desired liner. 46
Figure 91. Setup for diffusion bonding of copper-nickel assemblies, temperature is 982 °C, time is 1–3 hr, argon atmosphere. 46
Figure 92. Diffusion-bonded alternately layered copper-nickel cylinder. 47
Figure 93. Finish-machined alternately layered copper-nickel hemisphere. 47
Figure 94. Flash radiograph of the jet from a hemispherical liner. 48
Figure 95. Recovered jet particles from an alternately layered copper-nickel hemispherical liner. 48
Figure 96. Cross section of recovered jet particles from an alternately layered copper-nickel hemispherical liner. 49
Figure 97. Cross section of jet particle from alternately layered copper-nickel hemispherical liner. 49
Figure 98. Cross section of one half of a recovered jet particle from an alternately layered copper-nickel hemispherical shaped-charge liner. 50
Figure 99. Central region of alternately layered copper-nickel hemispherical liner. 50
Figure 100. Conclusion. 51
Figure 101. HELP code simulation of a 42° conical-liner charge, initial liner geometry (top), and jet and slug at 60 µs (center and bottom). 51
Figure 102. Diffusion bonding setup for fabricating alternately layered copper-nickel cones. 52
Figure 103. Finish-machined alternately layered copper-nickel cone. 52
Figure 104. Flash radiograph of the jet from a conical liner. 53
Figure 105. Recovered slug from alternately layered copper-nickel cone. 53
Figure 106. Jet particle from alternately layered copper-nickel cone. 54
Figure 107. Cross section of a jet particle from alternately layered copper-nickel cone. 54
Figure 108. Explosively formed penetrator (EFP) study. 55
Figure 109. EFPs. 55
Figure 110. State-of-the-art copper explosively formed penetrator. 56
Figure 111. Jet/slug velocity vs. liner half angle. 56
Figure 112. The effect of apex angle on the jet formation. 57
Figure 113. Formation types. 57
Figure 114. Heavy vs. light explosive/liner confinement. 58
Figure 115. Rearward-fold liner formation. 58
Figure 116. Rearward-fold liner formation (continued). 59
Figure 117. Forward-fold liner formation. 59
Figure 118. Forward-fold liner formation (continued). 60

Figure 119. Point-focus liner formation....60
Figure 120. Point-focus liner formation (continued)....61
Figure 121. W-fold liner formation....61
Figure 122. W-fold liner formation (continued)....62
Figure 123. W-fold liner formation (continued)....62
Figure 124. Aerostable EFPs....63
Figure 125. A generic EFP charge to form EFPs....63
Figure 126. Ways to form EFPs with star-shaped tail....64
Figure 127. Front and back view of three projectiles produced with an EFP charge caliber 75 mm, explosive composition B, and liner material armco iron....64
Figure 128. Hit precision of EFP with star-shaped tail at 45 m. The displacement was less than 20 cm....65
Figure 129. Multiple liner concepts....65
Figure 130. Liner materials studied at the U.S. Army Ballistic Research Laboratory (BRL)/ARL....66
Figure 131. Shaped-charge liner material as a function of crystal structure....66
Figure 132. Face-centered cubic (FCC)....67
Figure 133. Body-centered cubic (BCC)....67
Figure 134. Alloys tested as shaped-charge liners....68
Figure 135. Hexagonal close packed (HCP)....68
Figure 136. Orthorhombic (Ortho)....69
Figure 137. Amorphous....69
Figure 138. Alloys....70
Figure 139. Alloys (continued)....70
Figure 140. Alloys (continued)....71
Figure 141. Configuration of depleted uranium alloy charges....71
Figure 142. Free-flight radiograph of depleted uranium liners compared to copper (cone angles indicated)....72
Figure 143. Early time collapse of a hemispherical depleted uranium liner....72
Figure 144. Late time collapse of a hemispherical depleted uranium liner....73
Figure 145. Comparison between a copper and a lead-tin eutectic liner....73
Figure 146. Flash radiographs of 60° pure cadmium liners of varied wall thickness, 25 μs after detonation wave reached apex....74
Figure 147. Flash radiographs of 44° pure magnesium liners of varied wall thickness....74
Figure 148. Metallurgical and explosive effects on jets....75

Figure 149. Oxygen-free high-conductivity copper....75
Figure 150. Electrolytic tough-pitch copper....76
Figure 151. The effect of liner grain size on jet breakup (liner 105-mm M456, modified to BRL 81 dimensions)....76
Figure 152. Effect of liner grain size on jet penetration (M456/BRL 81 mm)....77
Figure 153. Effect of liner grain size on jet breakup time....77
Figure 154. Penetration standoff curve....78
Figure 155. The coordinate system....78
Figure 156. Penetration formulations....79
Figure 157. Bernoulli's equation for coordinates moving at velocity U....79
Figure 158. Ideal penetration time (penetration stops as soon as the rear of the jet hits the target)....80
Figure 159. Momentum equation....80
Figure 160. Equating the two expressions....81
Figure 161. The penetration....81
Figure 162. Eichelberger's equation....82
Figure 163. Eichelberger's formula....82
Figure 164. For fully particulated jets....83
Figure 165. Semi-empirical models....83
Figure 166. Pack and Evans....84
Figure 167. Chou....84
Figure 168. Matuska....85
Figure 169. Alekseevski, Sanasaryan, and Sagomonyan....85
Figure 170. Christman and Gehring....86
Figure 171. Doyle and Buchholz....86
Figure 172. The DiPersio, Simon, Merendino model....87
Figure 173. The DiPersio, Simon, Merendino model (continued)....87
Figure 174. The DiPersio, Simon, Merendino model (continued)....88
Figure 175. The DiPersio, Simon, Merendino model (continued)....88
Figure 176. The DiPersio, Simon, Merendino model (continued)....89
Figure 177. The DiPersio, Simon, Merendino model (continued)....89
Figure 178. The Tate model....90
Figure 179. The Walters and Majerus model....90
Figure 180. The Walters and Majerus model (continued)....91

Figure 181. Analytical and experimental penetration vs. standoff curve for aluminum jet impacting a steel target. 91
Figure 182. Experimental and calculated exit velocities for charge type 1. 92
Figure 183. Analytical and experimental penetration vs. standoff curve for a copper jet impacting a steel target. 92
Figure 184. Hole profiles in combination lead-plate, armor-plate targets. The distance from the top of the pile to the top of the armor plate is designated A in the discussion. 93
Figure 185. Predicted penetration vs. a layered target. 93
Figure 186. Compressibility effects. 94
Figure 187. Major factors in the penetration process. 94
Figure 188. Major factors in the penetration process (continued). 95
Figure 189. Types of charges. 95
Figure 190. Diagram of standard shaped charge. 96
Figure 191. Precision shaped-charge performance. 96
Figure 192. Shaped-charge precision assembly. 97
Figure 193. Shaped-charge precision assembly (continued). 97
Figure 194. Shaped-charge precision assembly (continued). 98
Figure 195. The gauging data for the precision and nonprecision charges. 98
Figure 196. Penetration performance of the standard charge. 99
Figure 197. The solution. 99
Figure 198. Metallurgical and explosive effects on jets. 100
Figure 199. Explosive properties. 100
Figure 200. Liner description. 101
Figure 201. Disposition of a shaped charge to be fired in lead plates. 101
Figure 202. Photograph of a stack of lead plates penetrated by a jet from a steel conical liner. The circular plates have been cut after the firing. The 15.5-cm-diameter plates were 1.5 cm thick. 102
Figure 203. Photograph of a stack of plates penetrated by a jet from a steel conical liner. The circular plates, except the last one, have been cut after firing. The plates are alternately lead and steel; the top plate is lead, the next is steel, the third is lead, etc. The 15.5-cm-diameter lead plates were 1.5 cm thick; the 15.35-cm-diameter steel plates were 1.27 cm thick. 102
Figure 204. Plate mass loss. 103
Figure 205. Thin vs. thick plates. 103
Figure 206. Materials table. 104
Figure 207. Materials table (continued). 104

Figure 208. Favorable characteristics of shaped-charge liner materials. 105
Figure 209. Favorable characteristics of shaped-charge jet materials. 105
Figure 210. Shaped-charge jet parameters. 106
Figure 211. Favorable jet characteristics. 106
Figure 212. Favorable jet characteristics (continued). 107

INTENTIONALLY LEFT BLANK.

1. Introduction

This report contains a presentation given at the U.S. Army Research Laboratory (ARL) as a 3-hr lecture introducing and presenting the basic principles of the shaped-charge concept. The lectures were given at ARL, Aberdeen Proving Ground, MD, on 8 January and 16 January 2007 for ARL personnel.

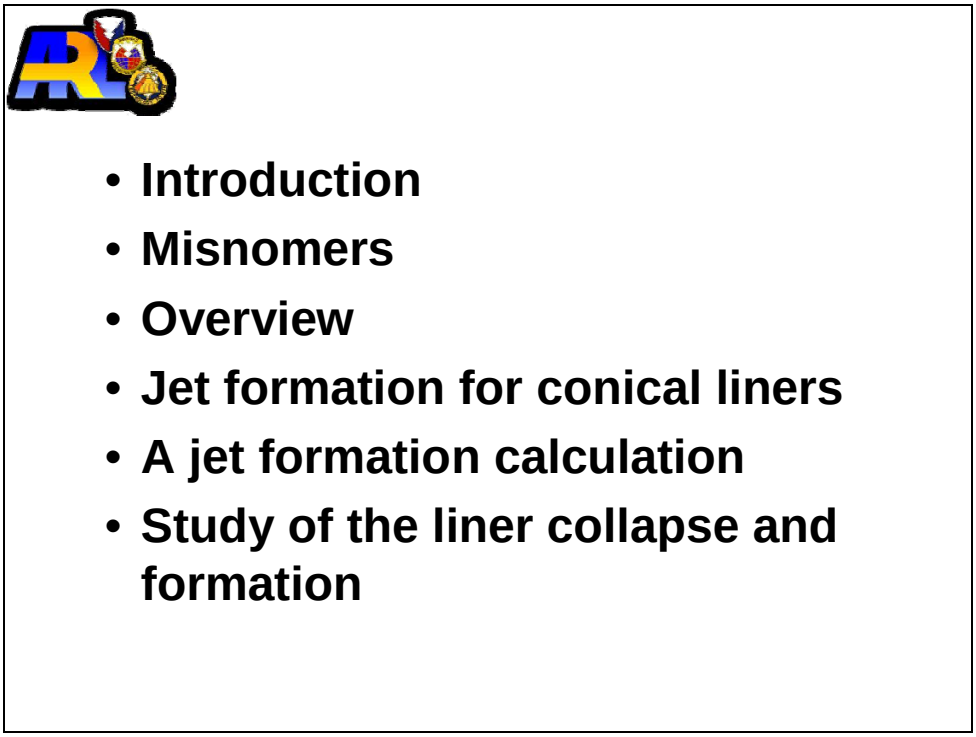

Figure 1. Topics.

- EFPs
- Liner material studies
- The HE fill
- Jet penetration
- Penetration data
- Craters
- Design rules

Figure 2. Topics (continued).

- *Fundamentals of Shaped Charges,* W. Walters and J. Zukas, Wiley, 1989 and soft cover edition with corrections, CMC Press, 1998
- *Tactical Missile Warheads*, Vol. 155 of Progress in Astronautics and Aeronautics. Edited by J. Carleone, AIAA, 1993.

Figure 3. Suggested reading.

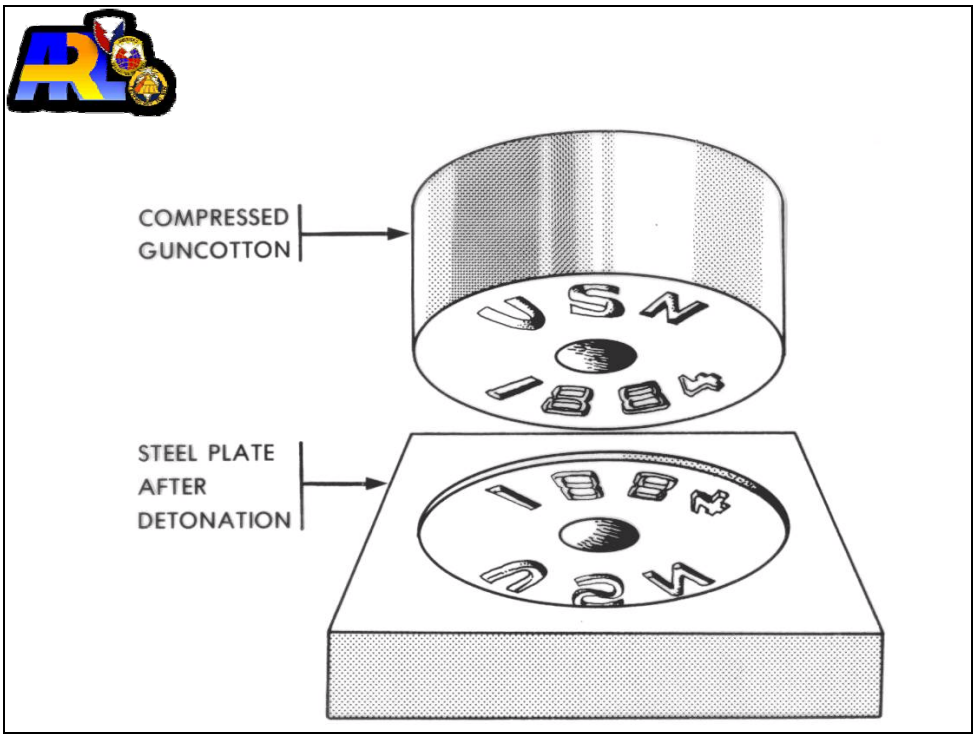

Figure 4. The Munroe effect.

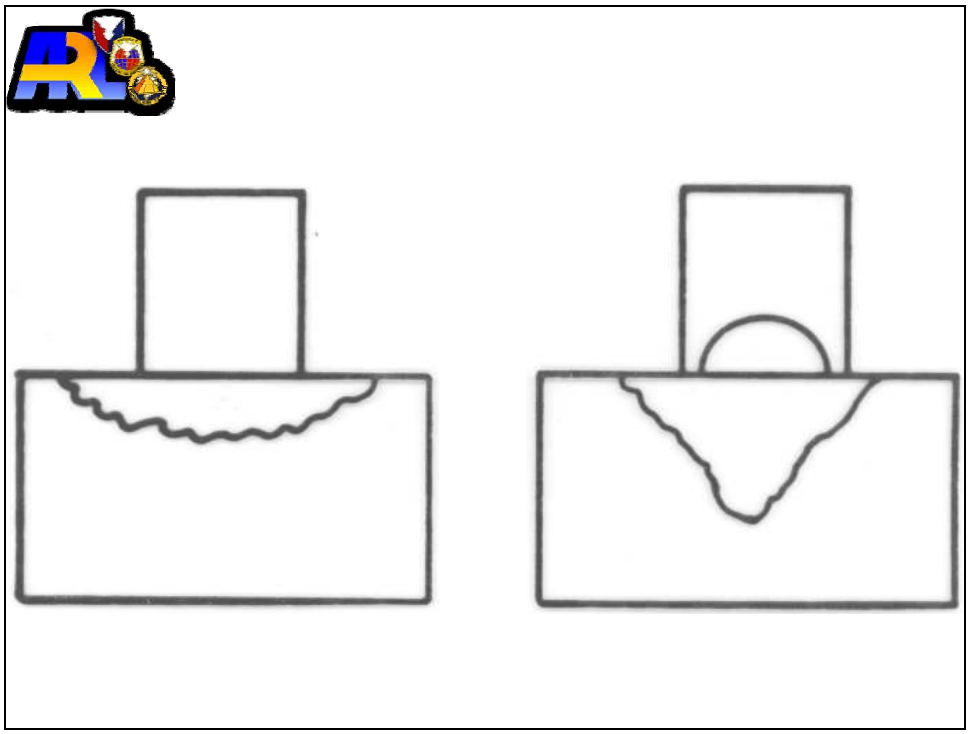

Figure 5. The Munroe effect (continued).

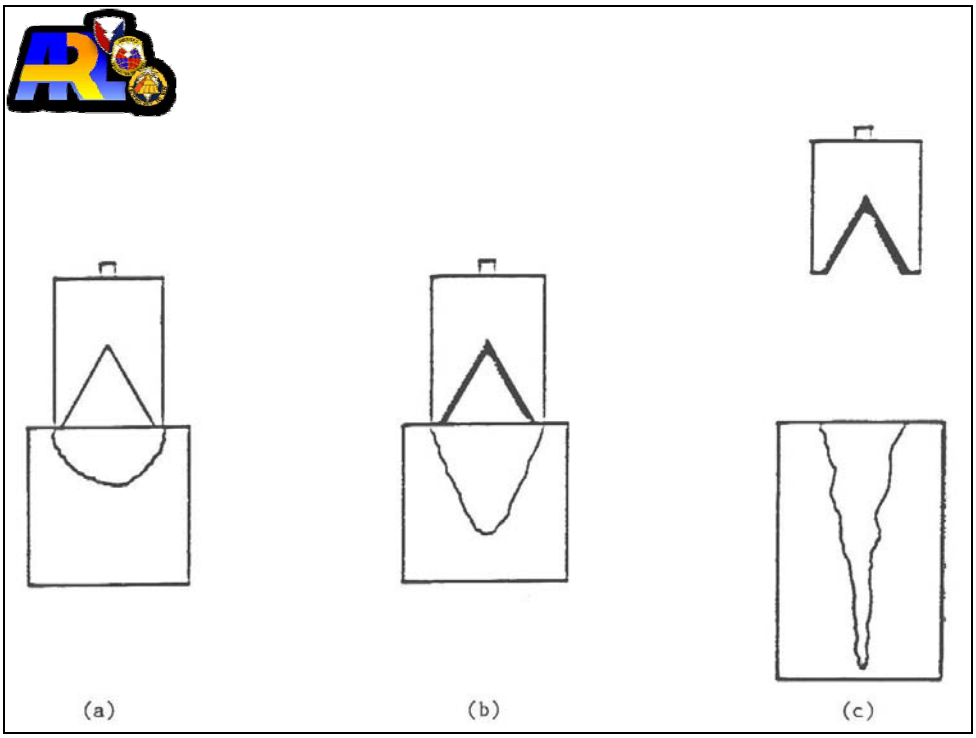

Figure 6. The lined-cavity effect.

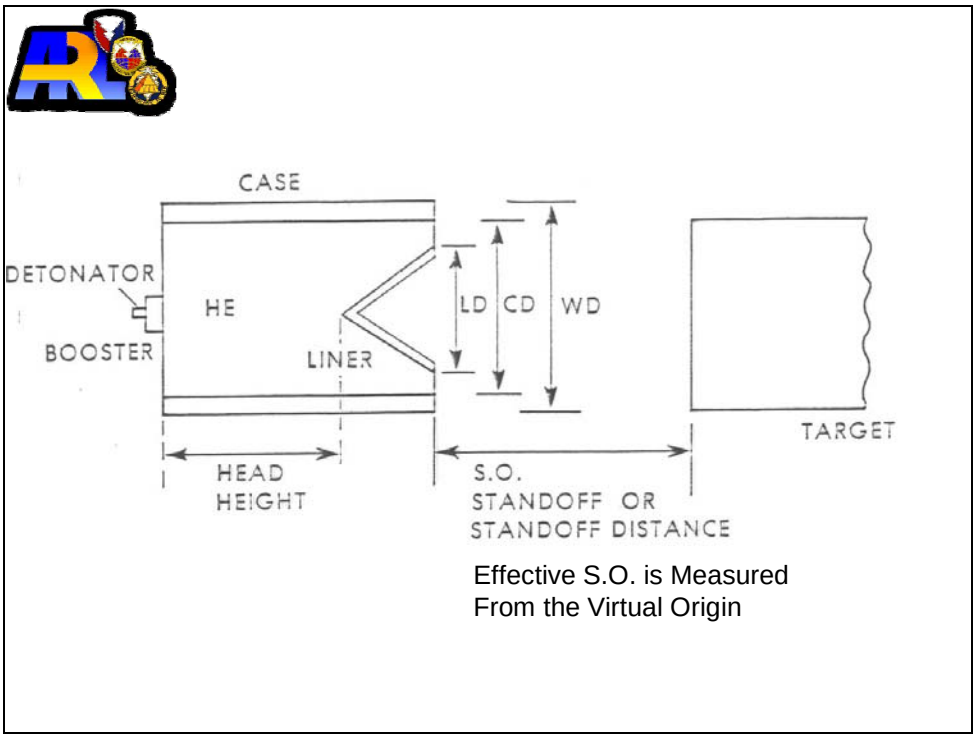

Figure 7. The nomenclature for a shaped-charge configuration.

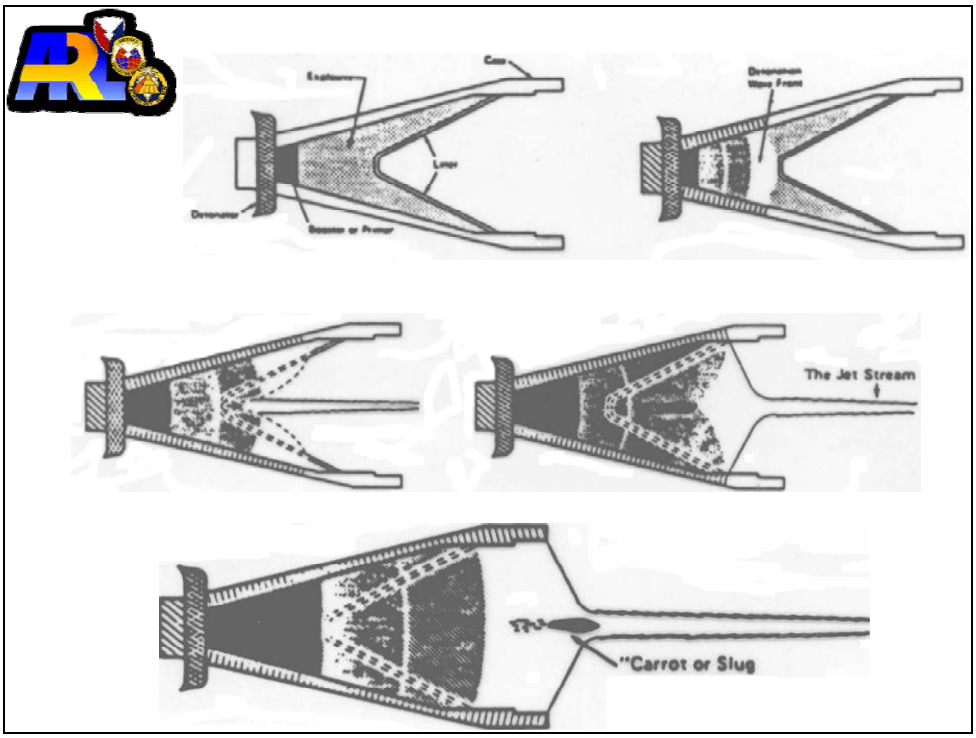

Figure 8. Detonation stages of a typical shaped charge.

Tip Velocity: 10 km/s

Maximum Strains > 10

Pressure: 200 GPa decaying to 20 GPa

Strain Rate: $10^{4-}10^{7}$/s

Jet Temperature: 400-500C

Figure 9. Liner collapse and jet formation.

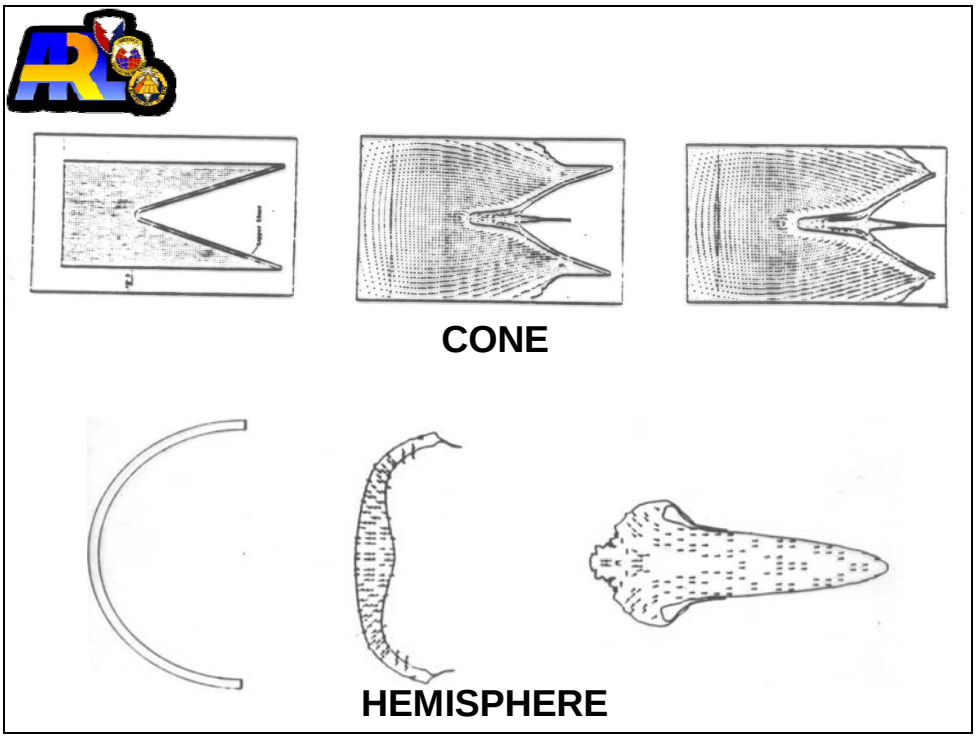

Figure 10. Liner collapse.

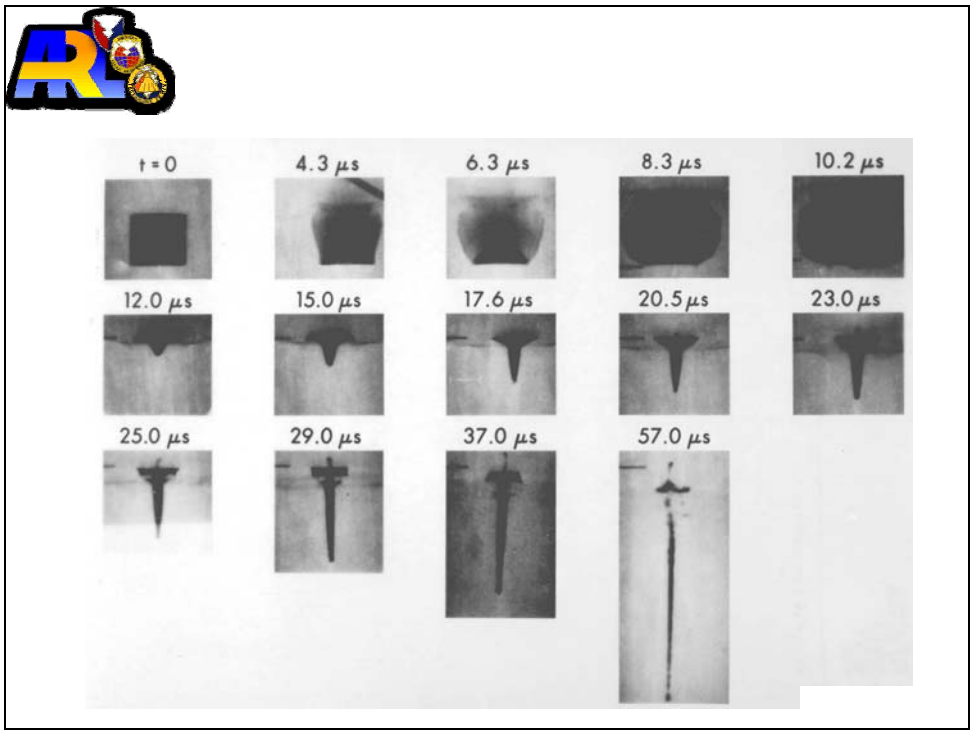

Figure 11. Collapse of a shaped charge with a hemispherical liner.

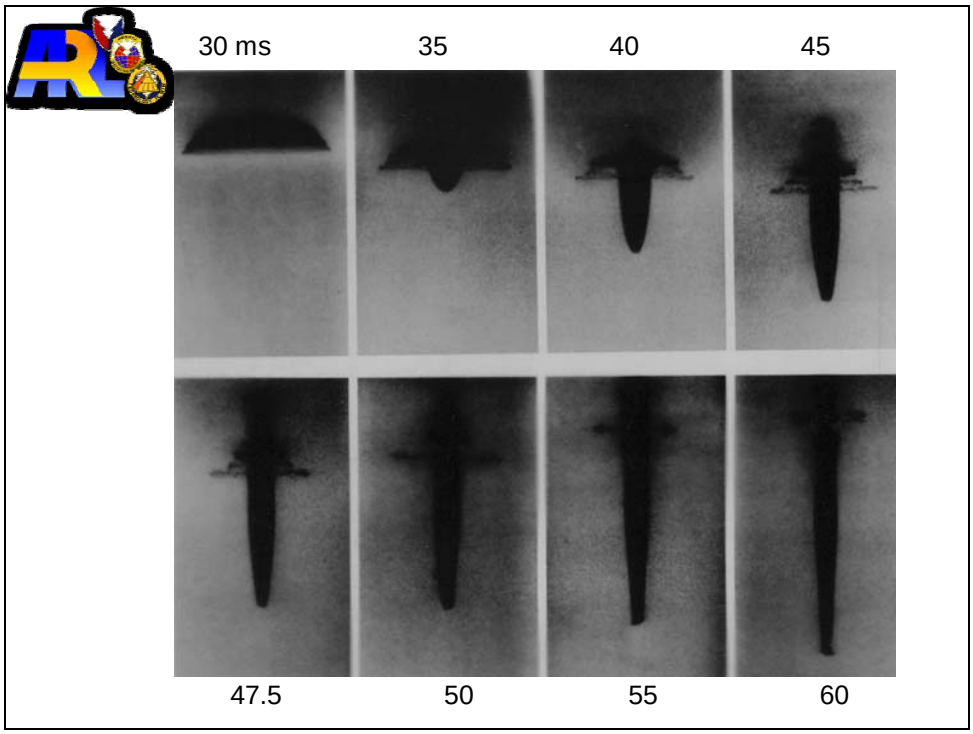

Figure 12. Collapse of a shaped charge with a hemispherical liner (continued).

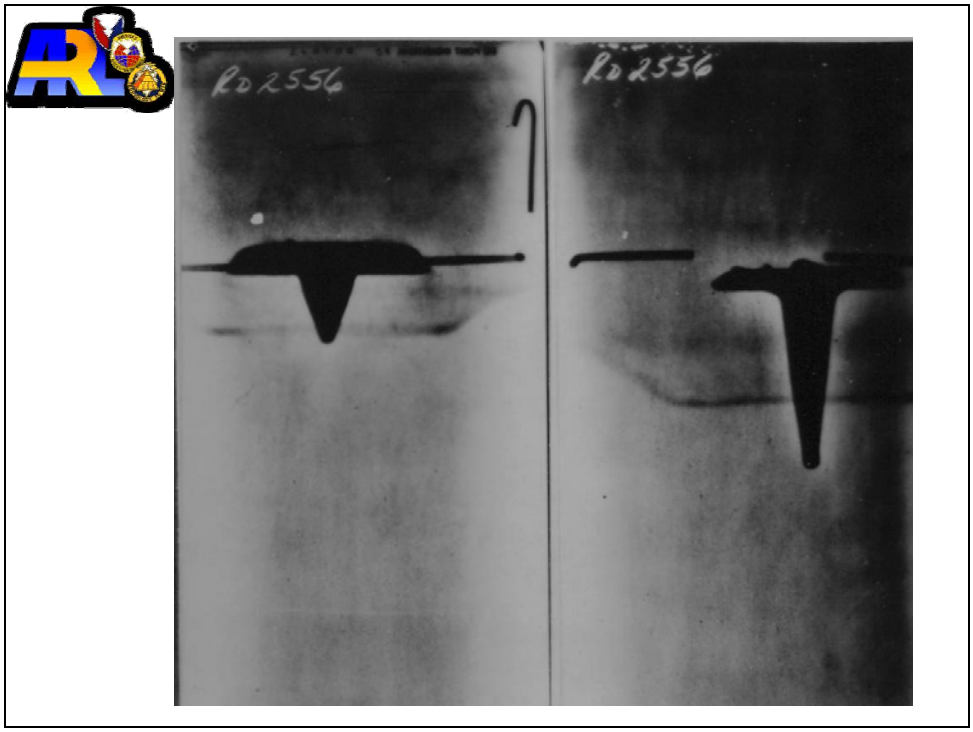

Figure 13. Collapse of a shaped charge with a hemispherical liner (continued).

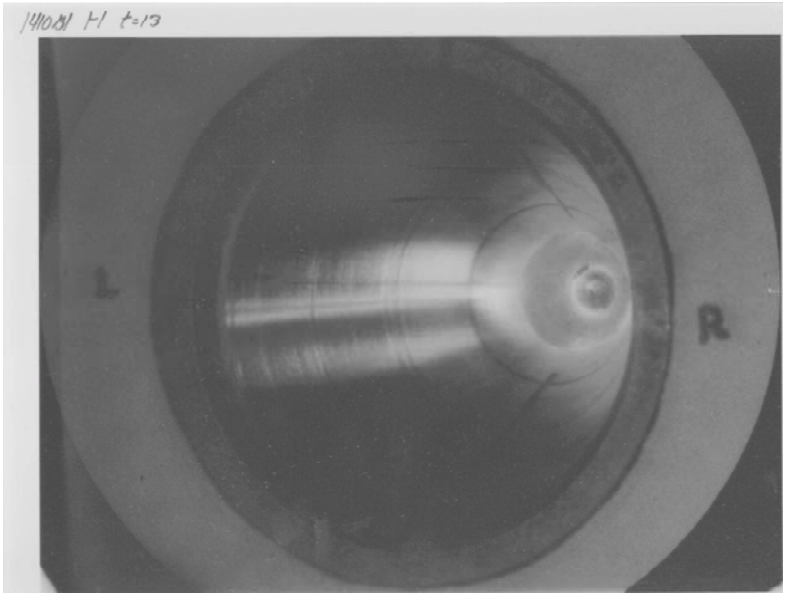

Figure 14. High-speed camera viewing the collapse of a shaped charge with a conical liner.

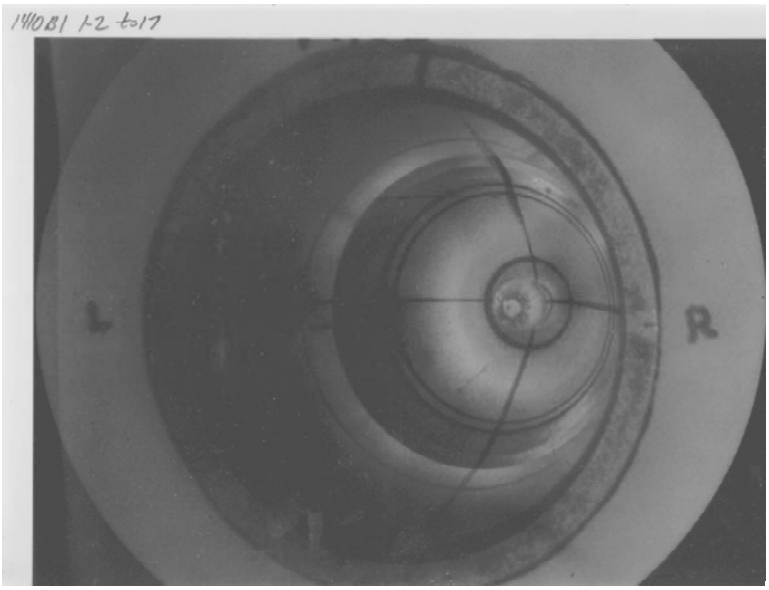

Figure 15. High-speed camera viewing the collapse of a shaped charge with a conical liner (continued).

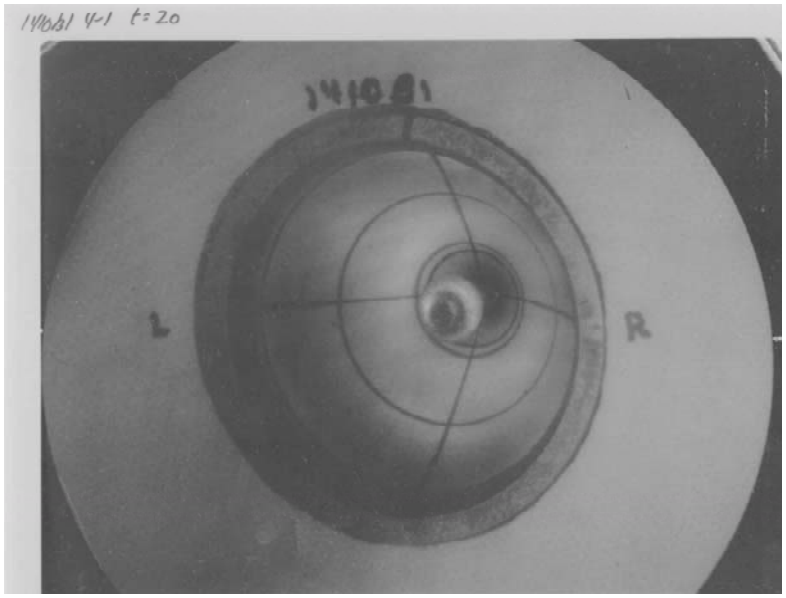

Figure 16. High-speed camera viewing the collapse of a shaped charge with a conical liner (continued).

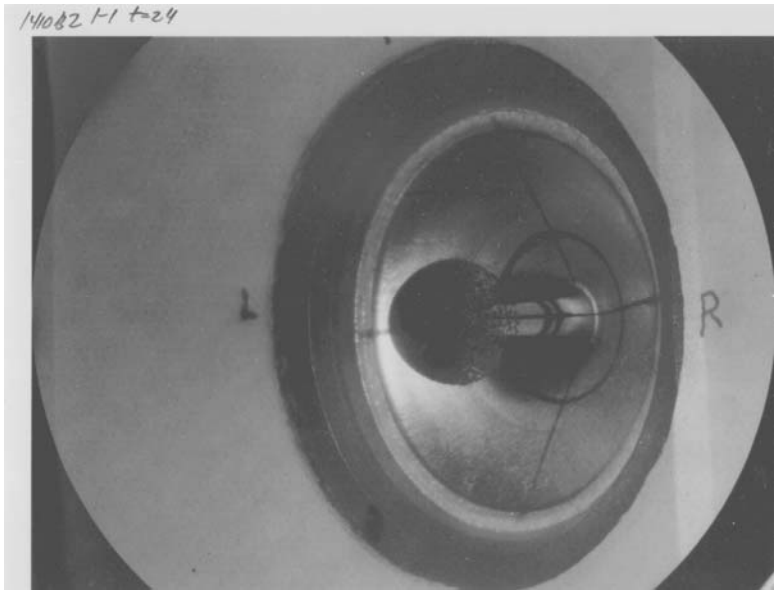

Figure 17. High-speed camera viewing the collapse of a shaped charge with a conical liner (continued).

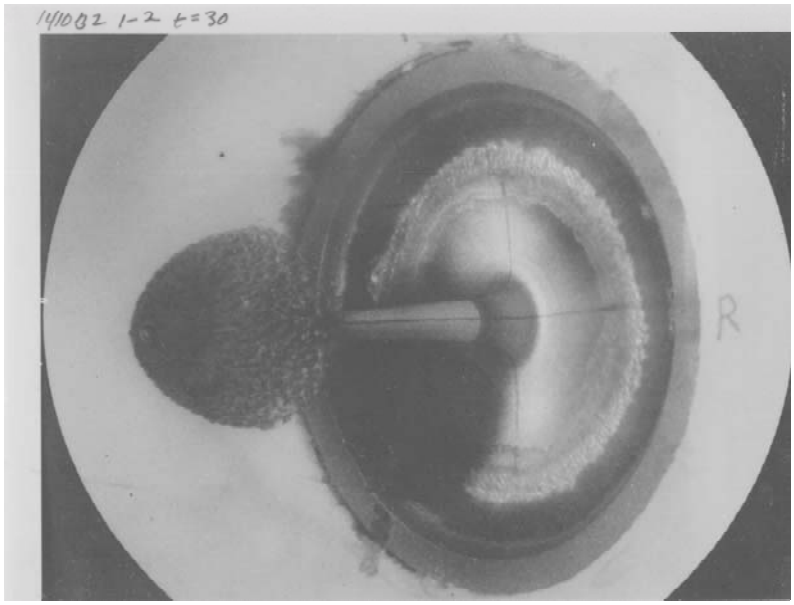

Figure 18. High-speed camera viewing the collapse of a shaped charge with a conical liner (continued).

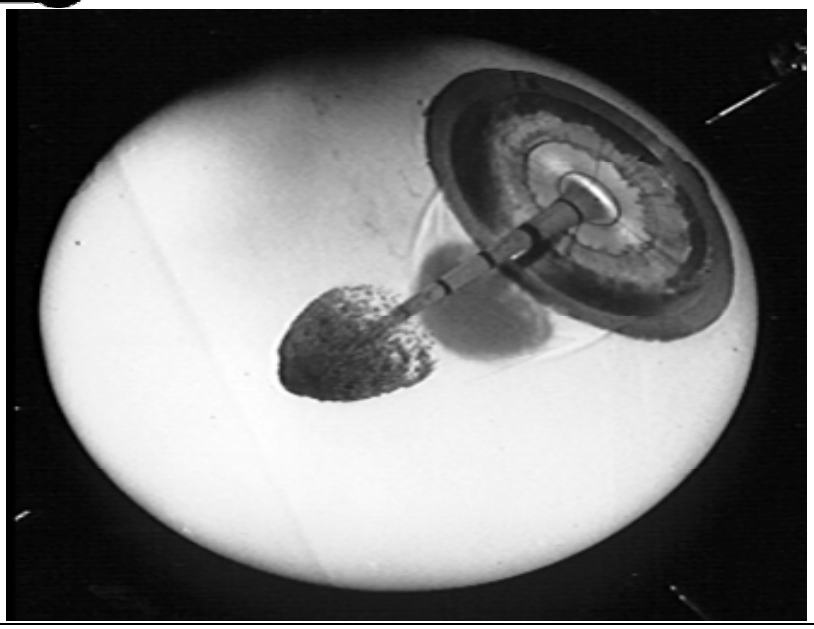

Figure 19. High-speed camera viewing the collapse of a shaped charge with a conical liner (continued).

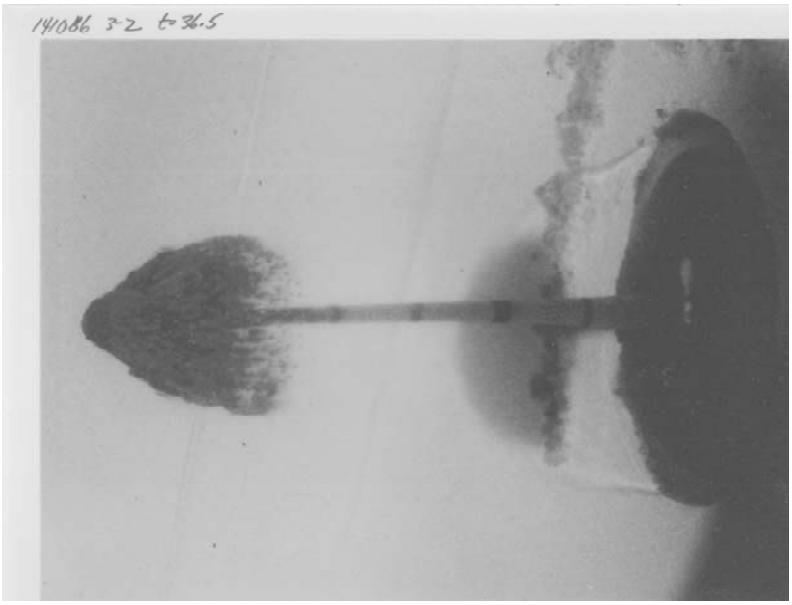

Figure 20. High-speed camera viewing the collapse of a shaped charge with a conical liner (continued).

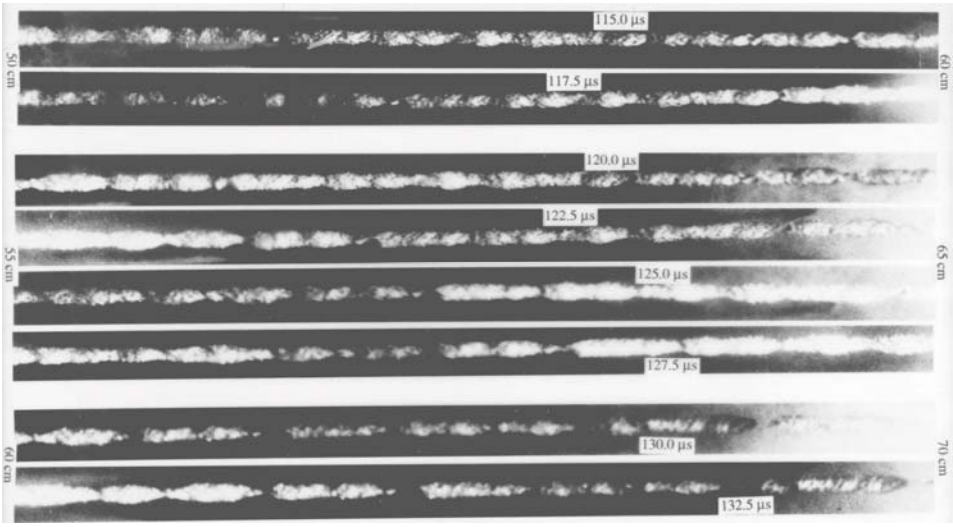

Figure 21. Collapse of a shaped charge with a conical liner after particulation.

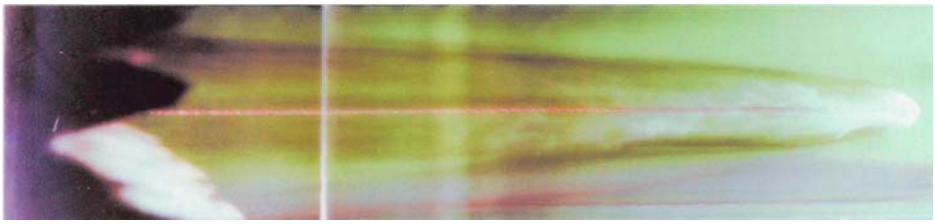

Figure 22. Collapse of a shaped charge with a conical liner prior to particulation.

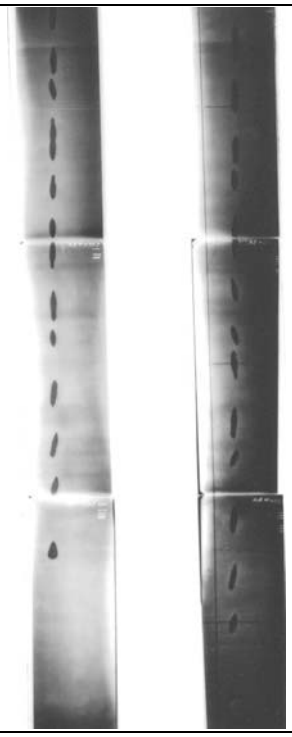

Figure 23. The jet from a shaped charge with a hemispherical liner at late times.

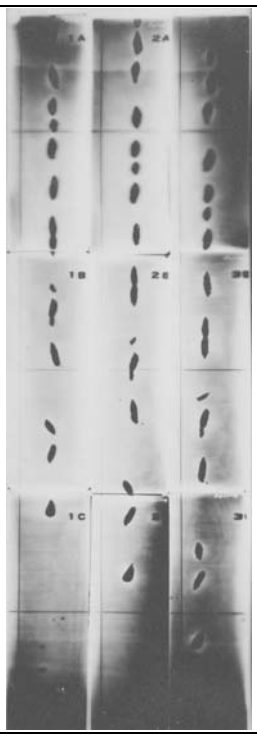

Figure 24. The jet from a shaped charge with a hemispherical liner at very late times.

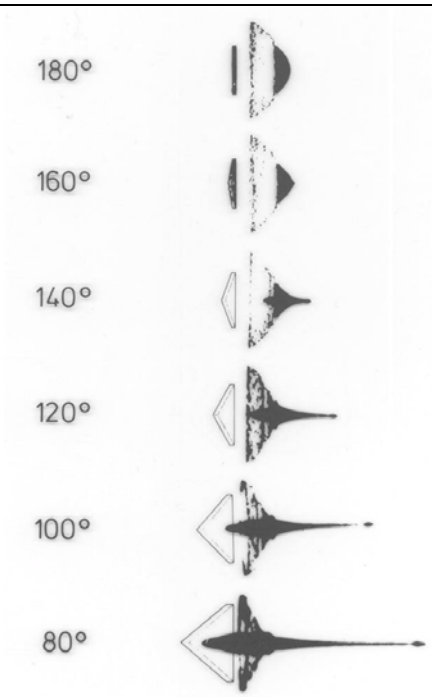

Figure 25. The effect of apex angle on the jet formation.

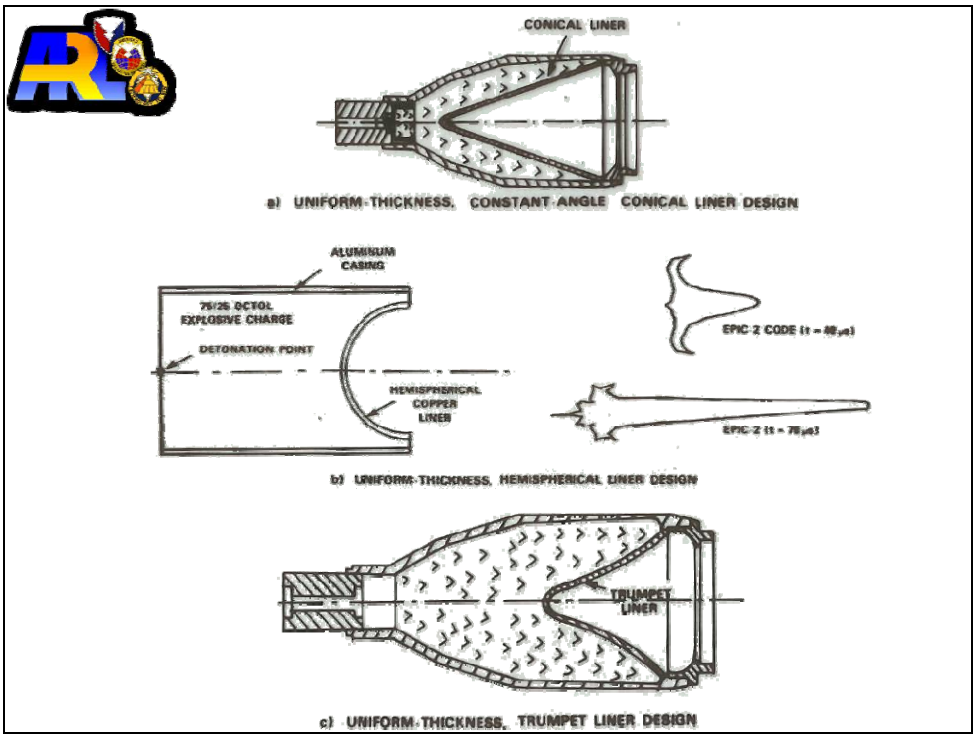

Figure 26. Shaped-charge liner designs.

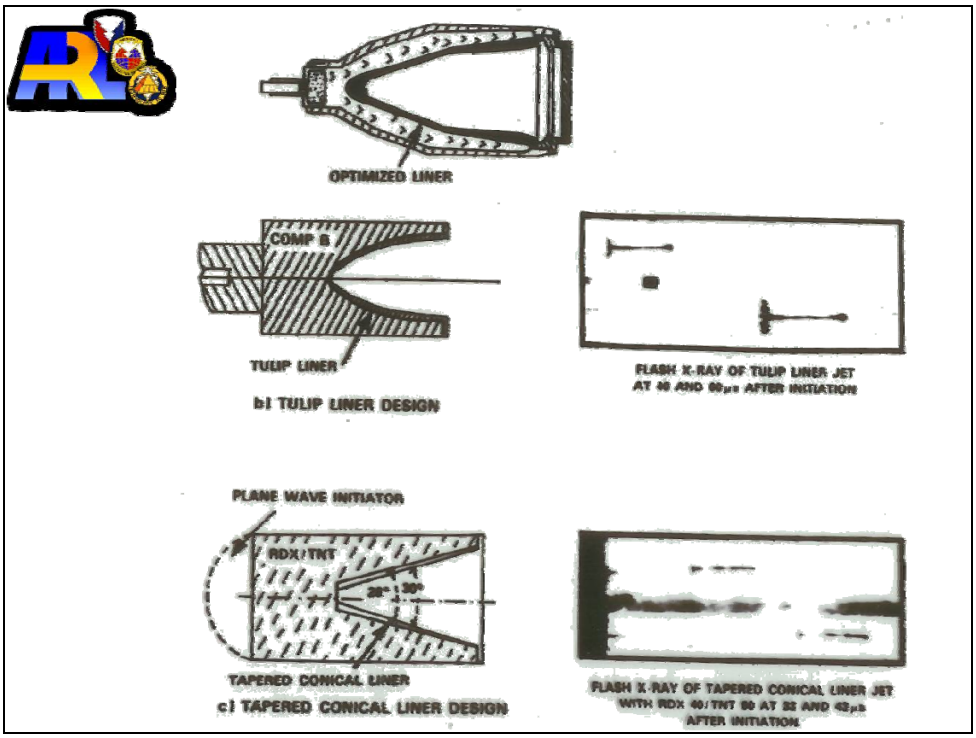

Figure 27. Shaped-charge liner designs (continued).

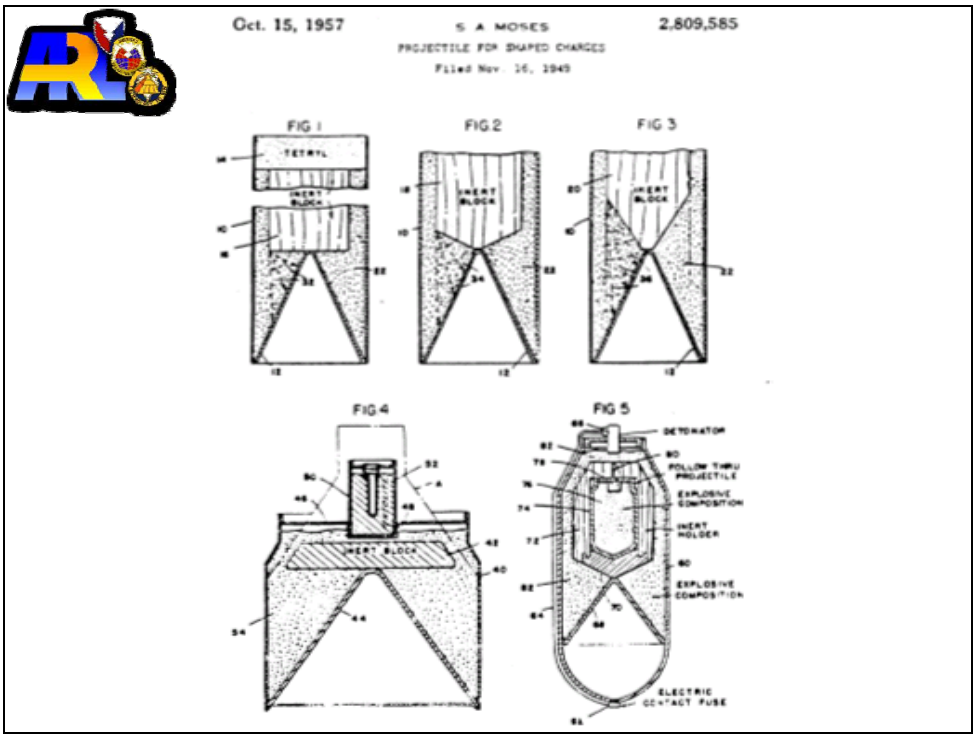

Figure 28. Waveshaping concepts.

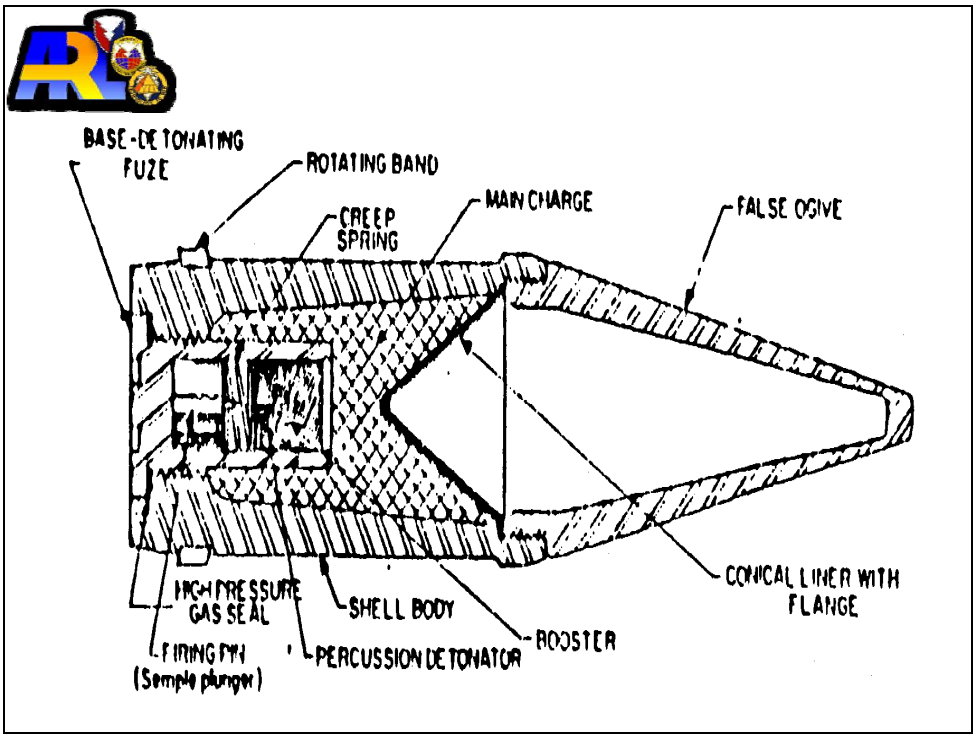

Figure 29. Warhead with ogive.

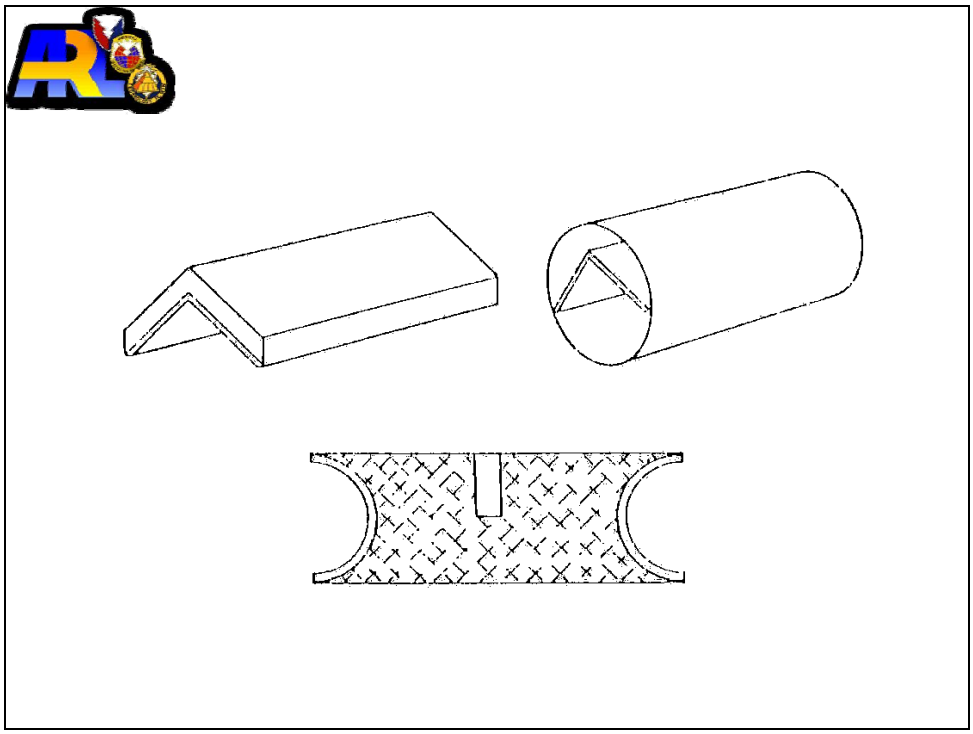

Figure 30. Linear and circular lined shaped-charge configurations.

- **On impact, the shaped charge within the round ignites and begins to play a steam of plasma on the target. Each shaped charge configuration has an optimum distance from the target where the cutting power of the plasma cone is greatest. This detonation distance is established by the length of the warhead tip. The plasma cone burns through the armor and sprays molten particles into the tank at speeds of 30,000 fps.**

Figure 31. Misnomers.

- **A shaped charge detonates on impact, liquefying metal, which melts the tanks armor.**
- **The jet is a high temperature plasma (about 20,000 °C).**
- **The jet reaches a density several times that of steel, and the armor becomes plastic and yields whilst the jet torch assists by melting and burning the armor metal.**

Figure 32. Misnomers (continued).

JET TEMPERATURE

W. G. VON HOLLE AND J. J. TRIMBLE, "TEMPERATURE MEASUREMENTS OF SHOCKED COPPER PLATES AND SHAPED CHARGE JETS BY TWO-COLOR IR RADIOMETRY", JOURNAL OF APPLIED PHYSICS, VOL. 47, NO. 6, PP. 2391-2394, JUNE 1976.

W. G. VON HOLLE AND J. J. TRIMBLE, "SHAPED-CHARGE TEMPERATURE MEASUREMENTS", THE SIXTH SYMPOSIUM ON DETONATION, SAN DIEGO, CALIFORNIA, AUGUST 24-27, 1976.

W. G. VON HOLLE AND J. J. TRIMBLE, "TEMPERATURE MEASUREMENT OF COPPER AND EUTECTIC METAL SHAPED-CHARGE JETS", BALLISTIC RESEARCH LABORATORY REPORT, BRL-R-2004, AUGUST, 1977.

W. P. WALTERS, G. H. JONAS AND J. A. ZUKAS, "EXPLOSIVE LOADING OF LEAD HEMISPHERICAL LINERS", COMPUTERS AND STRUCTURES, VOL. 20, NO. 1-3, PP. 615-621, 1985.

Figure 33. Jet temperature references.

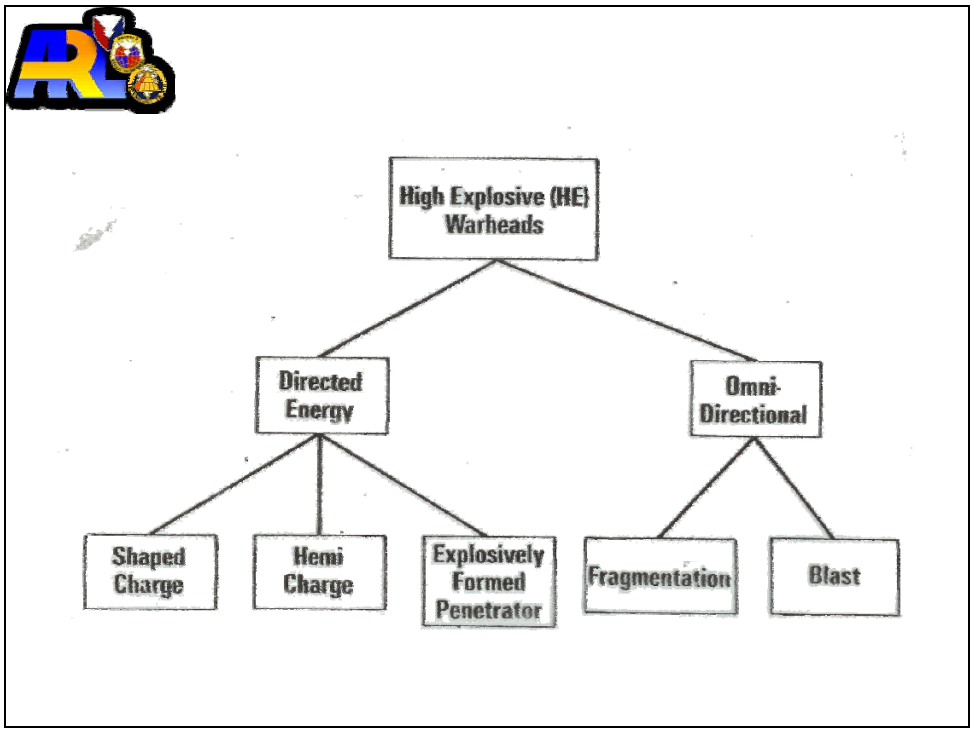

Figure 34. The family of high-explosive warheads.

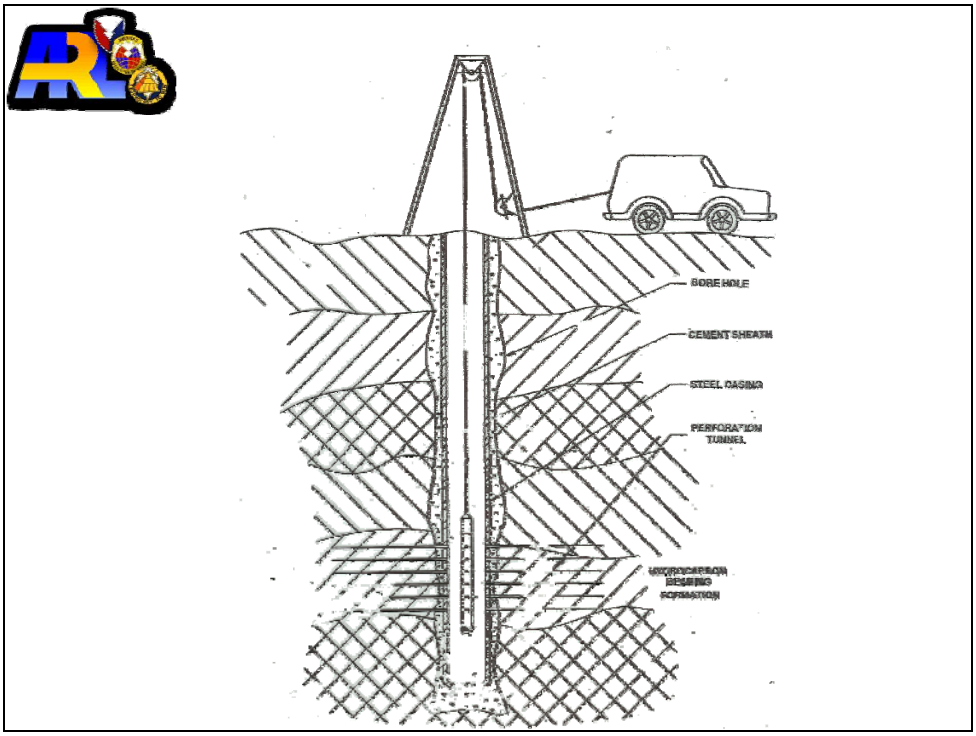

Figure 35. Wireline perforating-wellbore schematic.

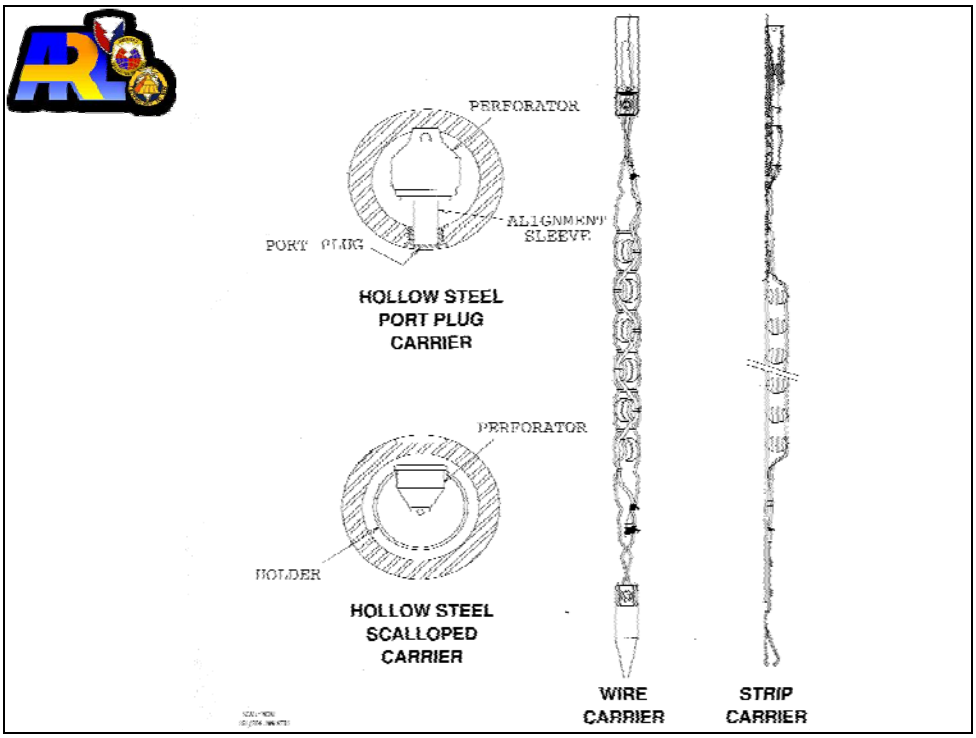

Figure 36. Perforator hardware.

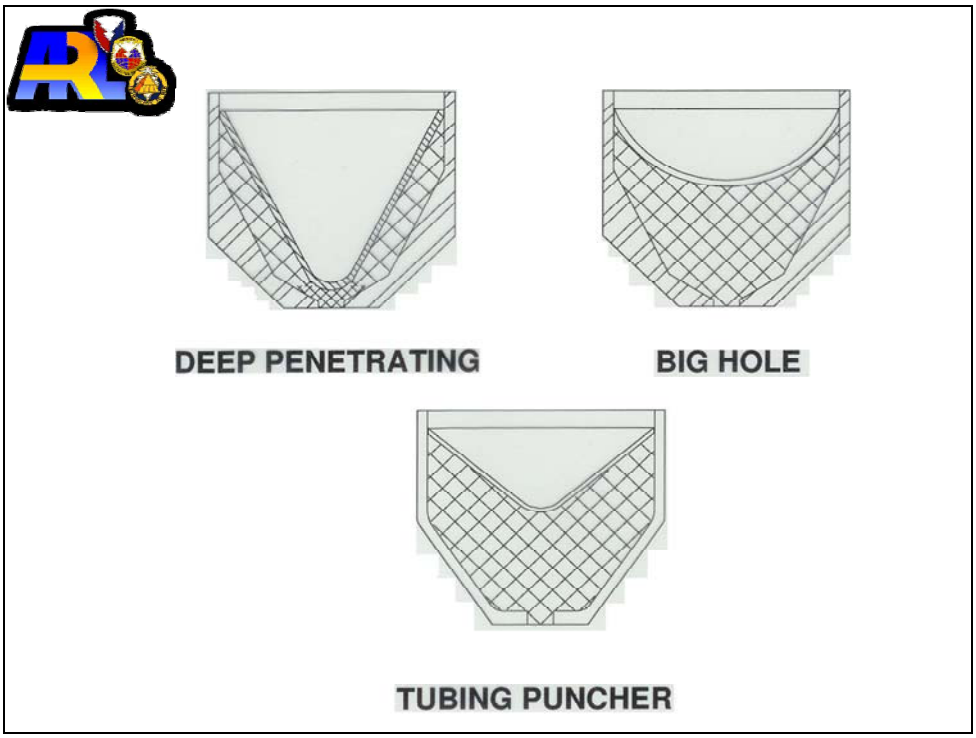

Figure 37. Perforator types.

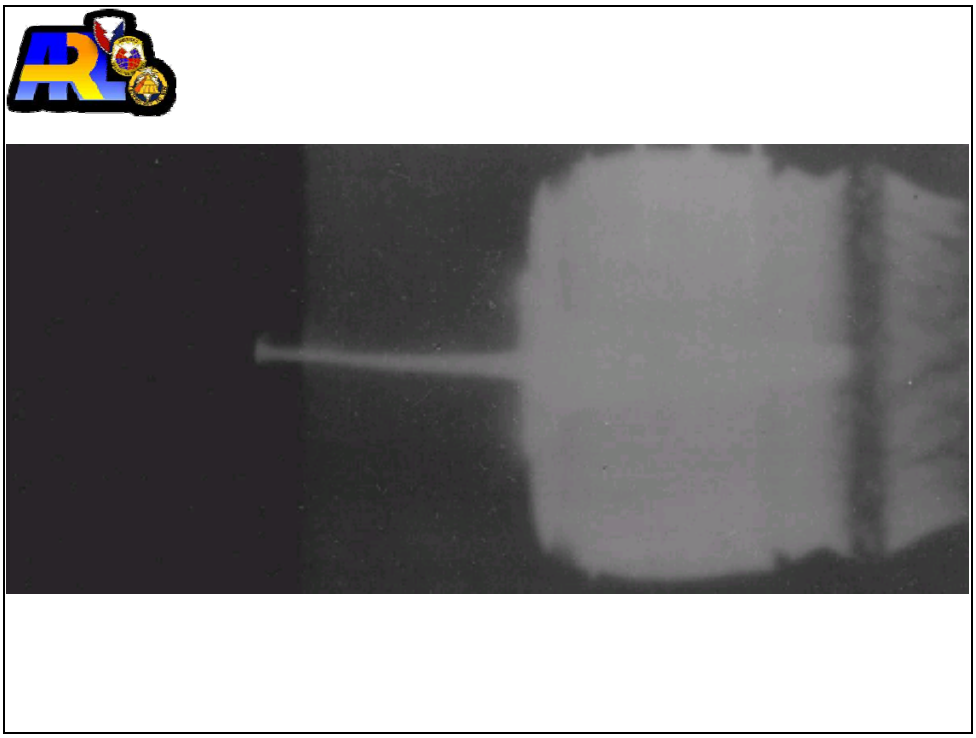

Figure 38. Jet from a powder liner.

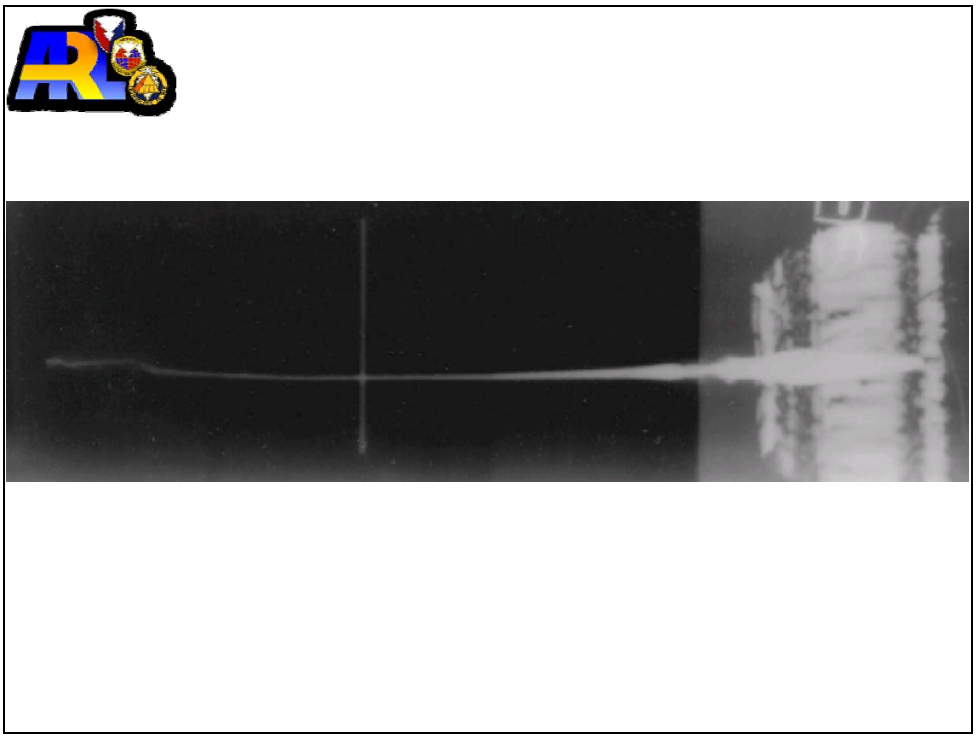

Figure 39. Jet from a powder liner (continued).

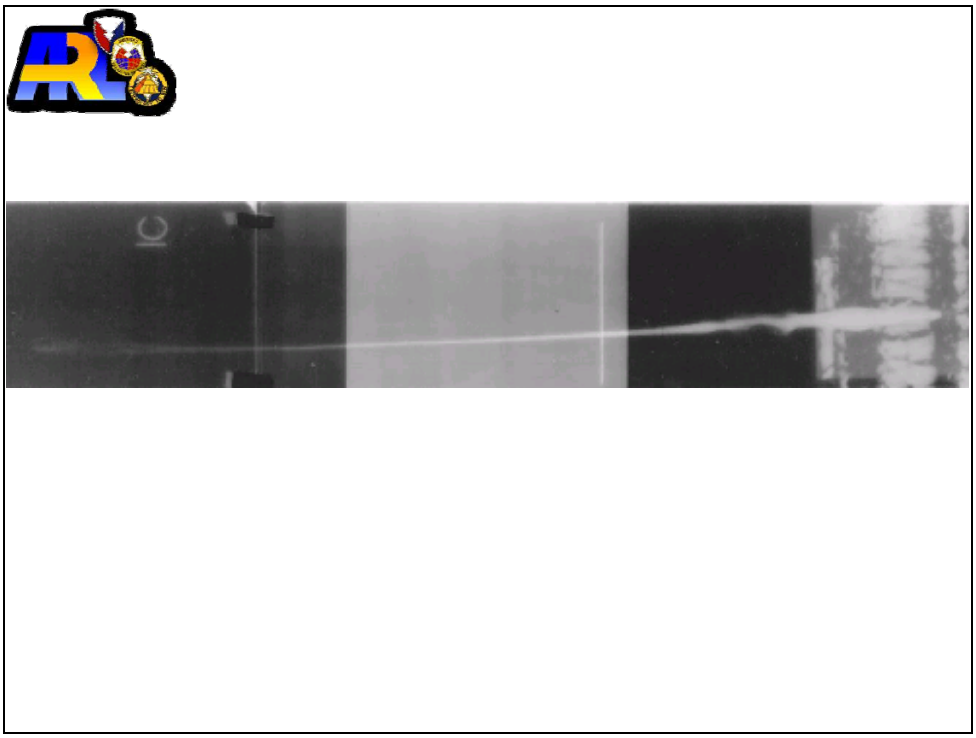

Figure 40. Jet from a powder liner (continued).

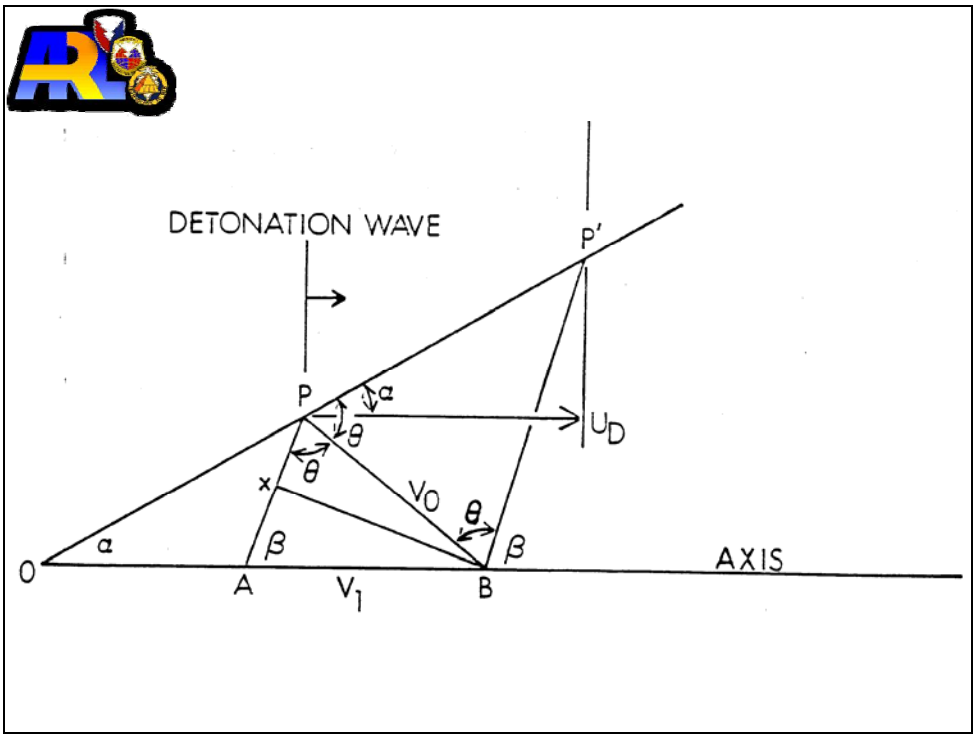

Figure 41. Geometry of the collapse process.

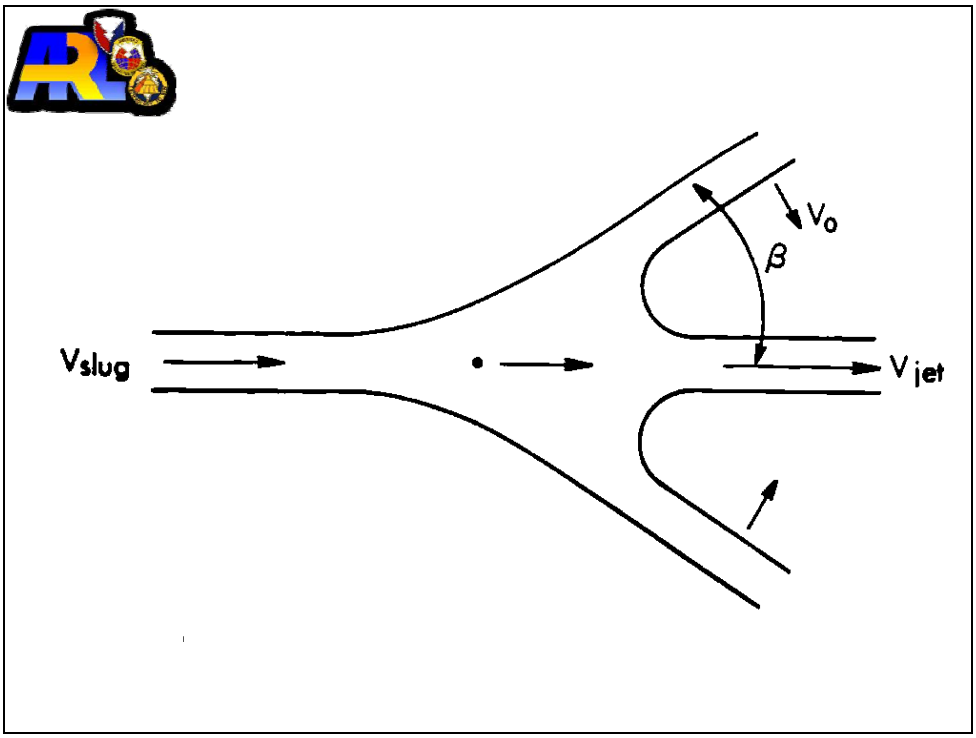

Figure 42. Velocities with respect to a fixed coordinate system.

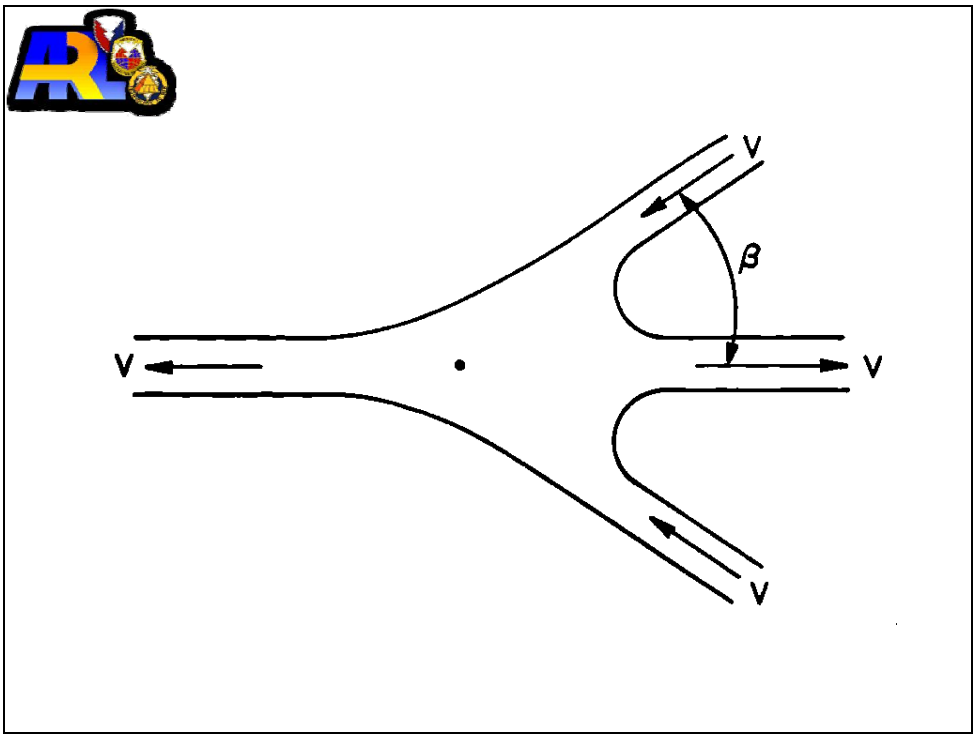

Figure 43. Velocities referred to a coordinate moving with velocity V_1.

STEADY STATE MODEL OVERPREDICTS V.

JET L = SLANT HEIGHT OF CONE.

NONE-STEADY (PER) THEORY DEVELOPED.

COLLAPSE VELOCITIES OF VARIOUS LINER ELEMENTS ARE NOT THE SAME BUT DEPEND ON THEIR ORIGINAL POSITION ON THE LINER.

Figure 44. The Birkhoff theory.

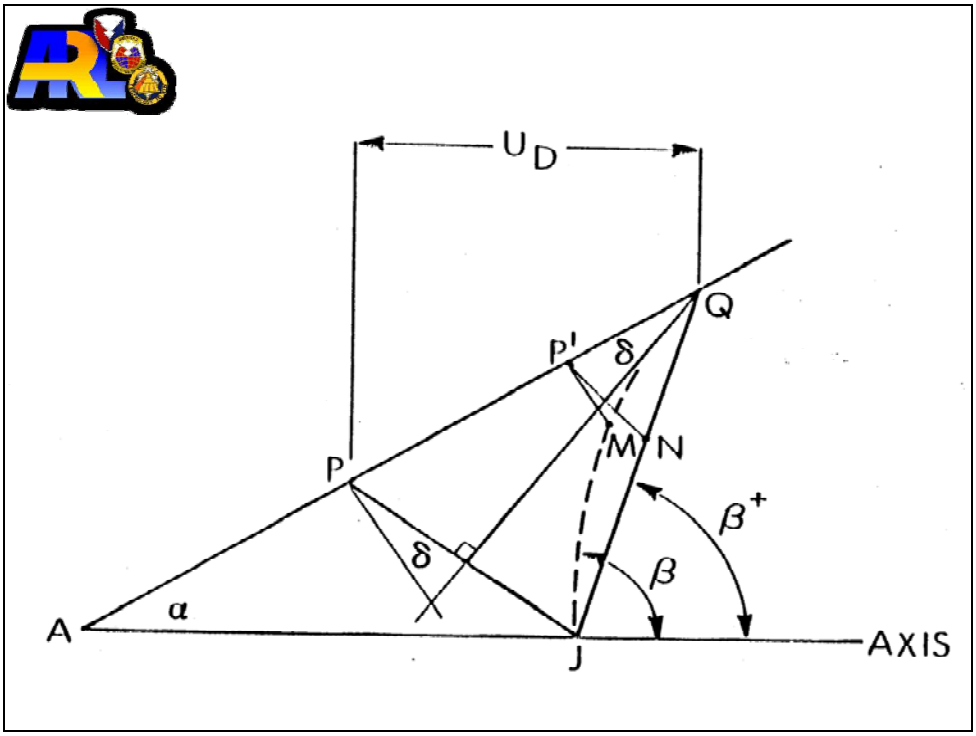

Figure 45. Birkhoff's geometry.

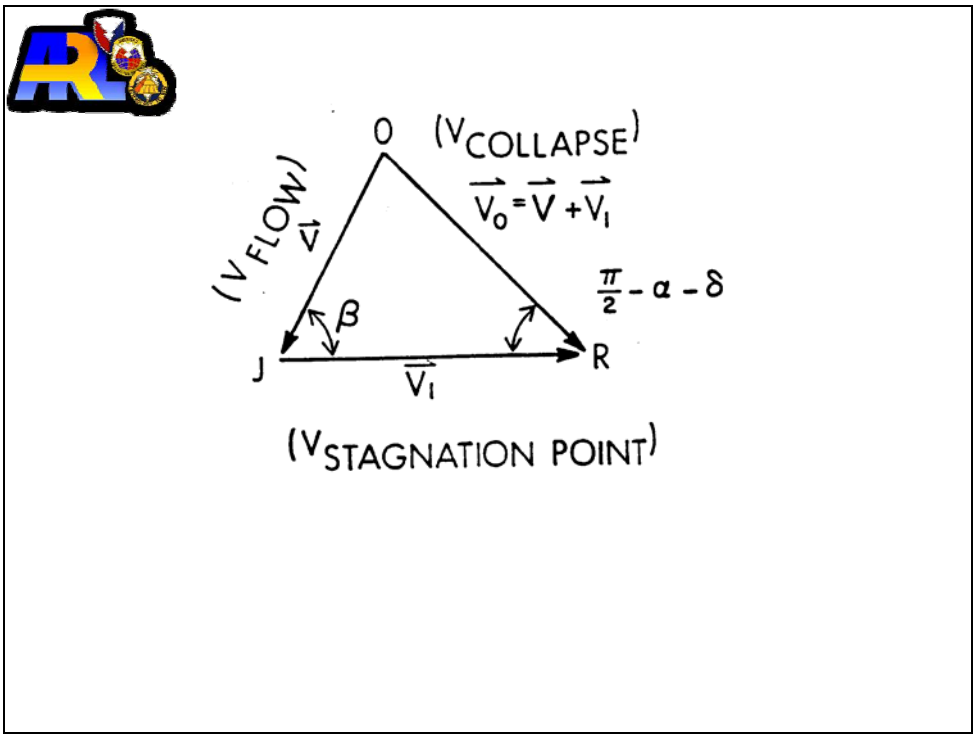

Figure 46. Relationship between $\vec{V}_0$, the liner collapse velocity, $\vec{V}$ the collapse velocity relative to the collision point, and $\vec{V}_1$ the collision point velocity.

$$V = V_0 \frac{\cos(\alpha + \delta)}{\sin \beta}$$

$$V_1 = V_0 \frac{\cos(\beta - \alpha - \delta)}{\sin \beta}$$

$$\vec{V} = V_{FLOW}$$

$$\vec{V}_1 = V_{\text{stagnation point}}$$

$$V_0 = V_{\text{collapse}} = \vec{V} + \vec{V}_1$$

Figure 47. The velocities.

IN FIXED COORDINATES

$$V_j = V_1 + V$$

$$V_s = V_1 - V$$

or

$$V_j = V_0 \csc\frac{\beta}{2}\cos\left(\alpha + \delta - \frac{\beta}{2}\right)$$

$$V_s = V_0 \sec\frac{\beta}{2}\sin\left(\alpha + \delta - \frac{\beta}{2}\right)$$

If $\beta = \beta^{+} = \alpha + 2\delta$

V_j, V_s reduce to Birkhoff, et al. (Using trigonometric trickery)

Eliminating δ yields

$$V_j = V_0\left(\csc\frac{\beta}{2}\right)\cos\left(\alpha - \frac{\beta}{2} + \sin^{-1}\frac{V_0}{2u}\right)$$

$$V_s = V_0\left(\sec\frac{\beta}{2}\right)\sin\left(\alpha - \frac{\beta}{2} + \sin^{-1}\frac{V_0}{2u}\right)$$

Figure 48. The jet and slug velocities.

$$dm = dm_j + dm_s$$

$$\frac{dm_j}{dm} = \sin^2\left(\frac{\beta}{2}\right)$$

$$\frac{dm_s}{dm} = \cos^2\left(\frac{\beta}{2}\right)$$

Figure 49. Conservation of mass yields as in the steady state theory.

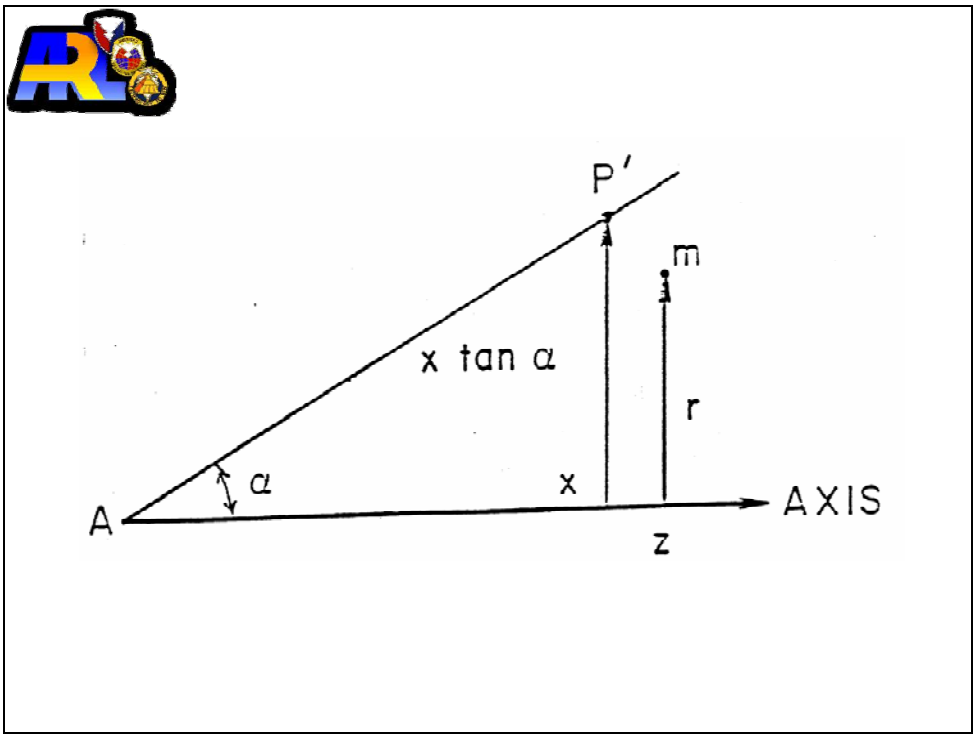

Figure 50. Calculation of the collapse angle.

Calculate β

Cylindrical coordinates of M are (r, z) of P' are (X $\tan\alpha$, X)

$$Z = X + V_0(t - T)\sin A$$

$$r = X\tan\alpha - V_0(t - T)\cos A$$

$t =$ elapsed time since detonation wave passed the apex of the cone.

$$T = \frac{X}{U_D} = \frac{X}{U\cos\alpha}$$

$$A = \alpha + \delta$$

The slope of the contour of the collapsing liner at any t can be

obtained from the $\frac{\partial r}{\partial z}$ using the above equations and some calculus.

Figure 51. Calculation of the collapse angle (continued).

The time when a given element reaches the axis is given by

$$r = X\tan\alpha - V_0(t-T)\cos A$$

for $r = 0$ or

$$t - T = \frac{X\tan\alpha}{V_0\cos A}$$

Also, $\tan\beta = \dfrac{\partial r}{\partial z}$ evaluated at $r = 0$ or

$$\tan\beta = \frac{\sin\alpha + 2\sin\delta\cos A - X\sin\alpha(1-\tan A\tan\delta)\,{V_0'}/{V_0}}{\cos\alpha - 2\sin\delta\sin A + X\sin\alpha(\tan A + \tan\delta)\,{V_0'}/{V_0}}$$

Figure 52. Calculation of the collapse angle (continued).

and since $2\delta = \beta^+ - \alpha$ and $2A = \beta^+ + \alpha$

$$\tan\beta = \frac{\sin\beta^+ - X\sin\alpha(1-\tan A\tan\delta)\,{V_0'}/{V_0}}{\cos\beta^+ + X\sin\alpha(\tan A + \tan\delta)\,{V_0'}/{V_0}}$$

$\beta \rangle \beta^+$ since $V_0' \langle 0$ or the collapse velocity decreases from apex

to base for cone angles (2α) which are not extremely large.

Watch the trigonometric quadrant for each angle!

Figure 53. Calculation of the collapse angle (continued).

TAYLOR ANGLE APPROXIMATION

For Grazing Incidence

Acceleration to final velocity is instantaneous.

Metal plate undergoes pure rotation, i.e., no net shear flow or change in length or thickness (behaves like a hinge).

Figure 54. The Taylor angle concept.

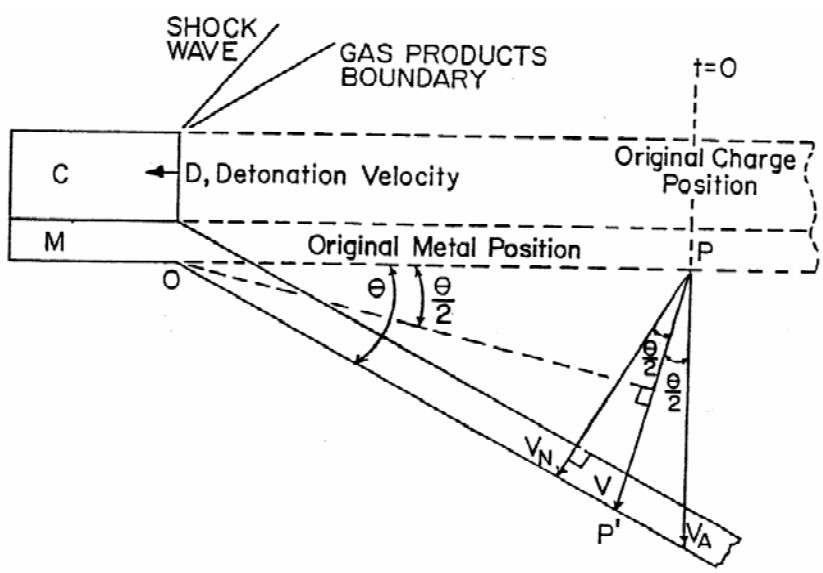

Figure 55. Taylor's geometry.

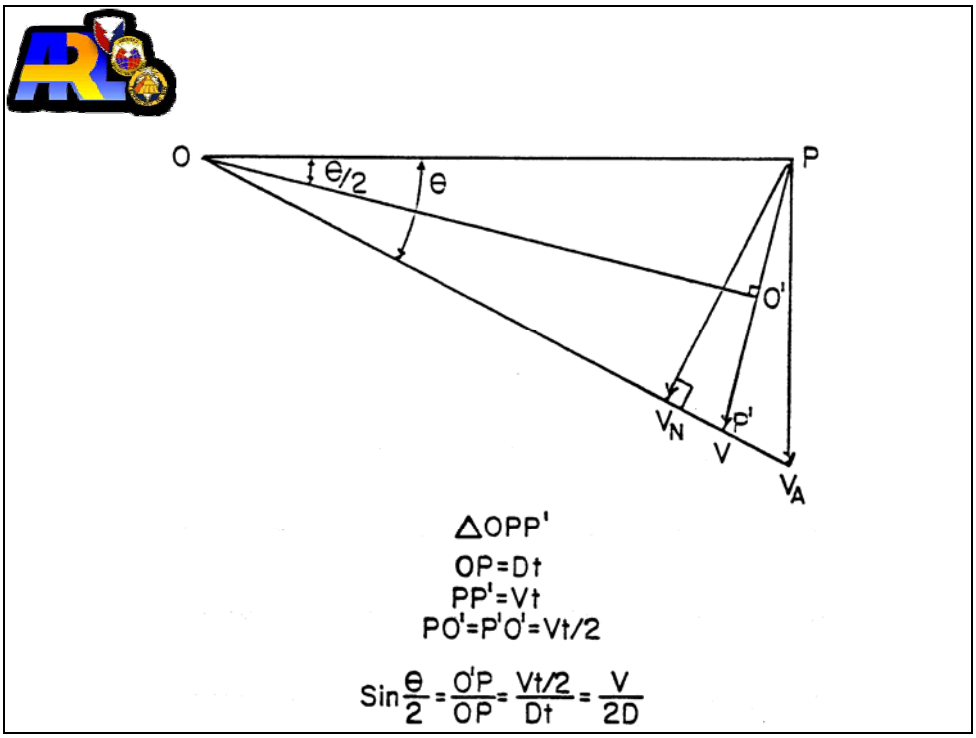

Figure 56. The Taylor angle.

- TAYLOR RELATION - AN EQUATION RELATING V_0 TO δ

$$\sin\delta = V_0/2U$$

- TWO APPROACHES

  I. FORMULA FOR V_0 - e.g., GURNEY

  II. FORMULA FOR δ - e.g., DEFOURNEAUX

- UNSTEADY THEORY

  - MODIFIED TAYLOR RELATION

  - LINER ACCELERATION -- V = f(time)

Figure 57. Liner collapse.

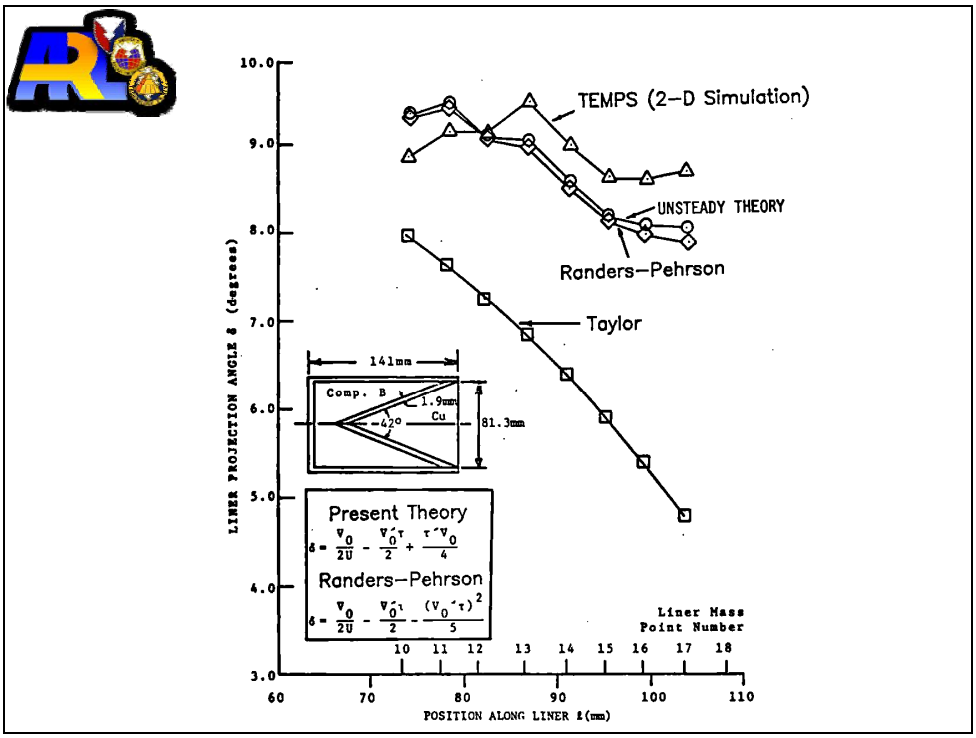

Figure 58. Liner projection angle by the simple Taylor relation (steady) and the unsteady theory.

I. VELOCITY FORMULAS

- GURNEY (1943)

$$V_0 = \sqrt{2E}\ f(\mu)$$

E = GURNEY ENERGY

μ = M/C = METAL-TO-EXPLOSIVE MASS RATIO

ASSUMPTIONS:

- LINEAR VELOCITY DISTRIBUTION IN GAS
- GLOBAL BALANCE OF MOMENTUM AND ENERGY

APPLICABLE GEOMETRIES:

- SANDWICHES, CYLINDRICAL, OR SPHERICAL EXPLOSION

GEOMETRY NOT APPLICABLE -- IMPLOSION

Figure 59. Liner collapse, velocity formulas.

KLEINHANSS (1971) -- FOR IMPLODING CYLINDER, EMPIRICAL

$$V_0 = U\, f(R_0, R_1, E)$$

DUVALL ET AL. (1958) -- HYDRODYNAMIC THEORY

$$V_0 = Uf(\mu)$$

TRINKS -- EMPIRICAL

$$V_0 = Uf(\mu)$$

Figure 60. Liner collapse, velocity formulas (continued).

DEFOURNEAUX: (1970) (ADAPTED FROM RICHTER)

$$\frac{1}{2\delta} = \frac{1}{\phi_0} + K\,\rho_E\,\mu$$

ϕ_0, K = EMPIRICAL CONSTANTS

MODIFIED DEFOURNEAUX: DYNA EAST (1975) (USED IN DESC, BASC)

$$\frac{1}{2\delta} = \frac{1}{\phi_0(\gamma)} + K(\gamma)\,\rho_E\,\frac{A_L}{A_E}$$

A_L, A_E = CROSS-SECTIONAL AREAS OF LINER, EXPLOSIVE

KERDRAON: (1975)

$$\phi = \frac{1}{C_1 + C_2\mu}\exp\left[-C_3\frac{\mu}{R_1^2}\right]$$

C_1, C_2, C_3 = EMPIRICAL CONSTANTS

Figure 61. Turning-angle formulas.

LINER ACCELERATION TO THE AXIS IS NOT INSTANTANEOUS,

AS ASSUMED BY THE PER THEORY!

Figure 62. Liner acceleration.

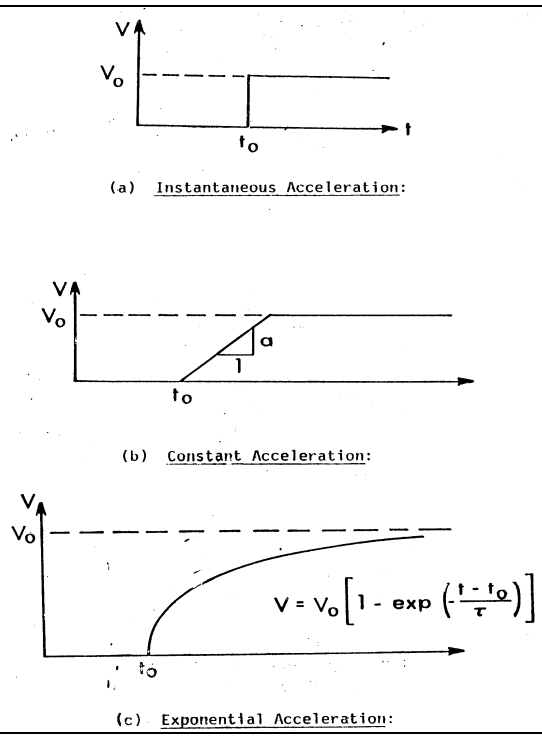

Figure 63. Liner acceleration (continued).

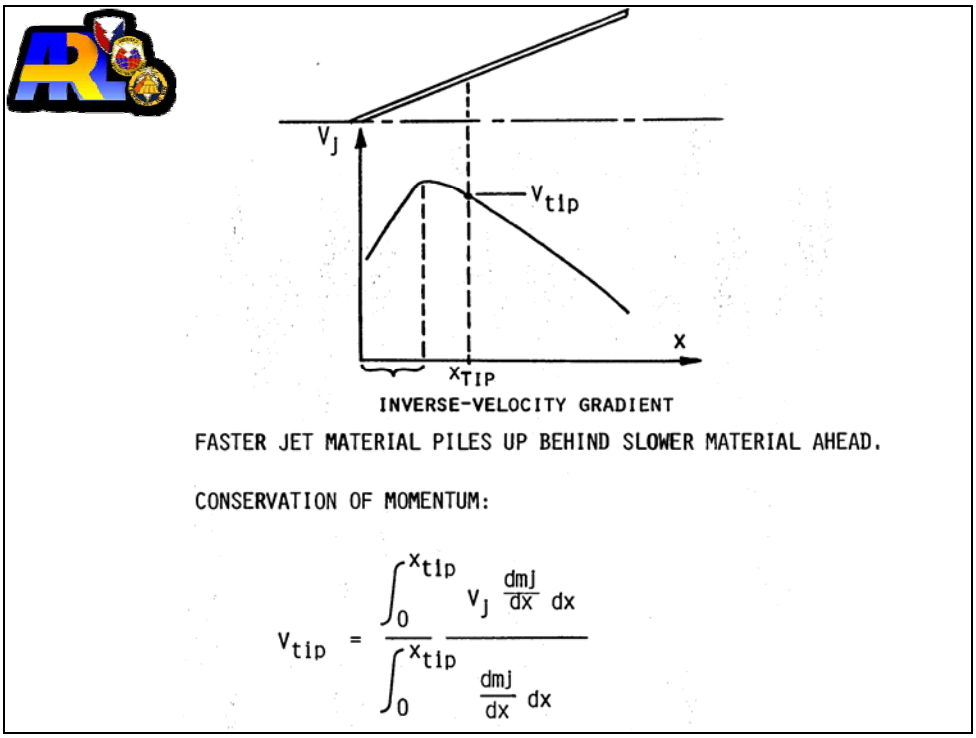

Figure 64. The jet-tip velocity.

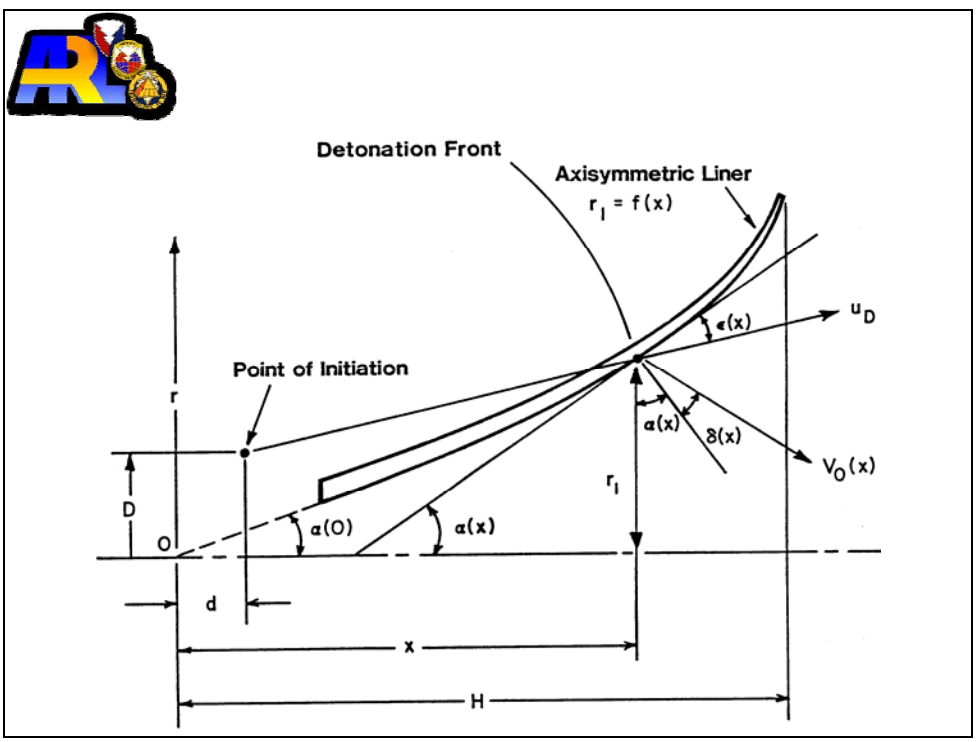

Figure 65. Extensions of the theory.

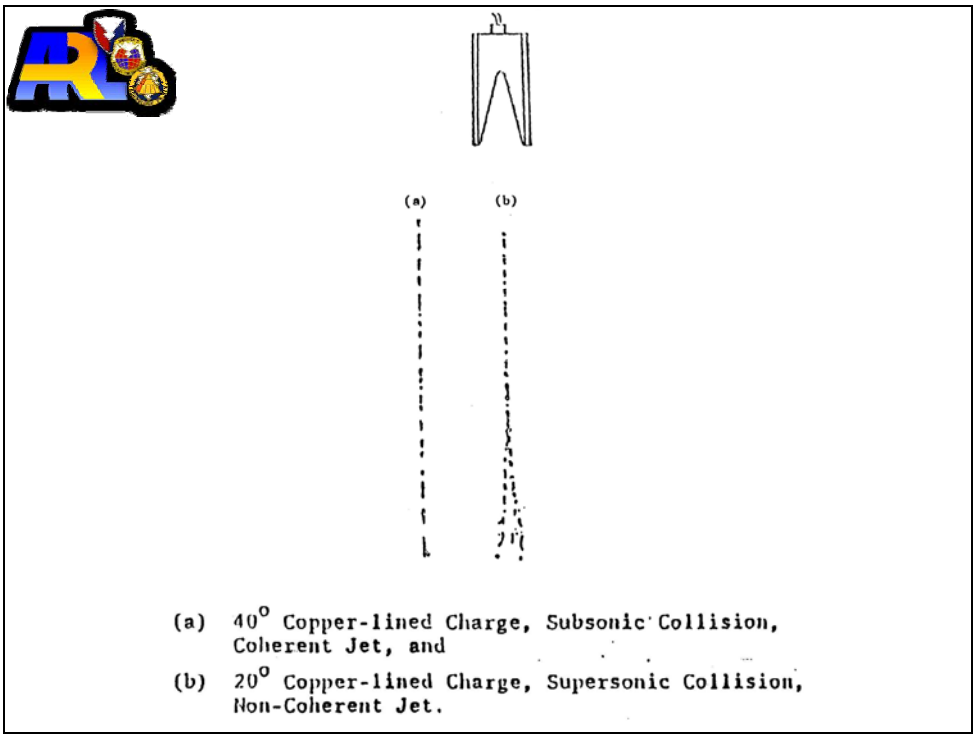

Figure 66. Radiographs of jets from two typical conical charges.

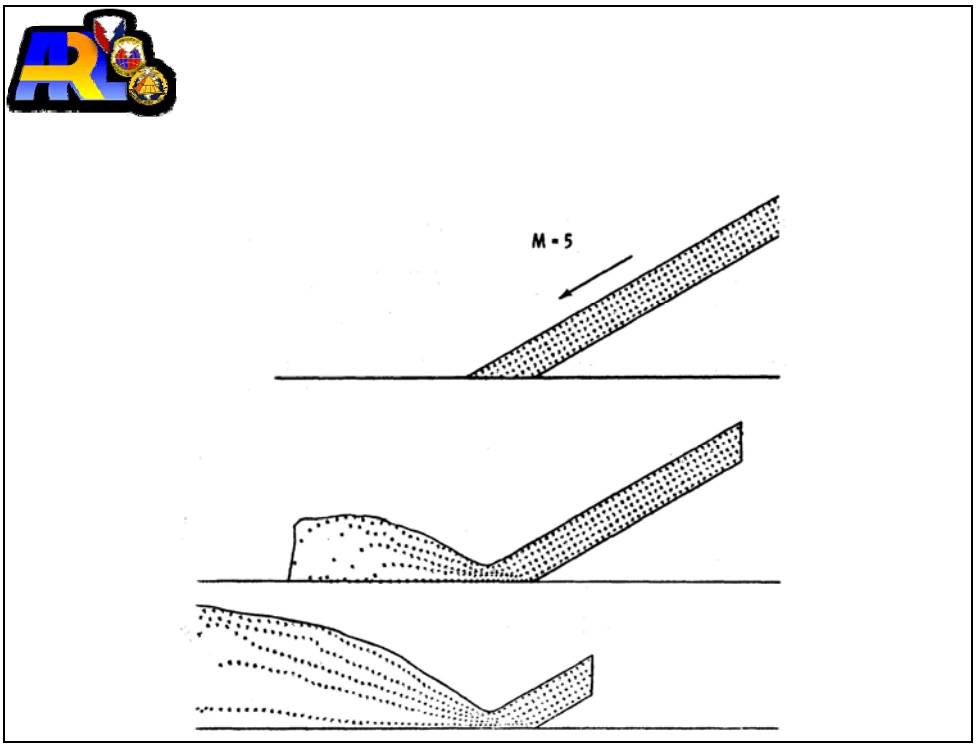

Figure 67. Supersonic wedge collapse, jetless configuration, stiffened gas.

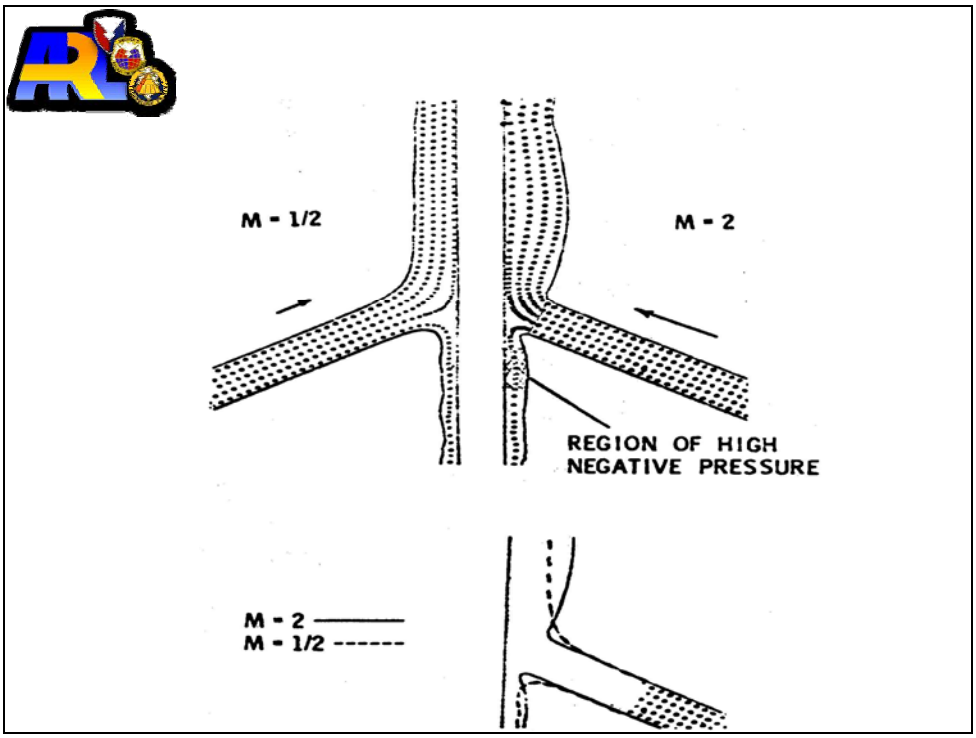

Figure 68. Comparison of jets from supersonic and subsonic collapse.

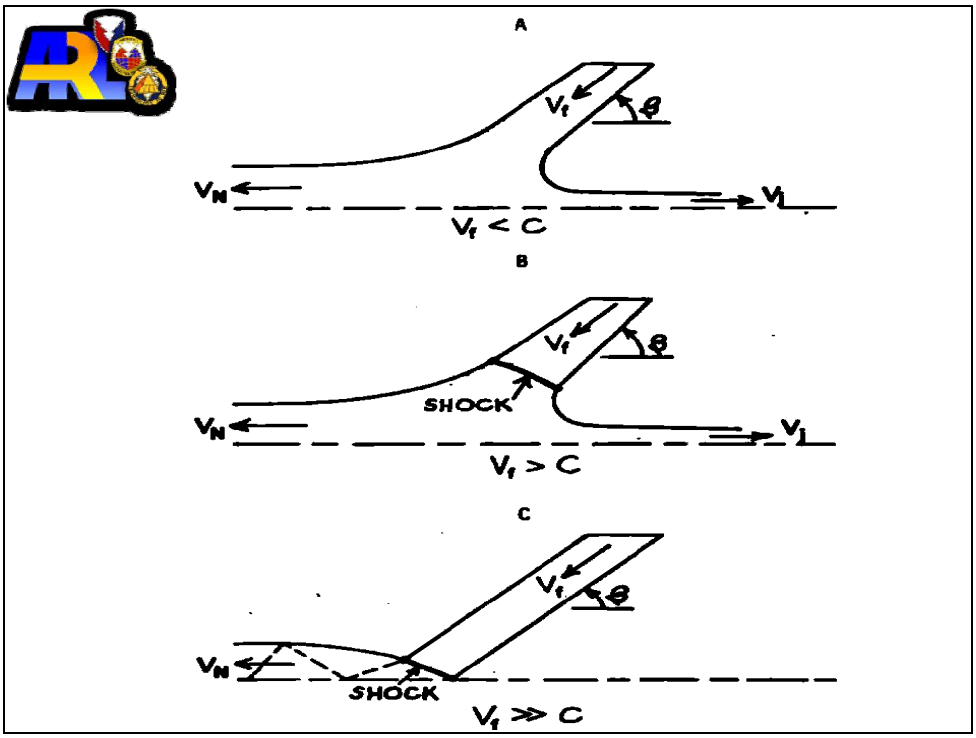

Figure 69. Comparison of jets from supersonic and subsonic collapse (continued).

The bulk speed of sound is

$$C_b = \sqrt{\left(V_L^2 - \frac{4}{3}V_S^2\right)},$$

where V_L is the longitudinal speed of sound and V_S is the shear speed of sound

Figure 70. The bulk speed of sound.

1. For subsonic collisions (or the collision velocity V<C, the material bulk speed of sound), a solid coherent jet always forms.

2. For supersonic collisions (V>C), jetting occurs if β > βc, but the jet is not coherent. The angle βc is the maximum angle that an attached shock wave can form at a prescribed supersonic velocity, V.

3. For supersonic collisions (V>C), but β < βc, a jet will not be formed.

Figure 71. Jetting criterion for plane axisymmetric cases.

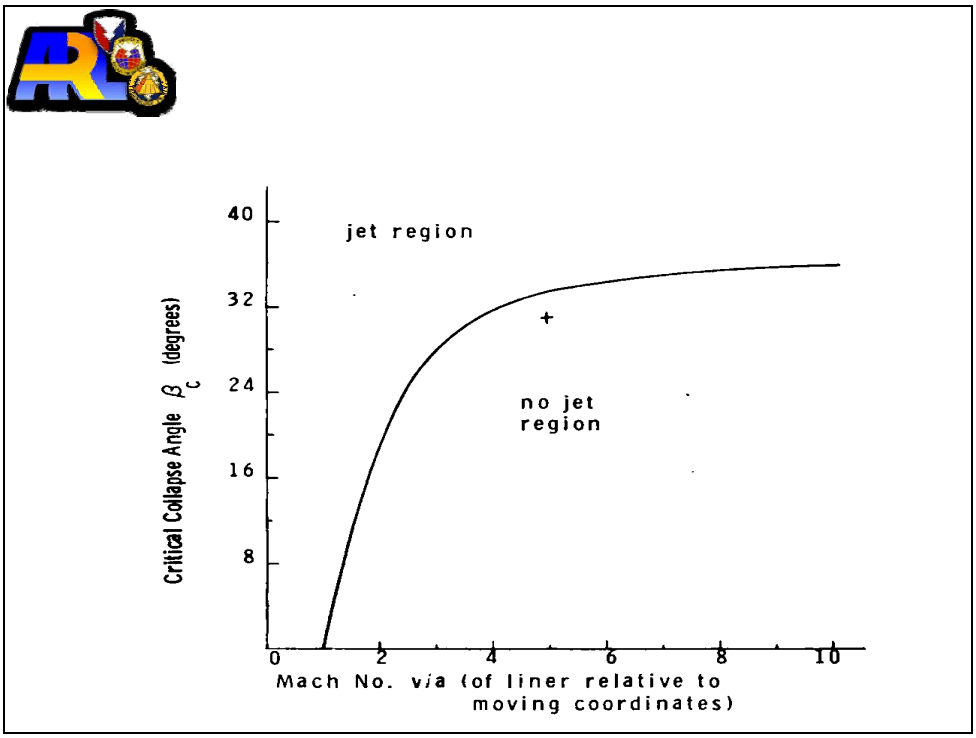

Figure 72. Jet/no jet curve for wedge collapse of a stiffened gas.

FOR A COHESIVE JET, FLOW INTO FORMATION REGION MUST BE SUBSONIC.

i.e., $M = \frac{v}{c} < 1$

c = LINER MATERIAL SOUND SPEED

FROM EXPERIMENTS,

$M < 1.1$ TO 1.25

Figure 73. Cohesive jet criterion.

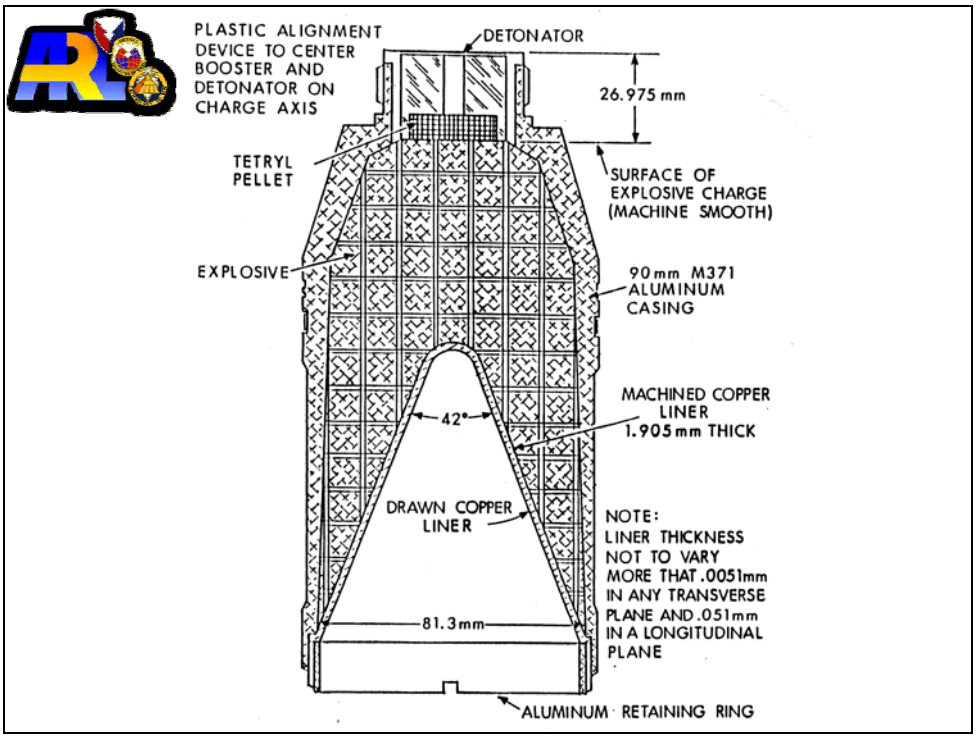

Figure 74. The 81.3-mm liner.

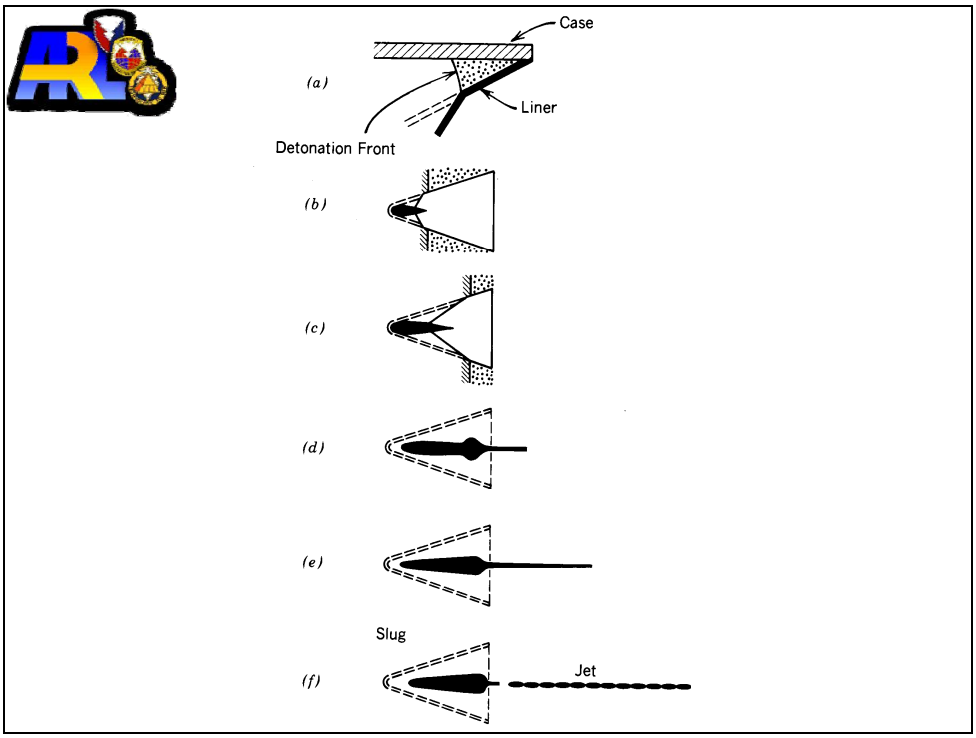

Figure 75. The jet collapse and formation.

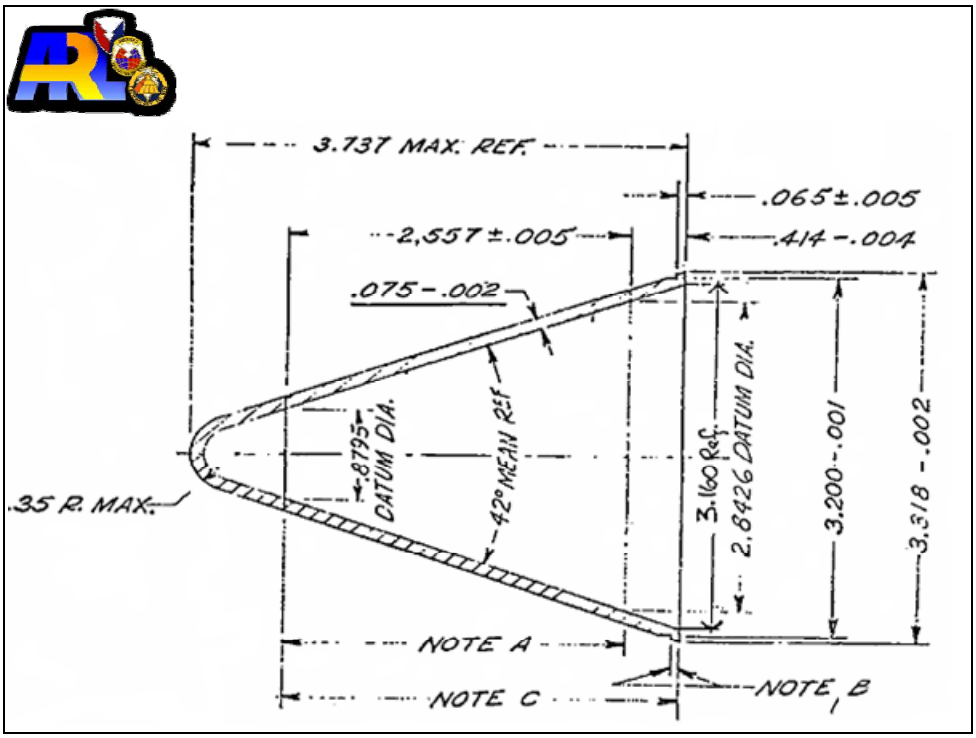

Figure 76. Liner drawing.

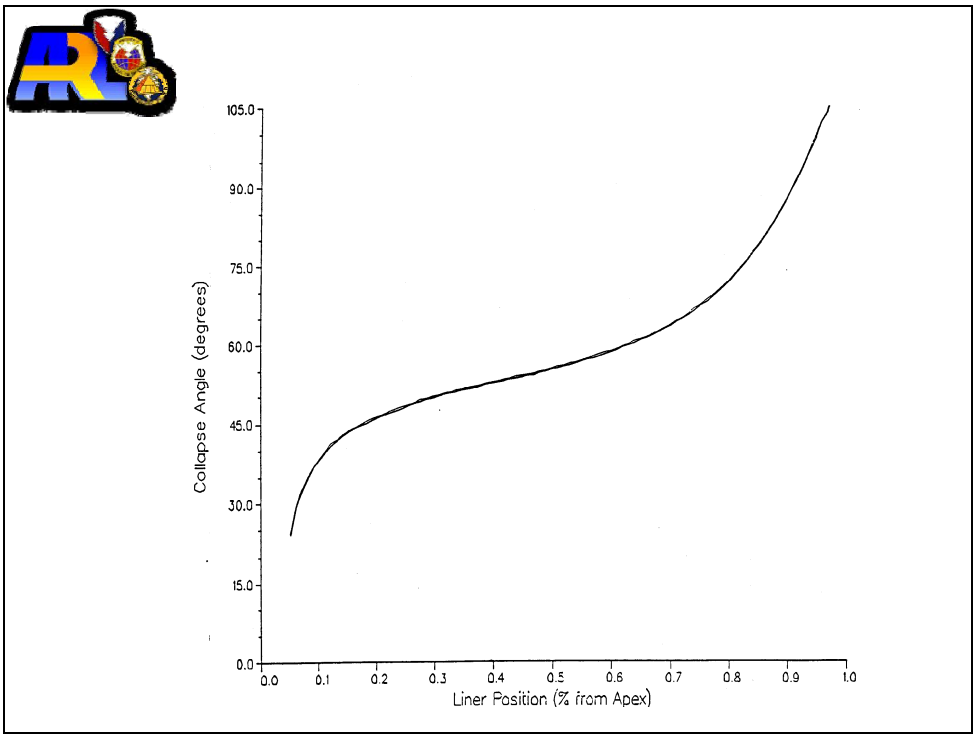

Figure 77. Collapse angle vs. liner position.

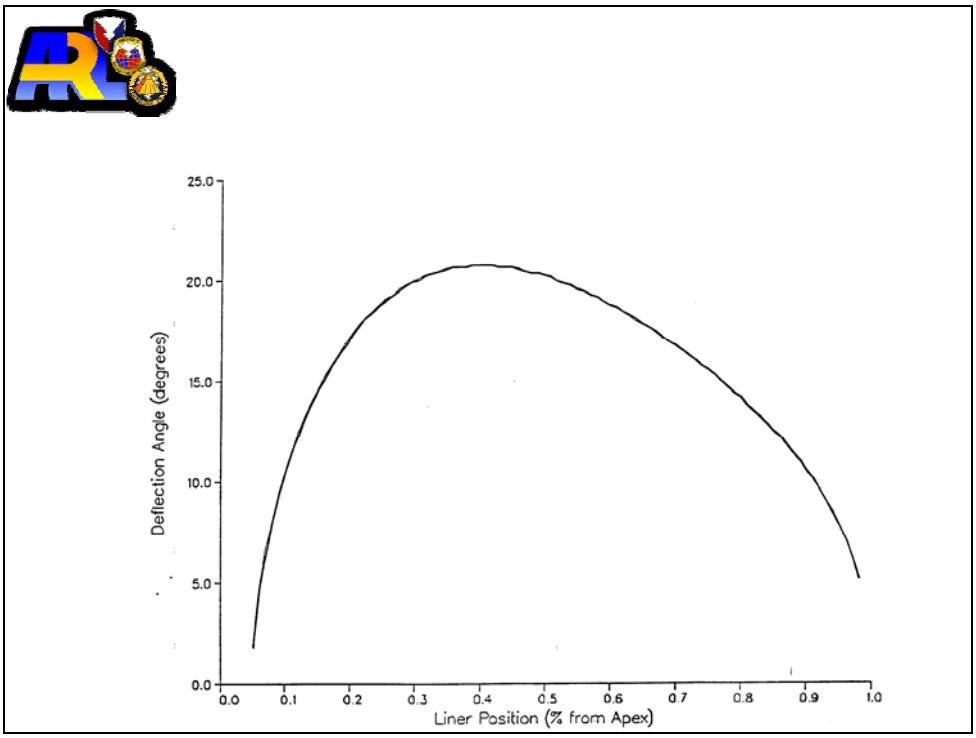

Figure 78. Deflection angle (Phi) vs. liner position.

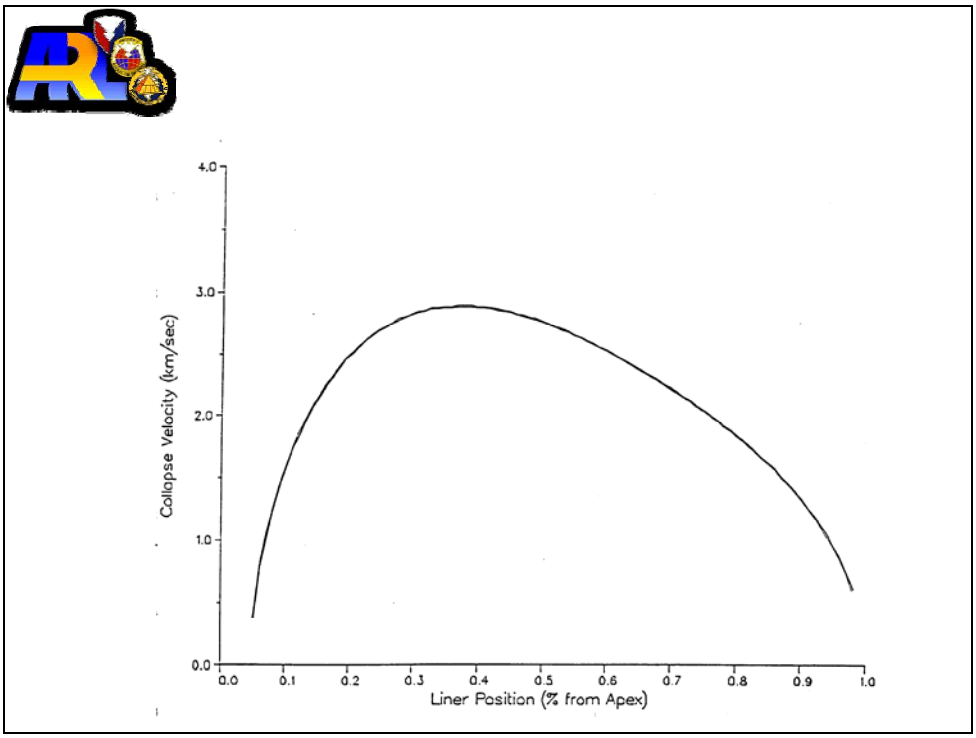

Figure 79. Collapse velocity vs. liner position.

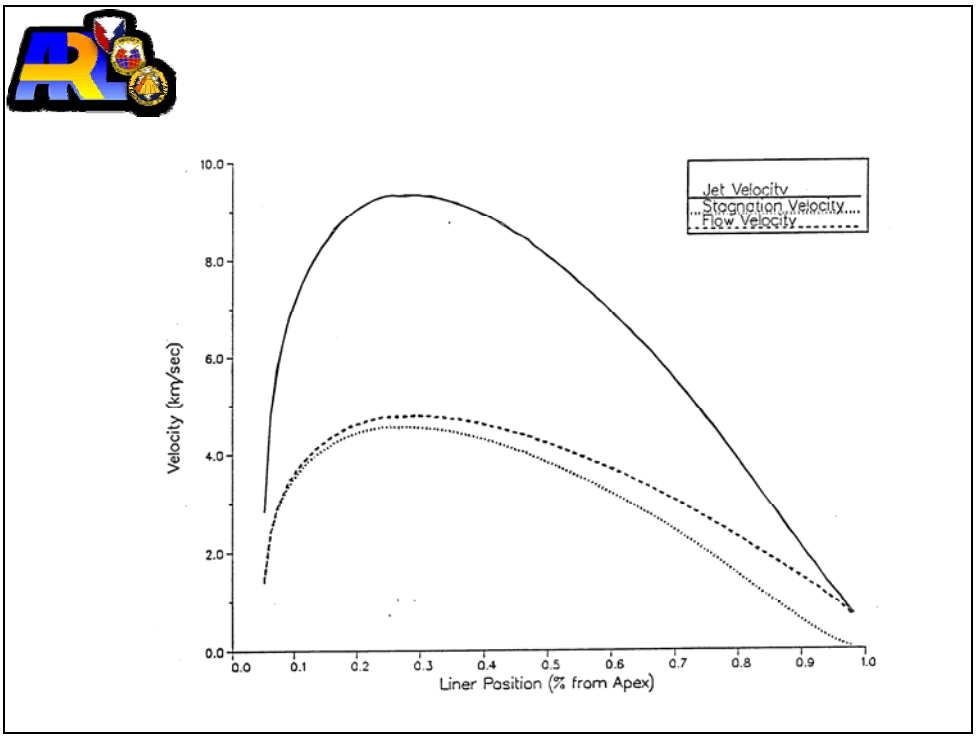

Figure 80. Jet formation velocities vs. liner position.

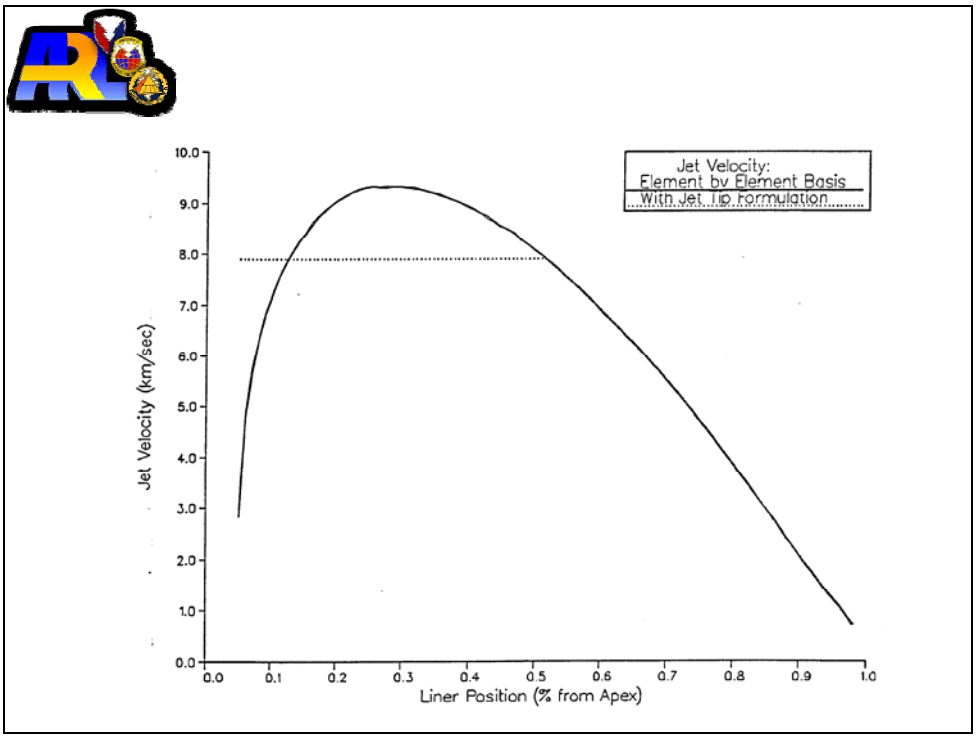

Figure 81. Jet velocity vs. liner position.

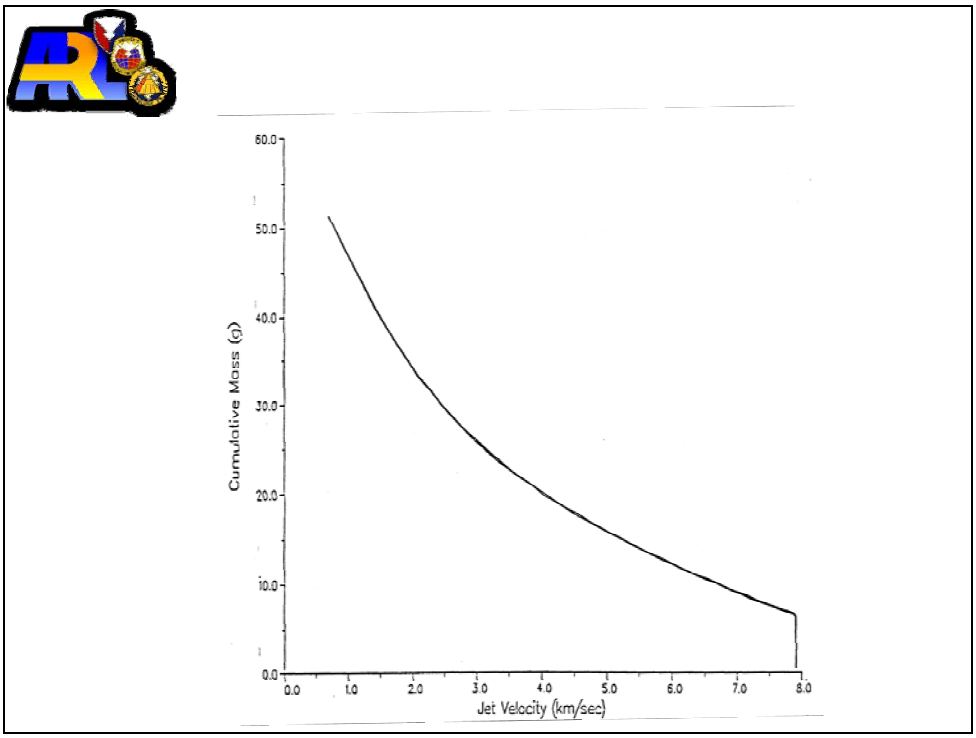

Figure 82. Cumulative jet mass vs. jet velocity.

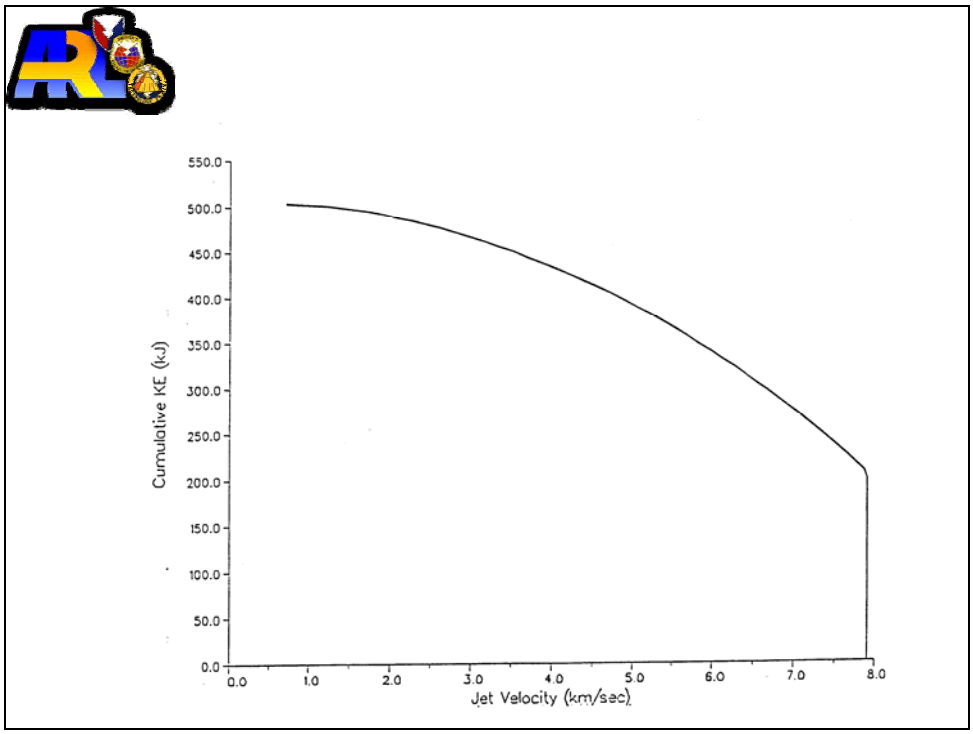

Figure 83. Cumulative KE vs. jet velocity.

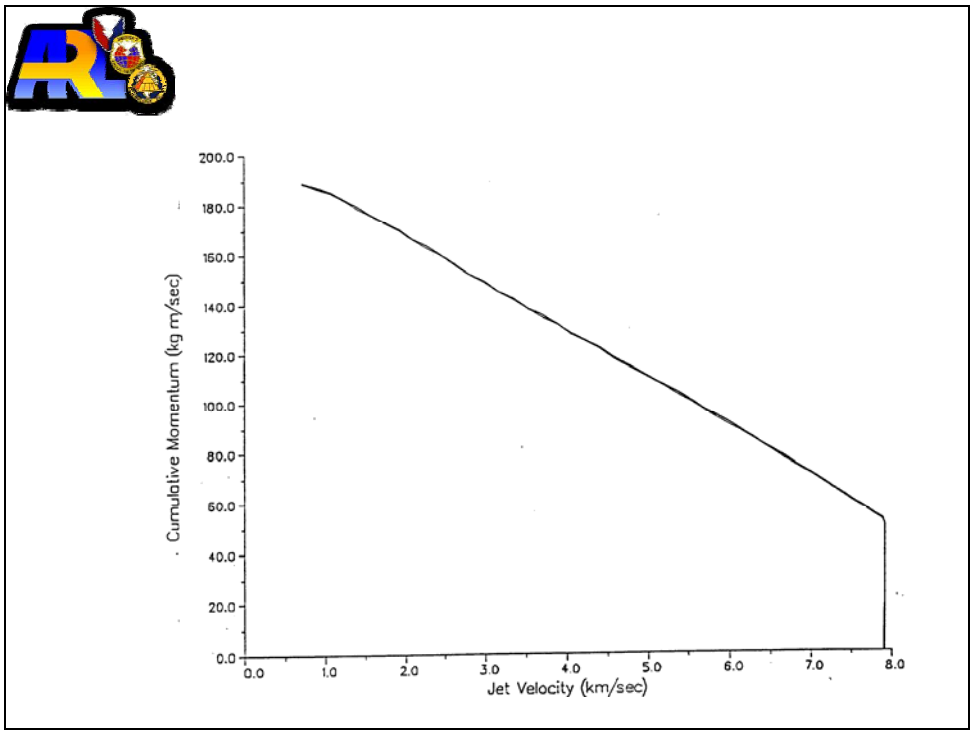

Figure 84. Cumulative momentum vs. jet velocity.

Experimental verification of the liner collapse and jet formation process as predicted by the HELP and EPIC-2 codes.

Figure 85. Experimental study of jet formation, objective.

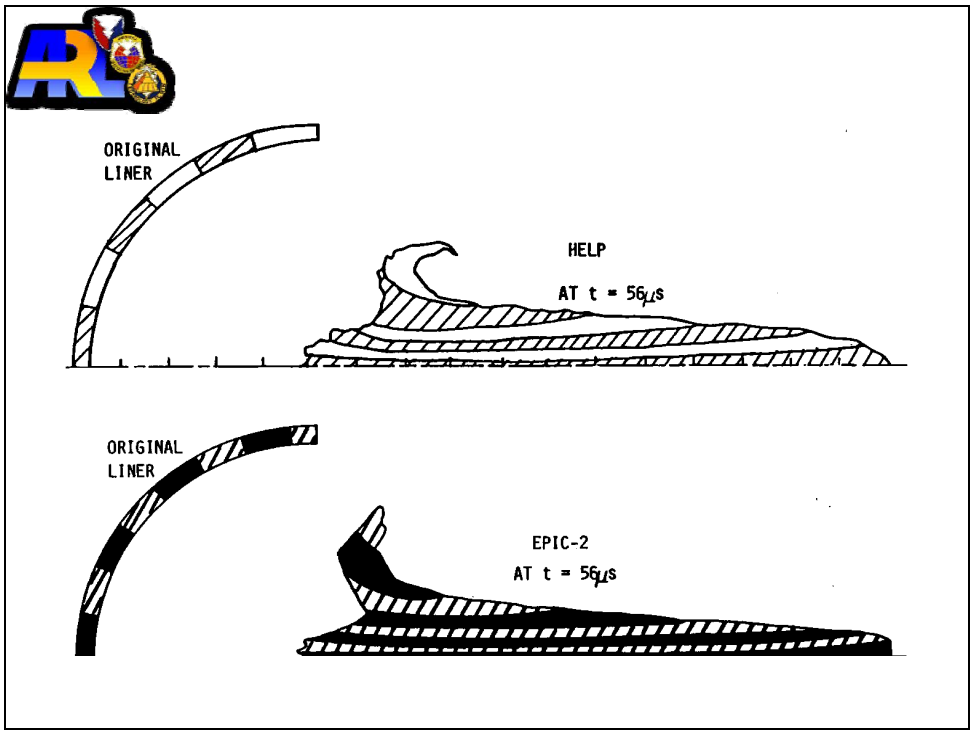

Figure 86. Comparison of HELP and EPIC-2 computer code simulations of jet formation from a hemispherical liner charge for the point initiation case at t = 56 μs after detonation.

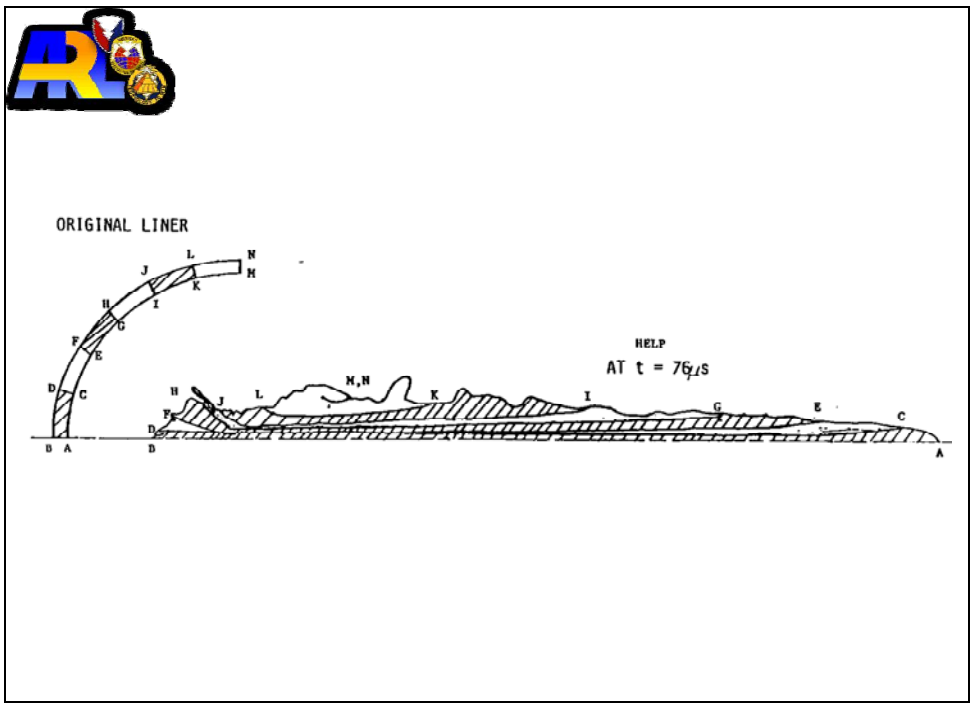

Figure 87. HELP code simulations of jet formation from a hemispherical liner charge for the initiation case at t = 67 μs after detonation.

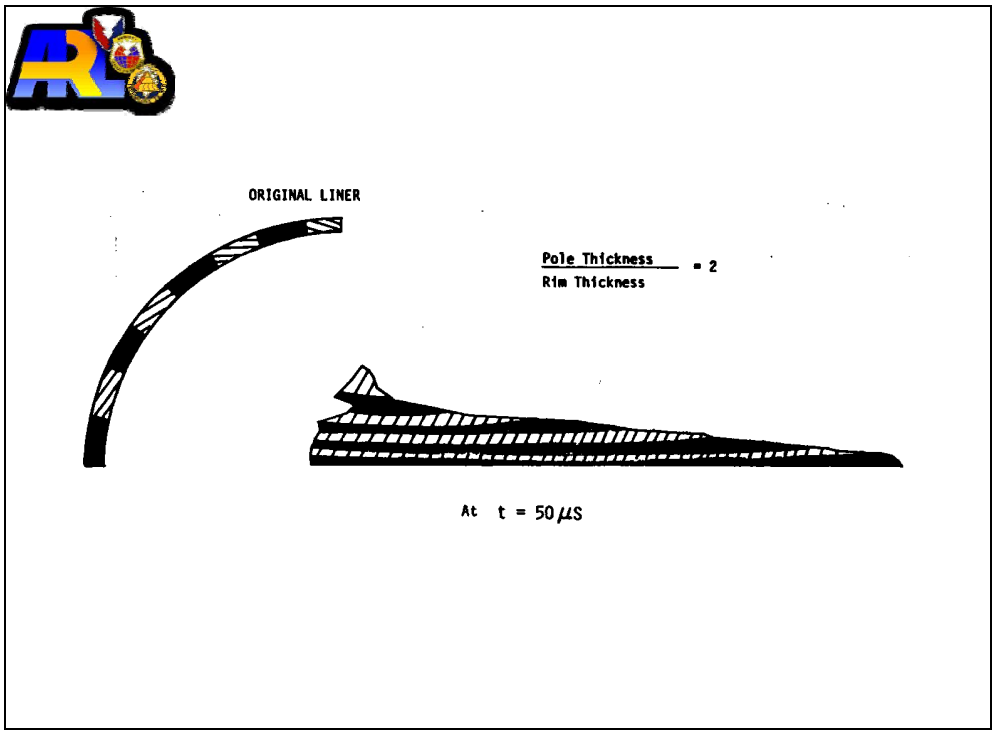

Figure 88. DEFEL code simulation of a thick-pole, tapered-wall, hemispherical liner charge.

The HELP and EPIC computer codes predict a layered tubular collapse of hemispherical liner elements. We seek experimental verification.

Figure 89. Experimental verification.

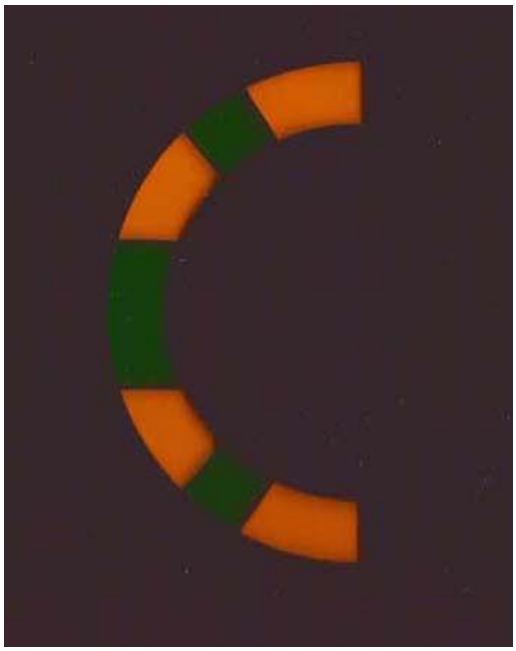

Figure 90. The desired liner.

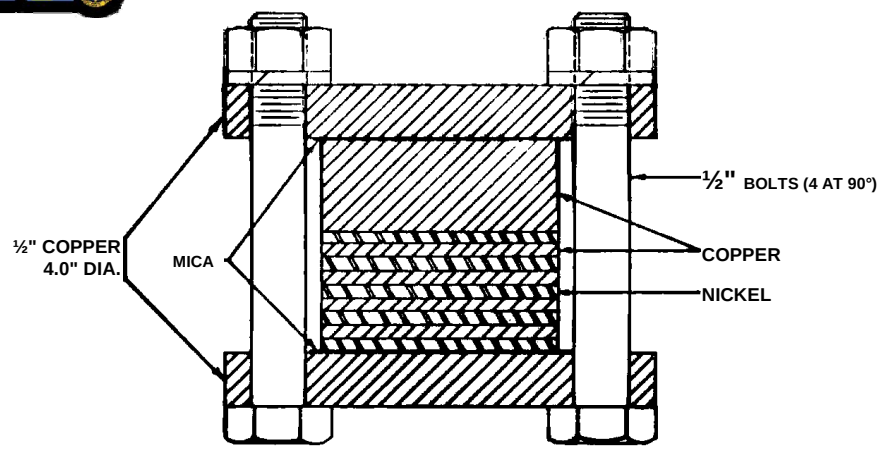

Figure 91. Setup for diffusion bonding of copper-nickel assemblies, temperature is 982 °C, time is 1–3 hr, argon atmosphere.

Figure 92. Diffusion-bonded alternately layered copper-nickel cylinder.

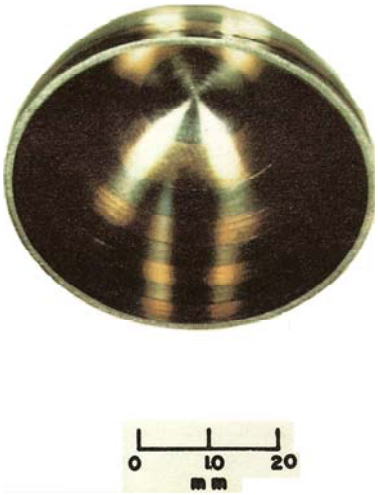

Figure 93. Finish-machined alternately layered copper-nickel hemisphere.

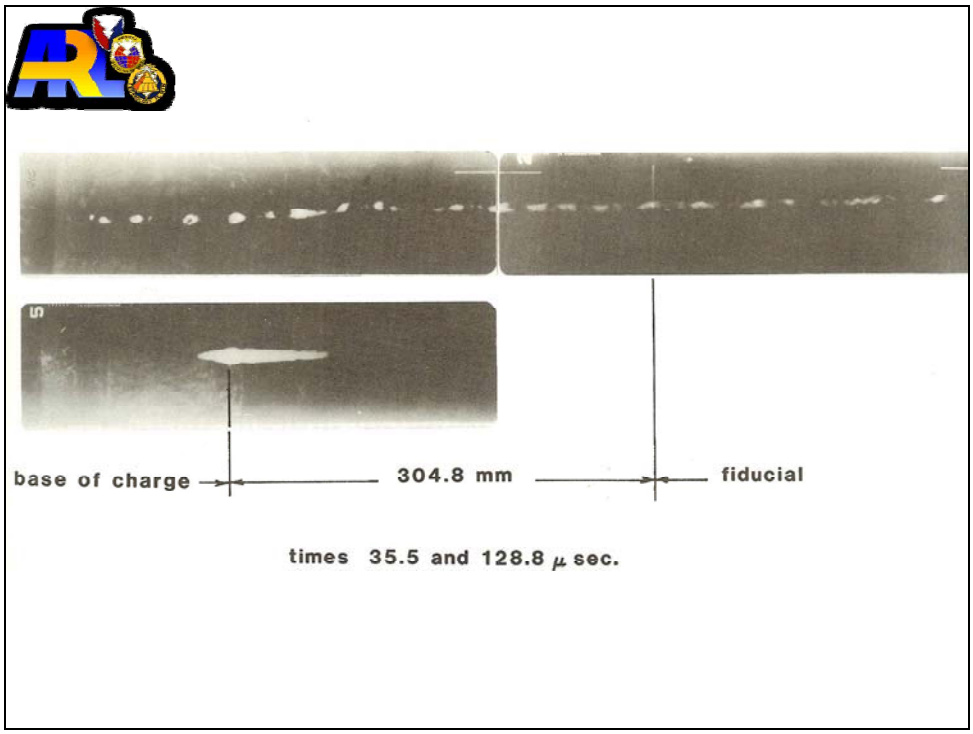

Figure 94. Flash radiograph of the jet from a hemispherical liner.

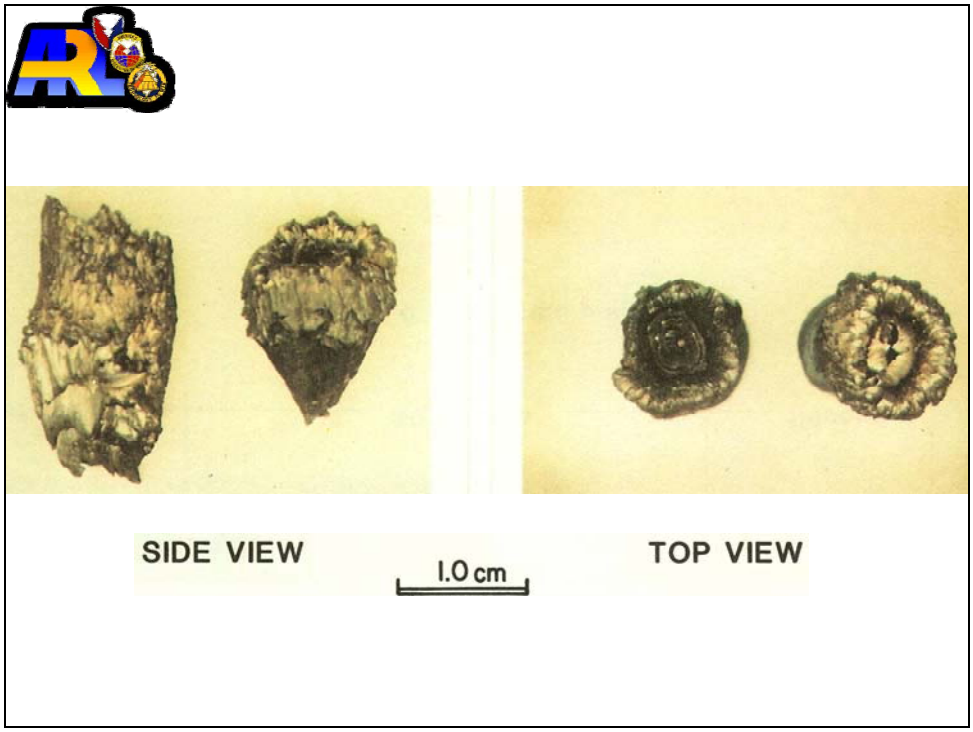

Figure 95. Recovered jet particles from an alternately layered copper-nickel hemispherical liner.

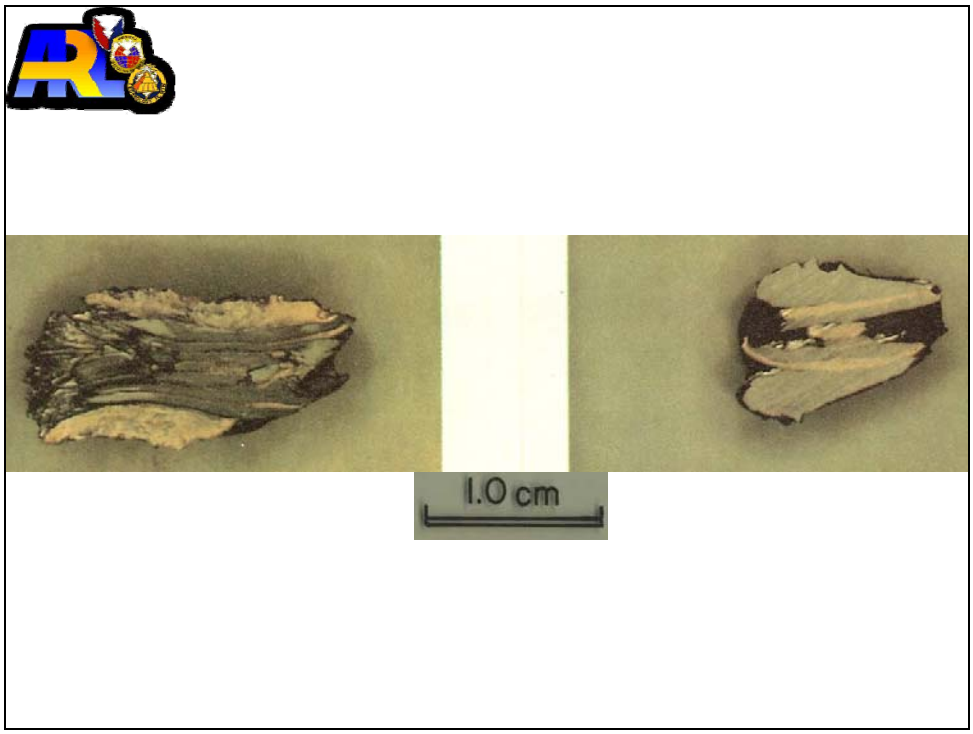

Figure 96. Cross section of recovered jet particles from an alternately layered copper-nickel hemispherical liner.

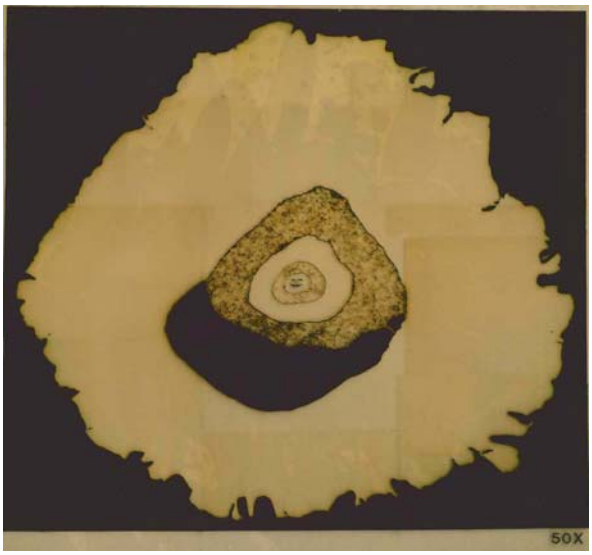

Figure 97. Cross section of jet particle from alternately layered copper-nickel hemispherical liner.

Figure 98. Cross section of one half of a recovered jet particle from an alternately layered copper-nickel hemispherical shaped-charge liner.

Figure 99. Central region of alternately layered copper-nickel hemispherical liner.

For point-initiated, uniform wall, hemispherical liners, the experimental and analytical results appear to be in agreement.

Figure 100. Conclusion.

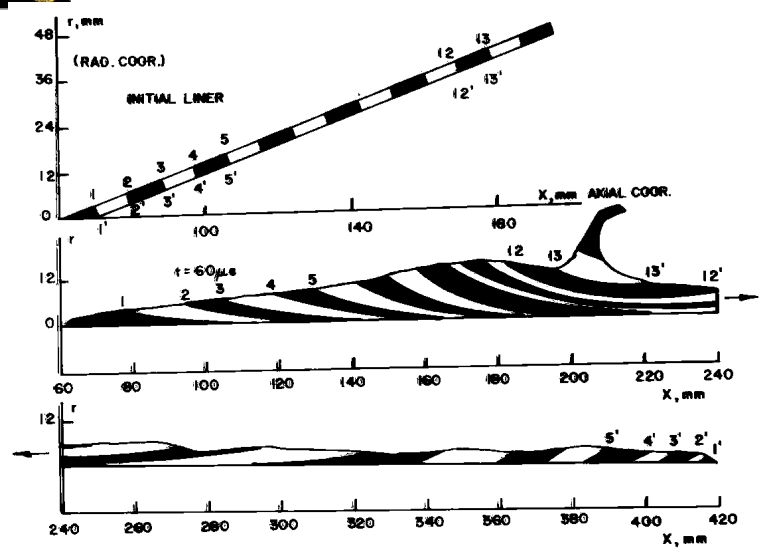

Figure 101. HELP code simulation of a 42° conical-liner charge, initial liner geometry (top), and jet and slug at 60 μs (center and bottom).

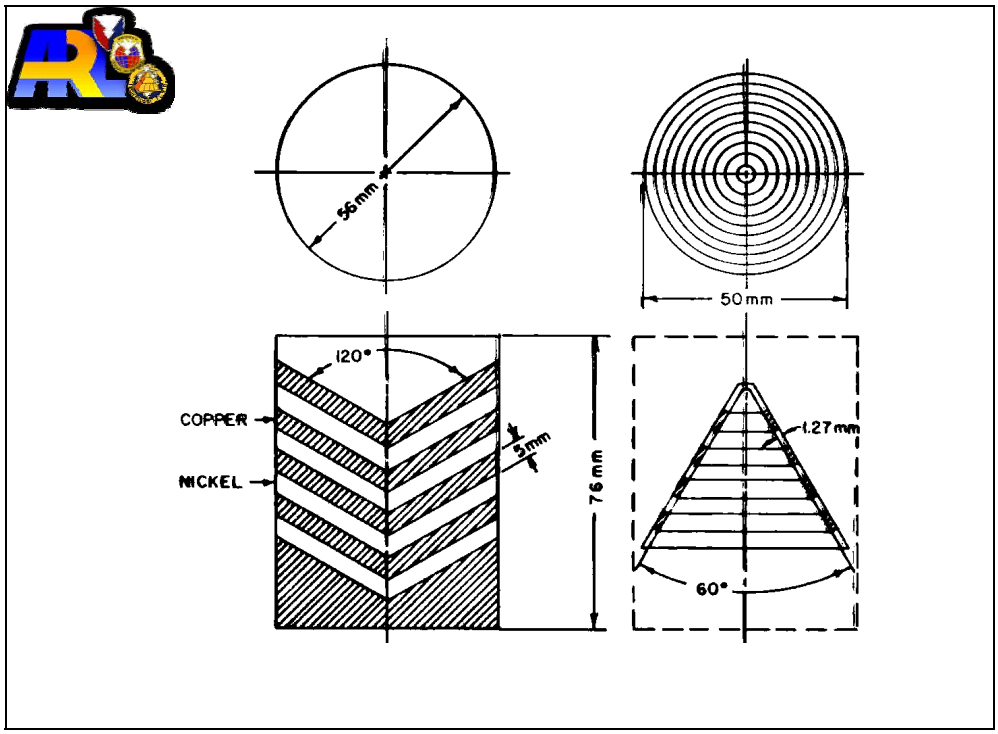

Figure 102. Diffusion bonding setup for fabricating alternately layered copper-nickel cones.

Figure 103. Finish-machined alternately layered copper-nickel cone.

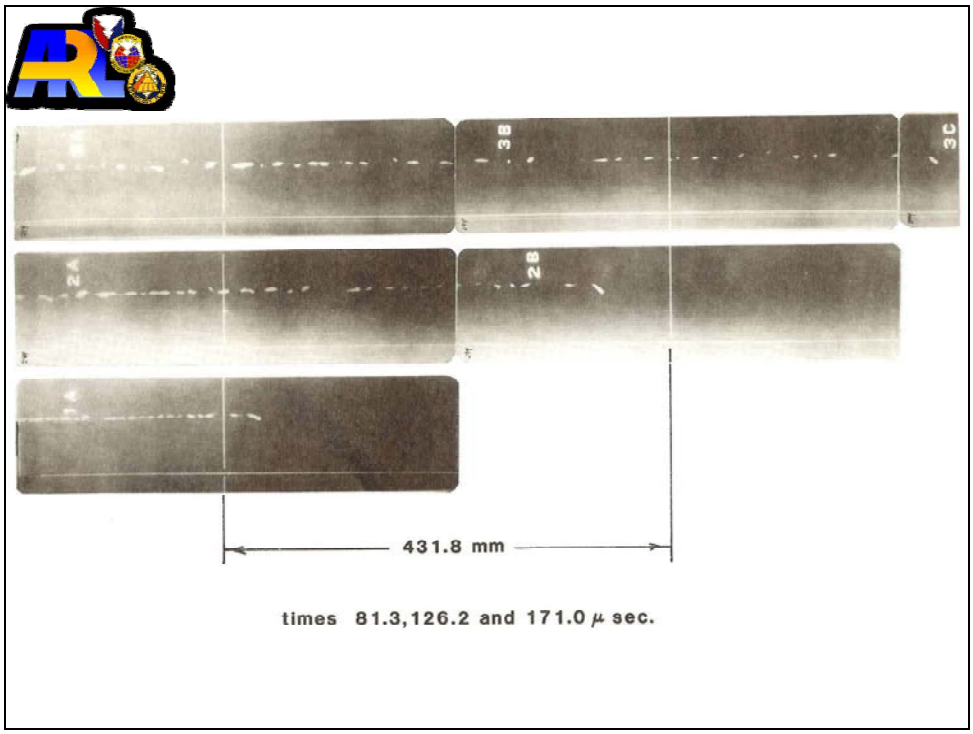

Figure 104. Flash radiograph of the jet from a conical liner.

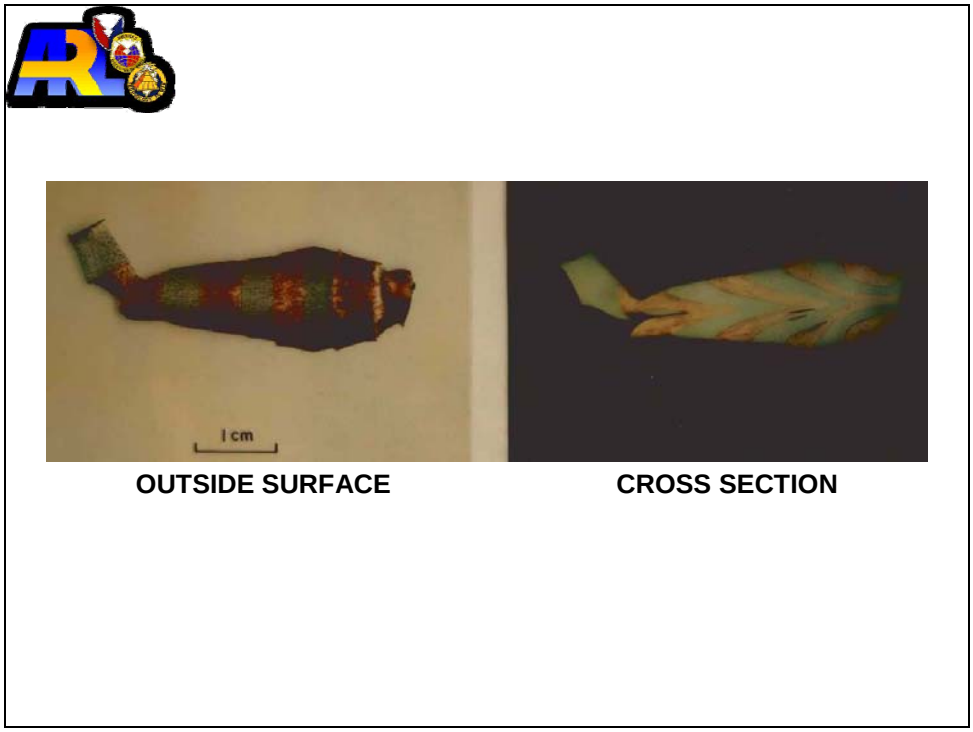

Figure 105. Recovered slug from alternately layered copper-nickel cone.

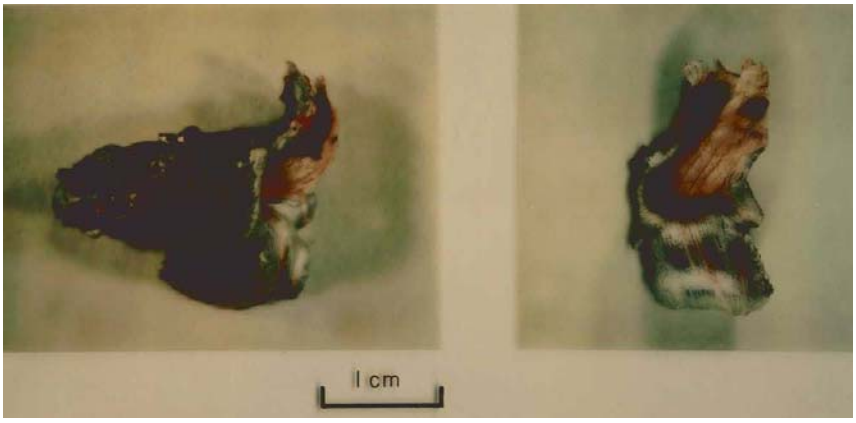

Figure 106. Jet particle from alternately layered copper-nickel cone.

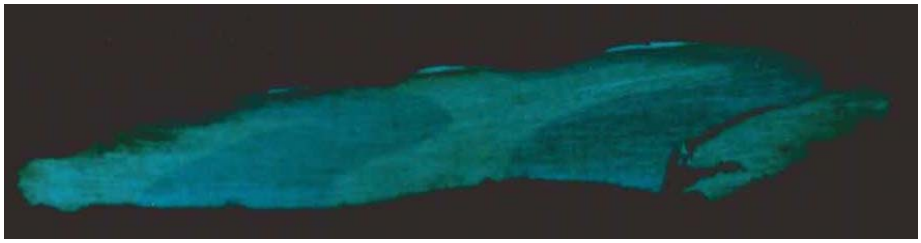

Figure 107. Cross section of a jet particle from alternately layered copper-nickel cone.

- Explosively formed penetrators
- Self-forging fragments
- Ballistic discs
- Miznay-Schardin devices

Figure 108. Explosively formed penetrator (EFP) study.

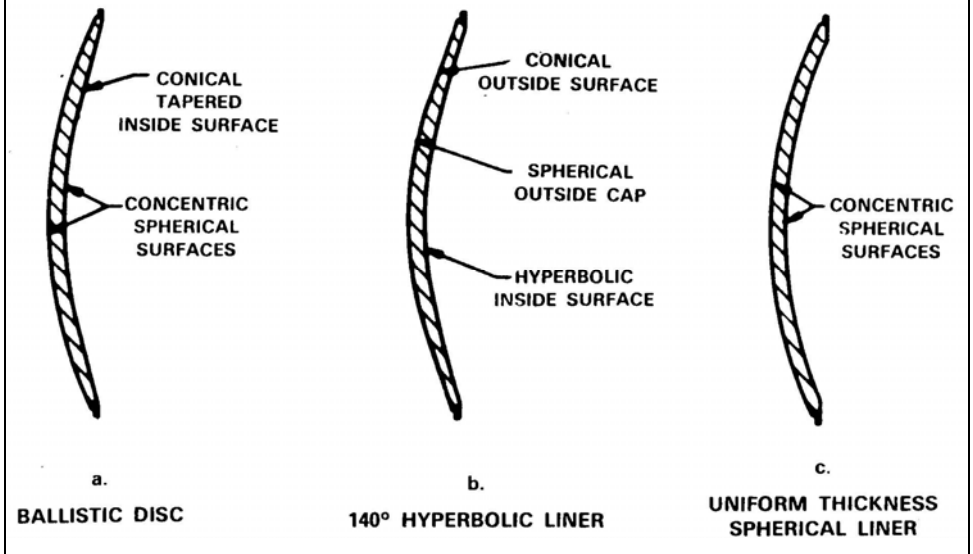

Figure 109. EFPs.

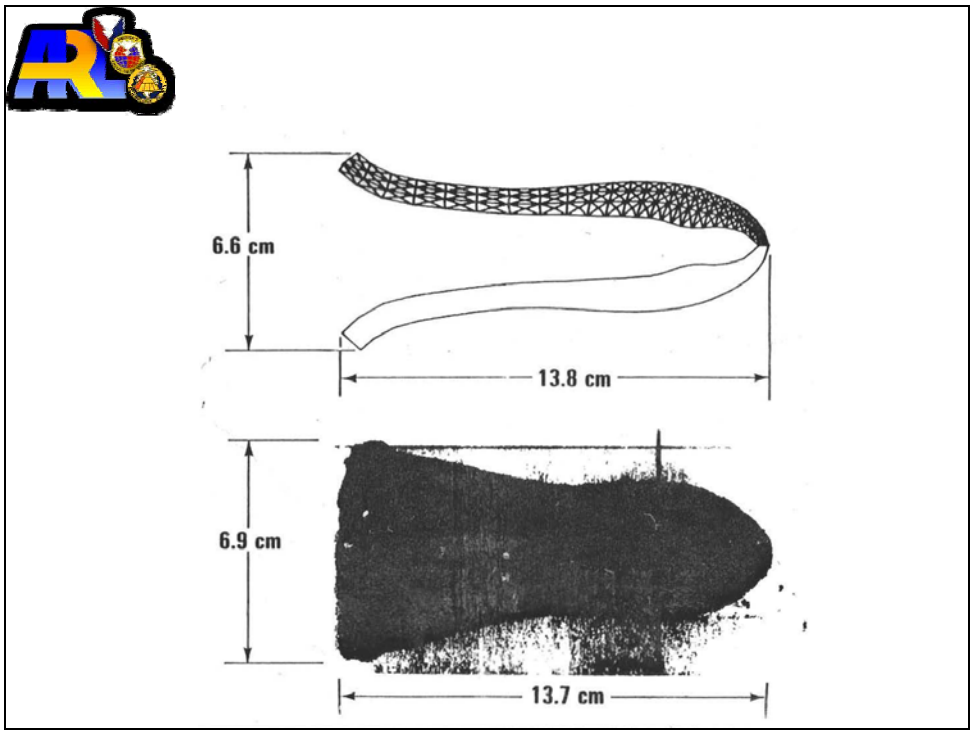

Figure 110. State-of-the-art copper explosively formed penetrator.

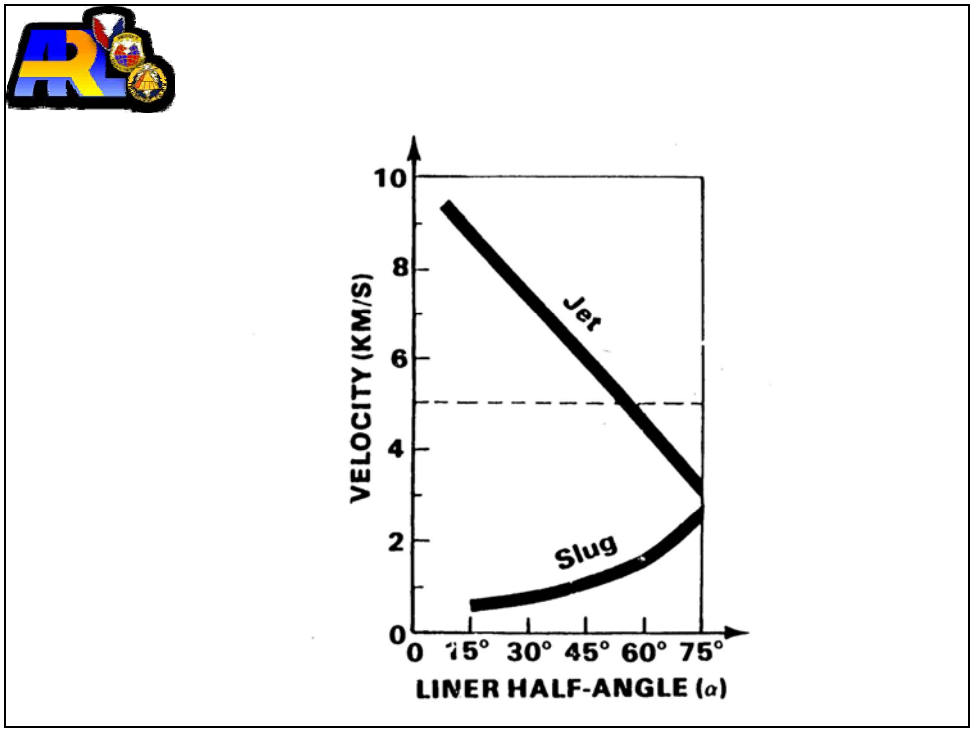

Figure 111. Jet/slug velocity vs. liner half angle.

Figure 112. The effect of apex angle on the jet formation.

- **Compact ball**
  - **W-fold: form liner into "W" shape and collapse upon itself**
  - **Point focus: focus all liner material into one point**
- **Long rod**
  - **Forward fold**
  - **Backward fold**

Figure 113. Formation types.

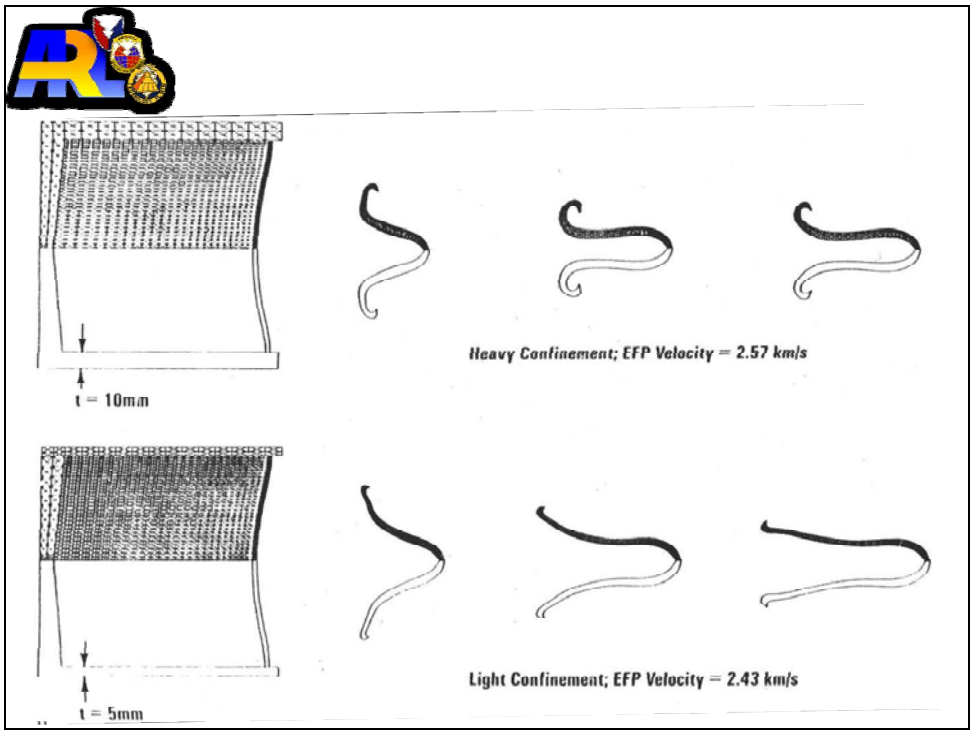

Figure 114. Heavy vs. light explosive/liner confinement.

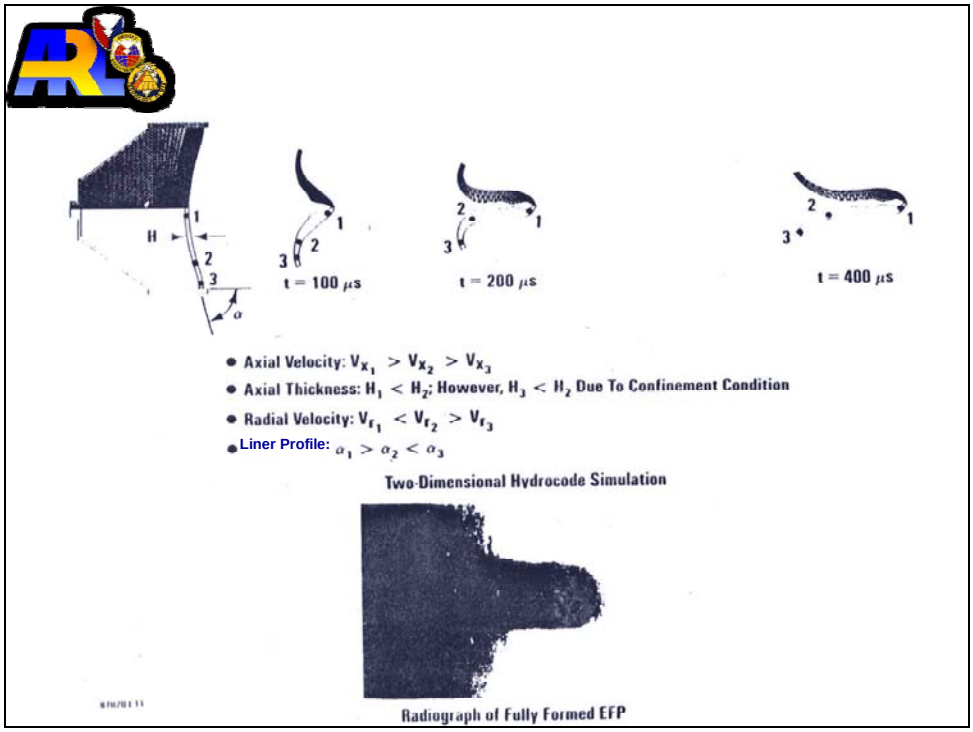

Figure 115. Rearward-fold liner formation.

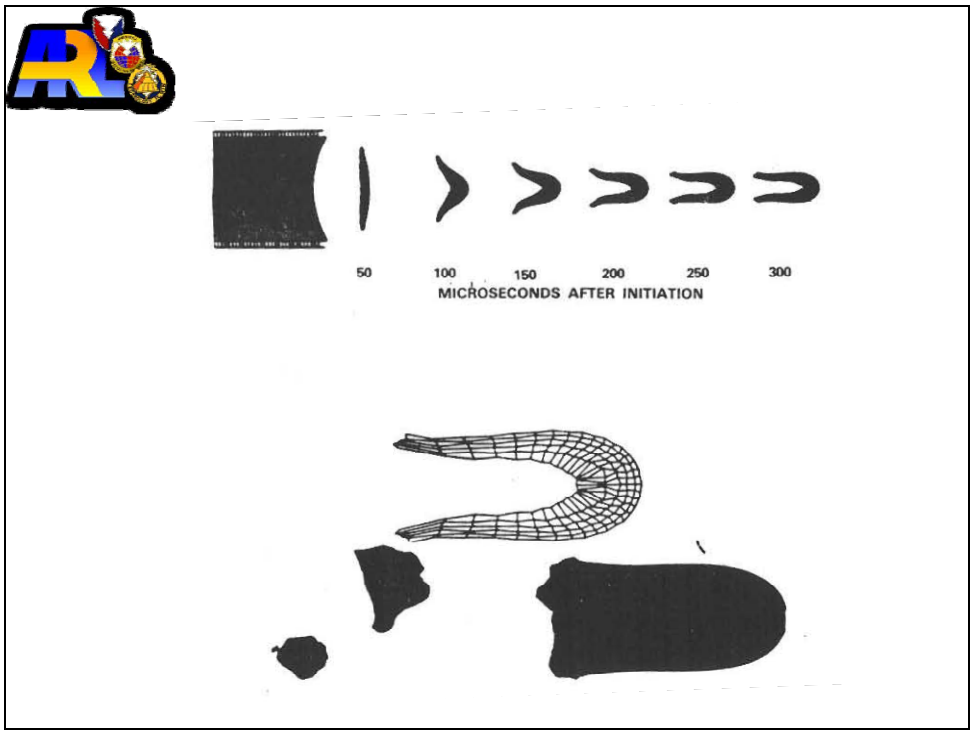

Figure 116. Rearward-fold liner formation (continued).

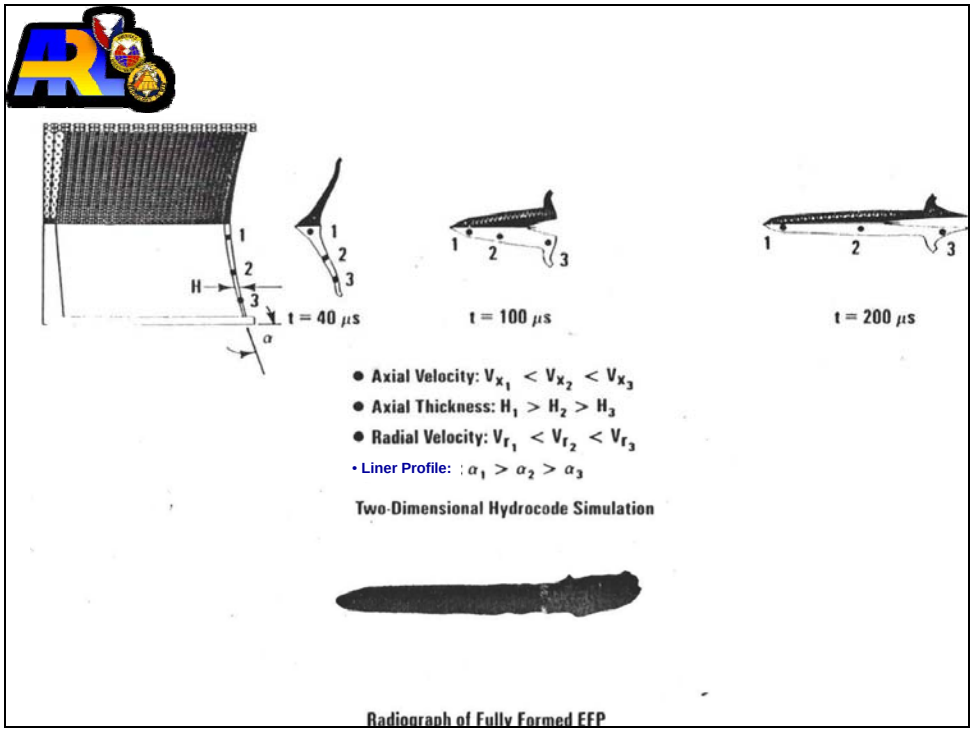

Figure 117. Forward-fold liner formation.

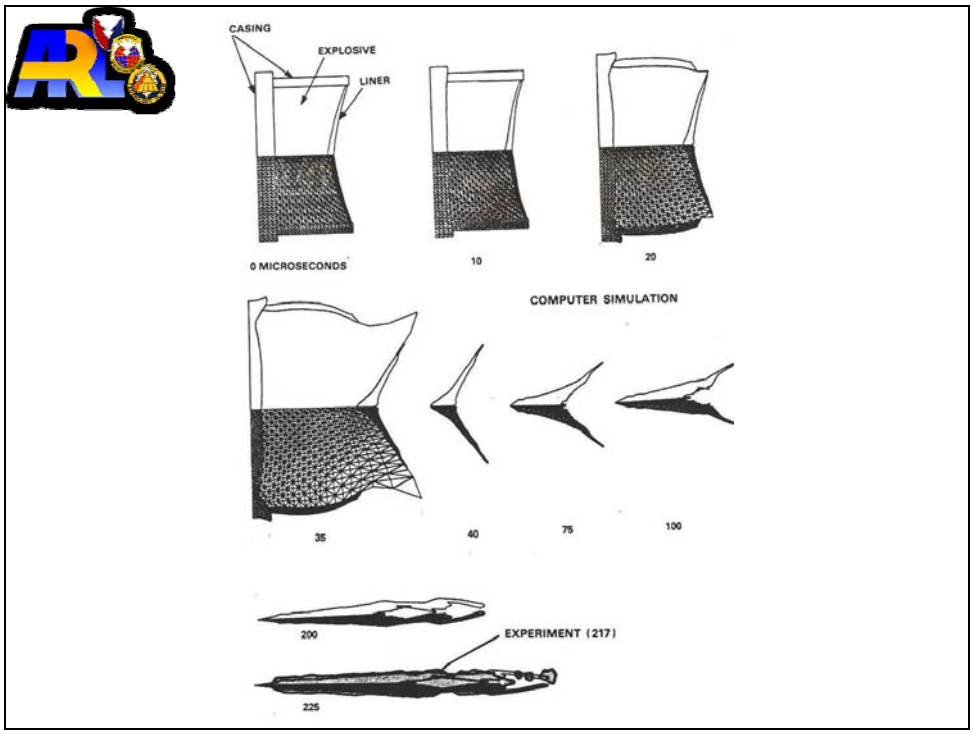

Figure 118. Forward-fold liner formation (continued).

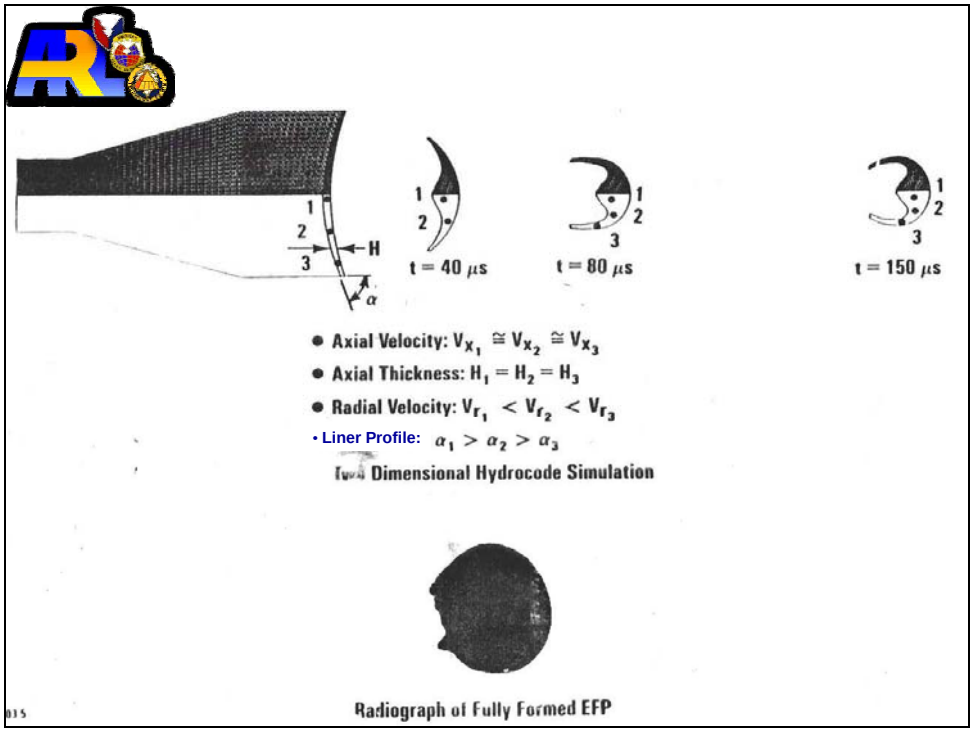

Figure 119. Point-focus liner formation.

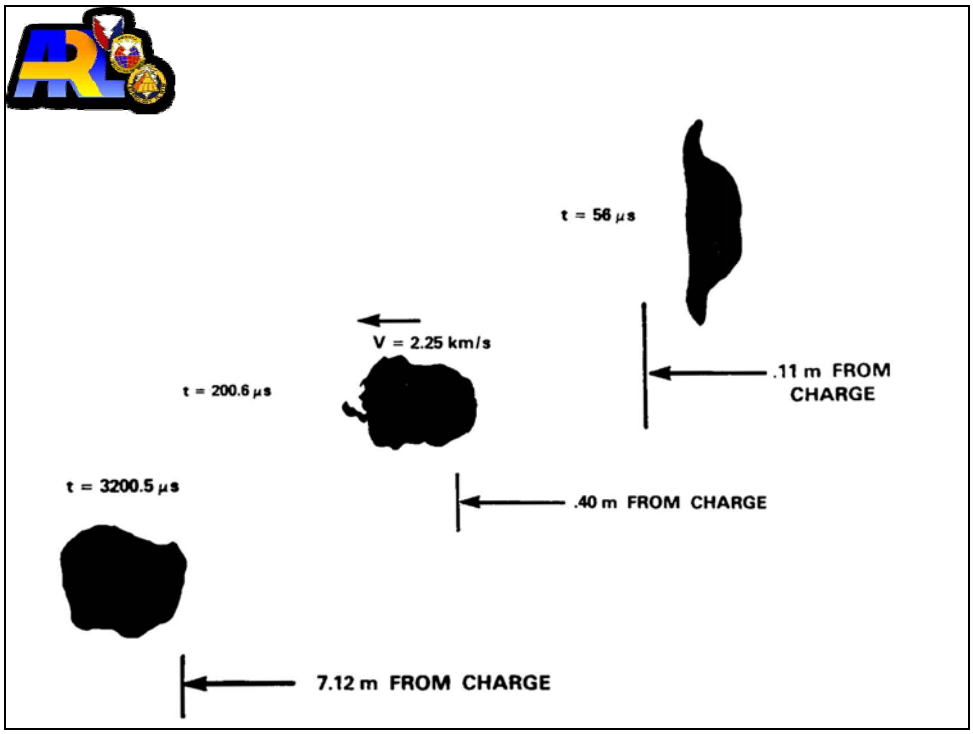

Figure 120. Point-focus liner formation (continued).

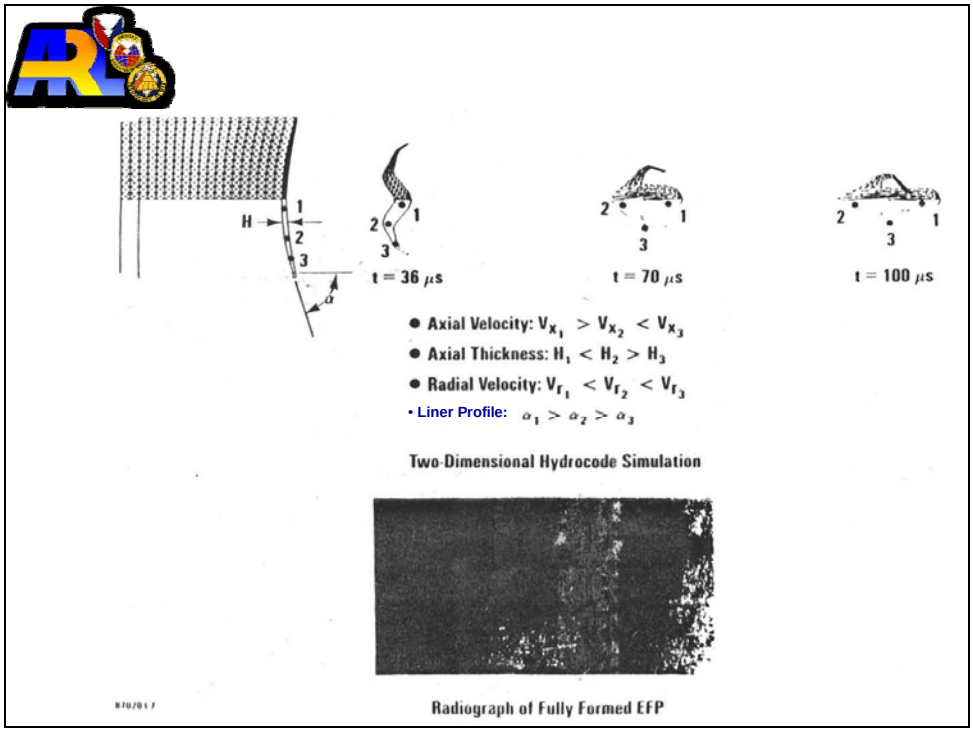

Figure 121. W-fold liner formation.

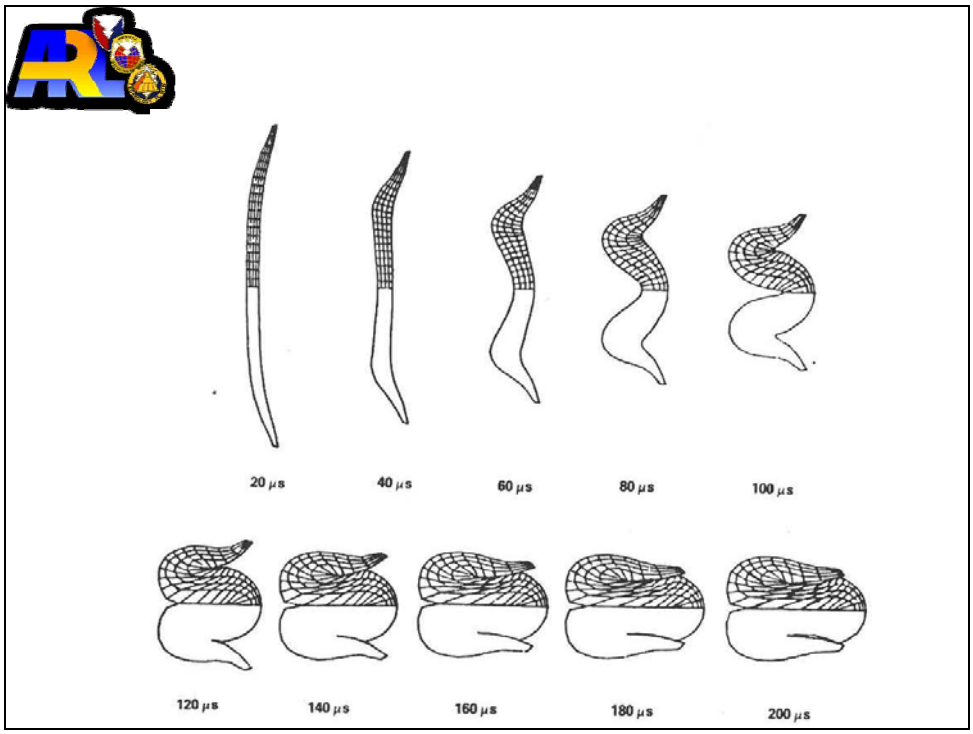

Figure 122. W-fold liner formation (continued).

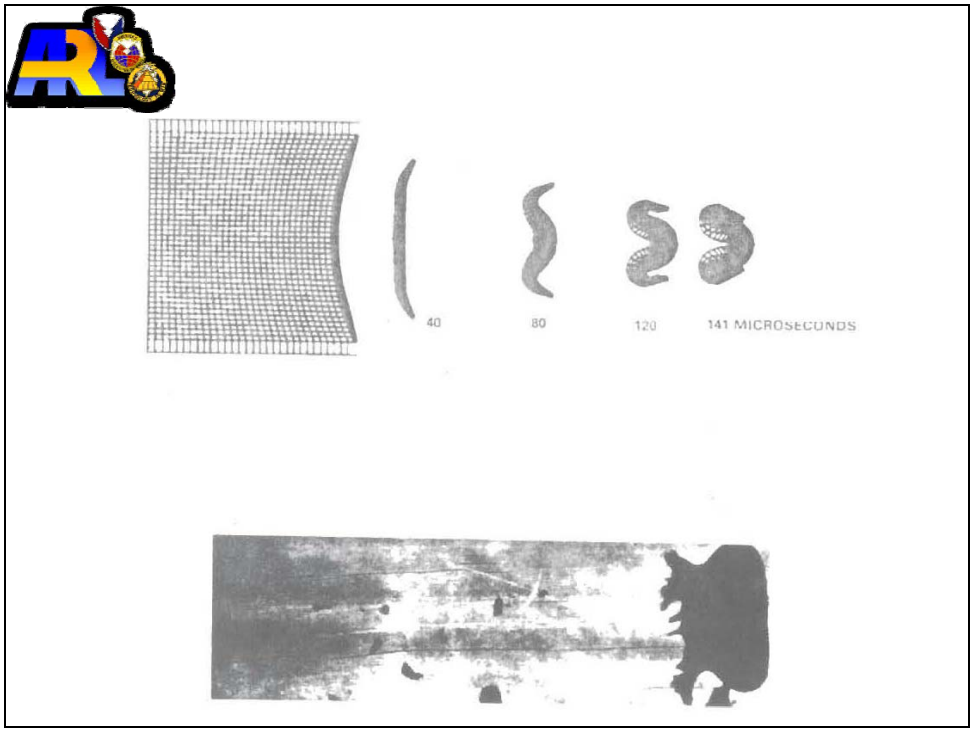

Figure 123. W-fold liner formation (continued).

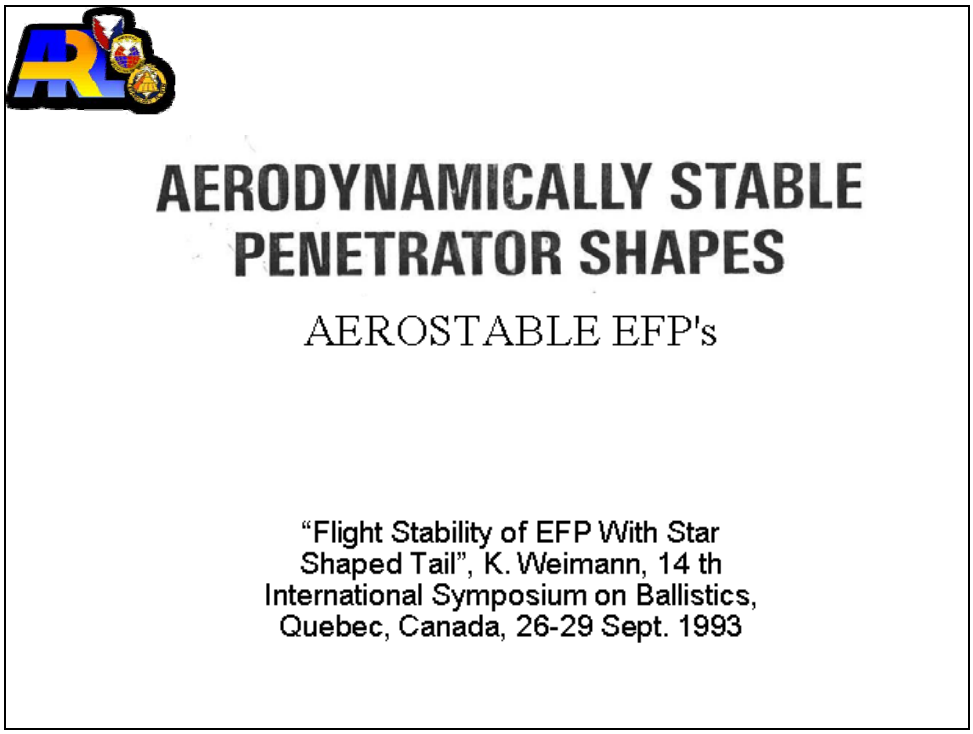

Figure 124. Aerostable EFPs.

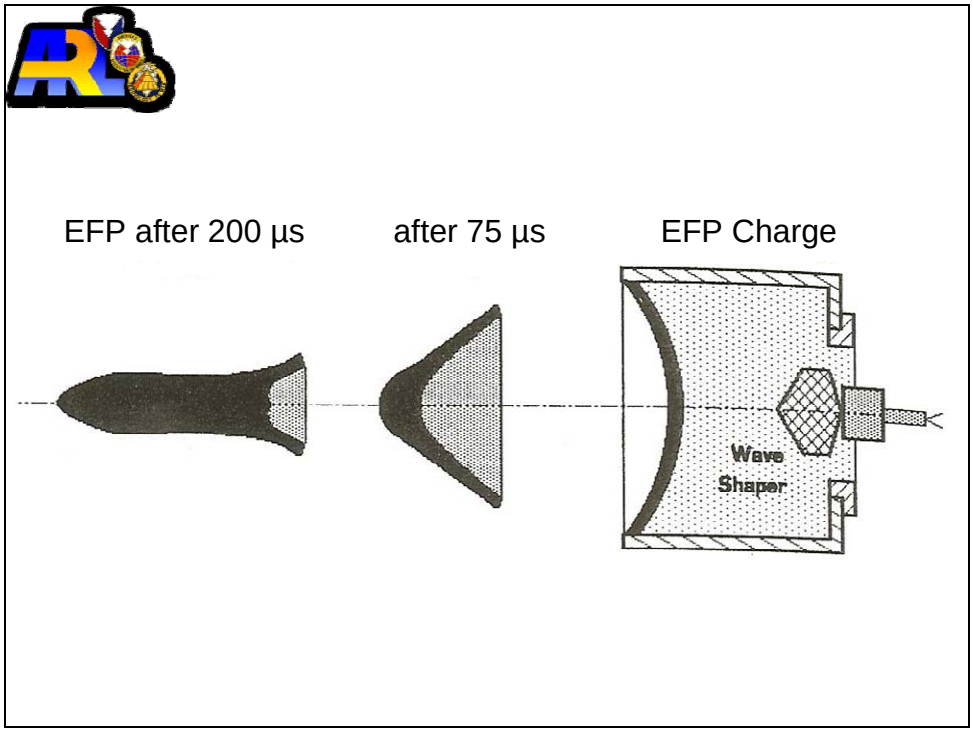

Figure 125. A generic EFP charge to form EFPs.

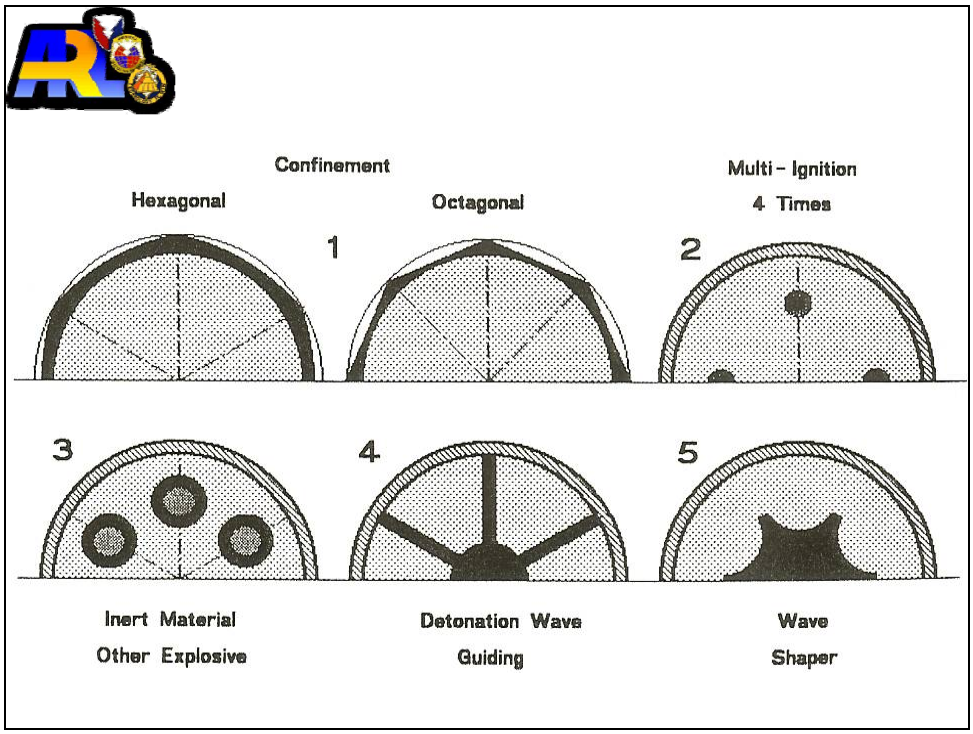

Figure 126. Ways to form EFPs with star-shaped tail.

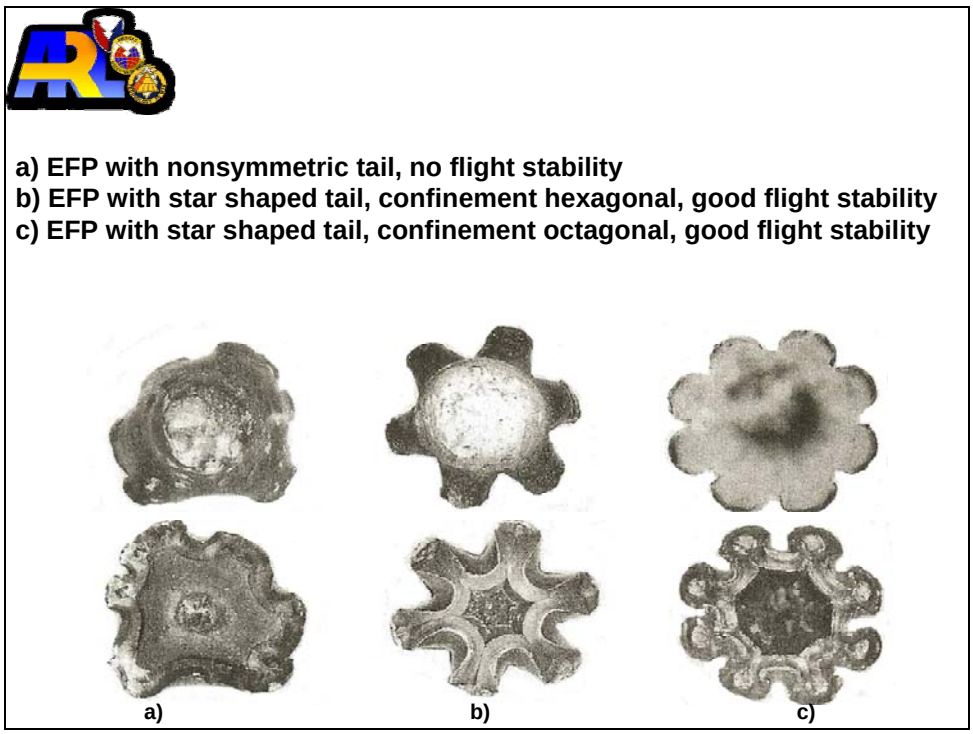

Figure 127. Front and back view of three projectiles produced with an EFP charge caliber 75 mm, explosive composition B, and liner material armco iron.

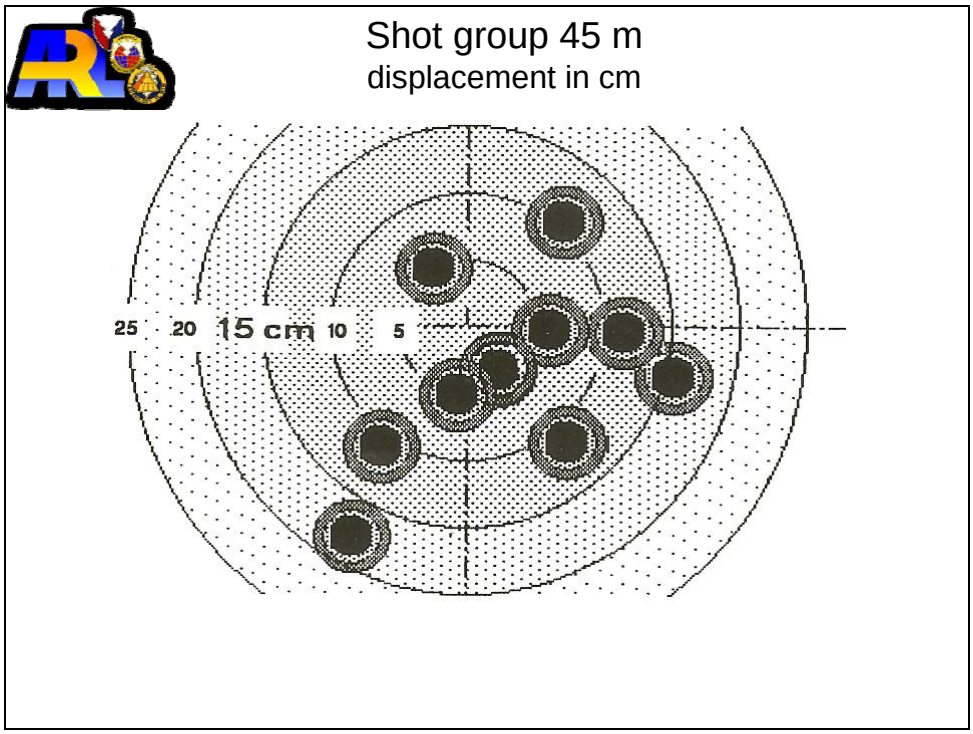

Figure 128. Hit precision of EFP with star-shaped tail at 45 m. The displacement was less than 20 cm.

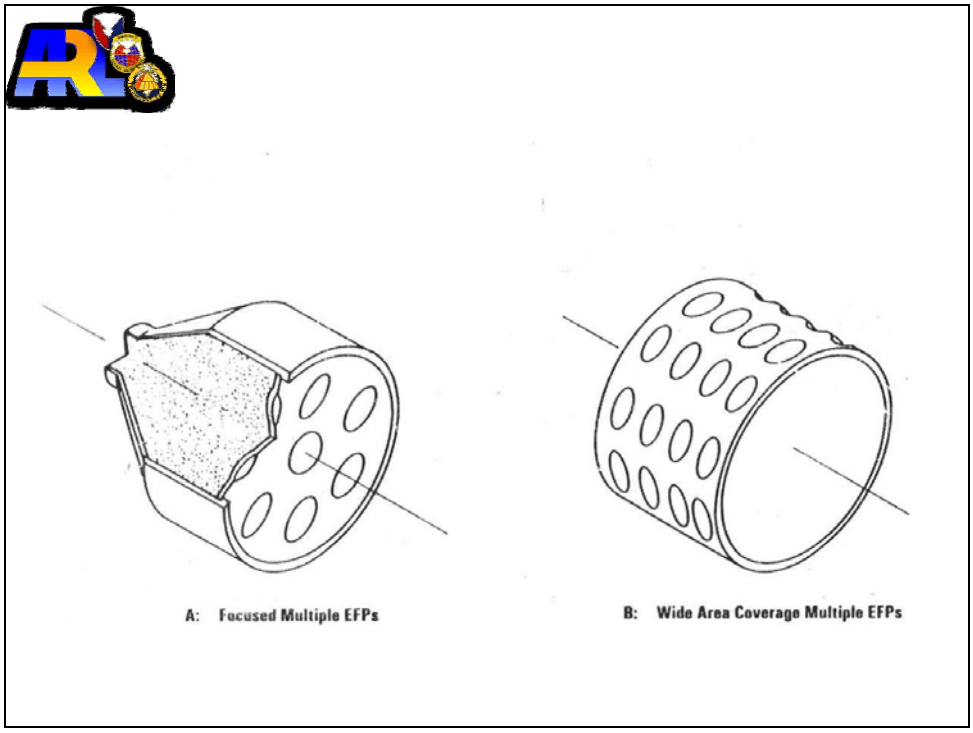

Figure 129. Multiple liner concepts.

Face Centered Cubic Crystal (High ductility-good jets)			Body Centered Cubic Crystals (low ductility-chunky jets)			Hexagonal Crystals (Powder jets)		
Element	Density gm/cc	Melting Pt. °C	Element	Density gm/cc	Melting Pt. °C	Element	Density gm/cc	Melting Pt. °C
* Aluminum	2.69	660	Chromium	7.22	1890	* Beryllium	1.85	1285
* Copper	8.93	1083	*Iron	7.86	1535	Boron	2.3	2100
* Gold	18.98	1063	Lithium	0.53	186	* Cadmium	8.65	321
* Lead	11.34	327	Molybdenum	9.01	2620	* Carbon	2.2	3704
* Nickel	8.80	1455	Tantalum	16.6	2996	* Cobalt	8.9	1489
* Platinum	21.37	1773	Vanadium	5.96	1710	* Magnesium	1.74	651
* Silver	10.42	960				Osmium	22.48	2700
Tungsten (Beta)	19.30	3770				* Titanium	4.5	1800
						* Zinc	7.14	419.5
						* Zirconium	6.43	1700

Mixtures

Antimony - lead
Glass
Aluminum - zinc
Aluminum - copper
Zirconium - tin

* Known to have been experimentally investigated

Figure 130. Liner materials studied at the U.S. Army Ballistic Research Laboratory (BRL)/ARL.

FCC	BCC	HCP	ORTHO.	AMORPHOUS
Al	Fe	Be	U	Cu-9Y
Ca	Nb	Mg		DU-20Ni
Ni	Mo	Ti		
Cu	Ta	Zn		
Ag	W	Zr		
Au	V	Co		
Pb	Cr	Cd		

Figure 131. Shaped-charge liner material as a function of crystal structure.

- Cu, Ni, Al, Ag, Au form coherent, ductile jets.

- Ni somewhat difficult to fabricate, performance has been inconsistent.

- Pb can form fluid jets.

Figure 132. Face-centered cubic (FCC).

- Ta, Mo, and W all form coherent and ductile jets when properly designed.

- W jets are somewhat less ductile than Mo or Ta and can exhibit brittle fracture on some parts of the jet surface. The proper jet conditions for W have not been completely defined.

Figure 133. Body-centered cubic (BCC).

Multiphase	Solid Solution	Eutectic	Eutectoid	Pressed/Sintered
95Cu-5Al	90Cu-10Ni	38Pb-62Sn	78Zn-22Al	90W-7Ni-3Fe
90Cu-10Sn	70Cu-30Ni	89Pb-11Sb		78W-22Cu
90Cu-10Zn	50Cu-50Ni	28Cu-72Ag		70W-30Cu
70Cu-30Zn	30Cu-70Ni			
304 SS				
IN-744				

Figure 134. Alloys tested as shaped-charge liners.

- Useful for special applications. Be can produce very high velocity but low mass jets. Mg and Zr exhibit incendiary effects.

Figure 135. Hexagonal close packed (HCP).

- DU provides an excellent jet with the proper design and appropriate treatment of its anisotropic properties.

Figure 136. Orthorhombic (Ortho).

- Multielement alloys, made by a press or sintering process or by sputter deposition.

- Cu-Y and DU-Ni tested in conical and hemispherical geometries.

- Cu-Y in a conical geometry yielded a continuous stream of very fine particles. In a hemispherical shape, the jet was highly ductile with a long breakup.

- DU-Ni liners from conical and hemispherical geometries gave a continuous, nonparticulating jet.

Figure 137. Amorphous.

- Do not perform as well or as consistently as pure metal liners.

- Multiphase liners are the worst; jets are incoherent and fragment early.

- Solid solution liners can form coherent jets but are not as ductile and perform worse than their pure metal constituents.

Figure 138. Alloys.

- Eutectic alloy jets are usually continuous and nonparticulating. They have produced very good penetration into steel targets at normal obliquity. They may be fluid ad susceptible to destruction by oblique targets. The jets were highly variable in quality ad penetration.

Figure 139. Alloys (continued).

- **The only eutectoid tested (78Zn-22A1 and variants) has not produced good quality jets. This alloy is superplastic with a submicrometer microstructure. In conical liners, the jet forms a steam of brittle particles that tend to disperse radially. In a hemispherical geometry, the jets are more continuous, but neither geometry produces a high-performance jet.**
- **Pressed or sintered liners produce a continuous jet of fine particles, but the jet tends to disperse radially at long standoff distances. There is also a degree of variability in the jet quality and charge performance.**

Figure 140. Alloys (continued).

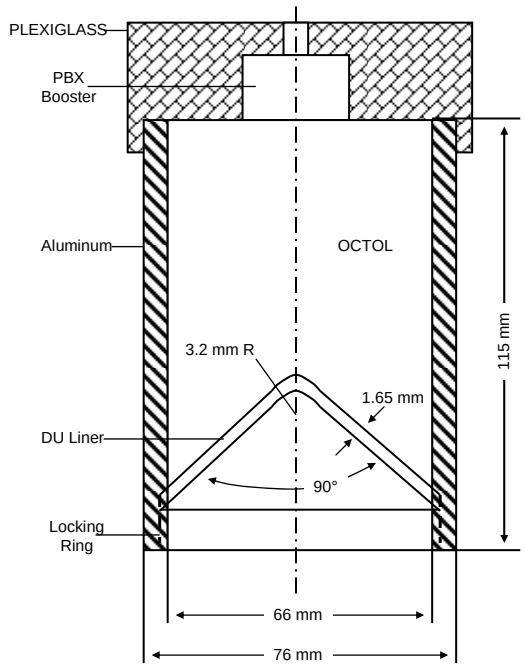

Figure 141. Configuration of depleted uranium alloy charges.

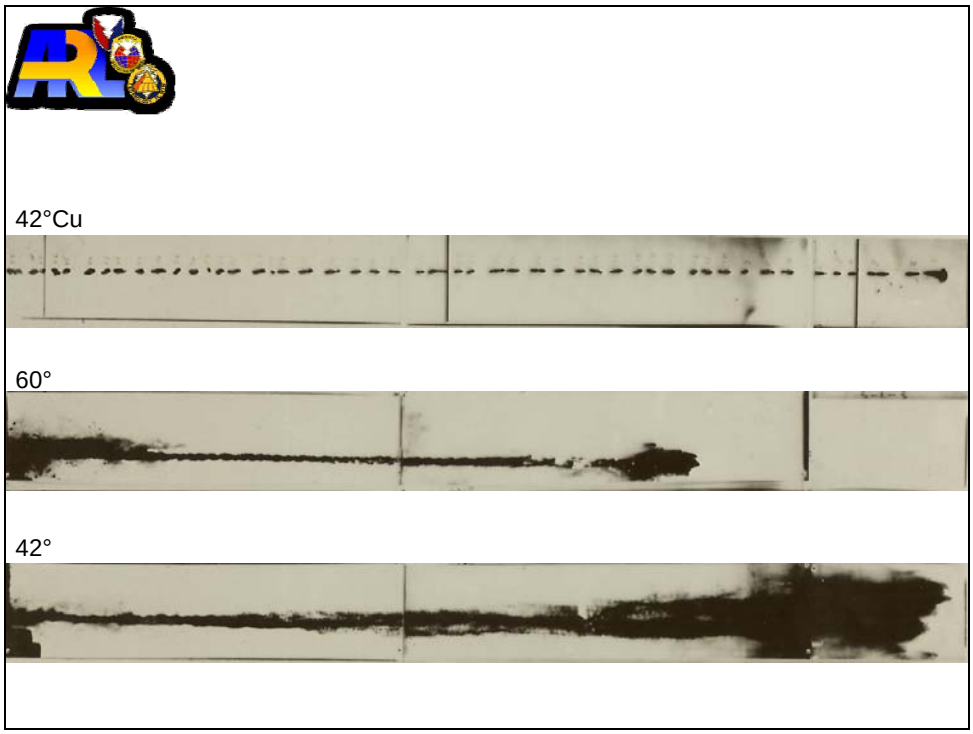

Figure 142. Free-flight radiograph of depleted uranium liners compared to copper (cone angles indicated).

Figure 143. Early time collapse of a hemispherical depleted uranium liner.

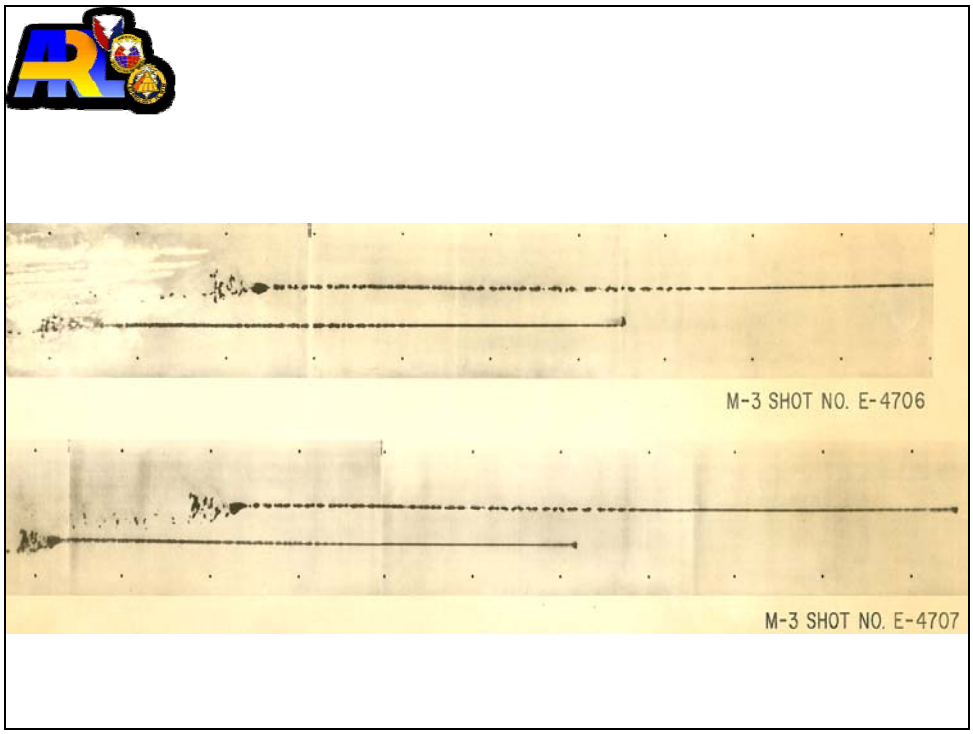

Figure 144. Late time collapse of a hemispherical depleted uranium liner.

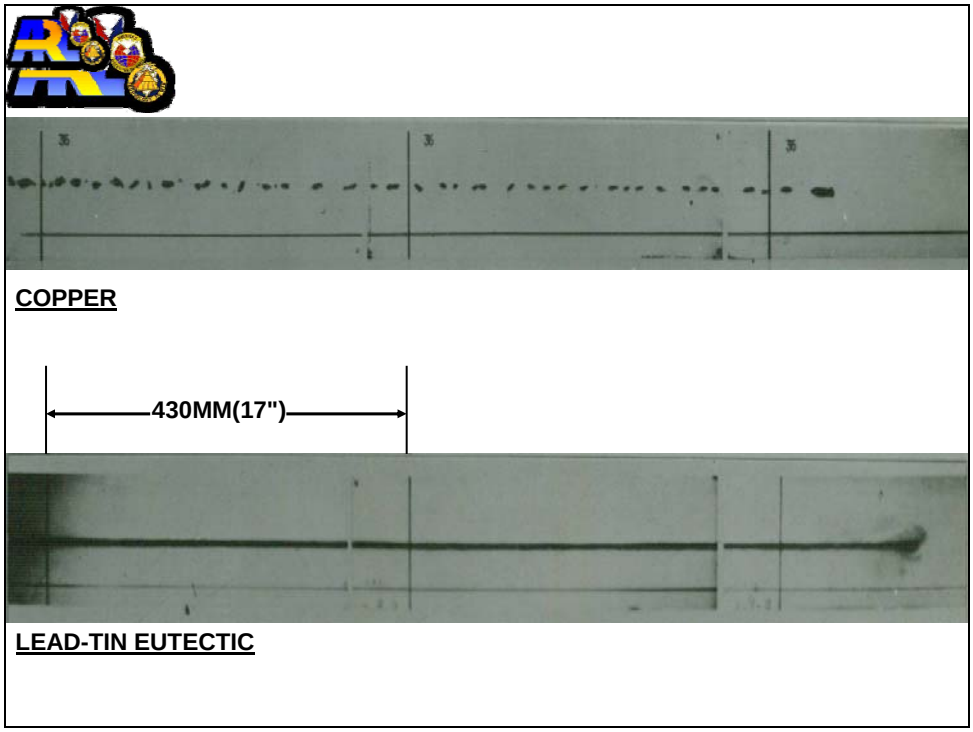

Figure 145. Comparison between a copper and a lead-tin eutectic liner.

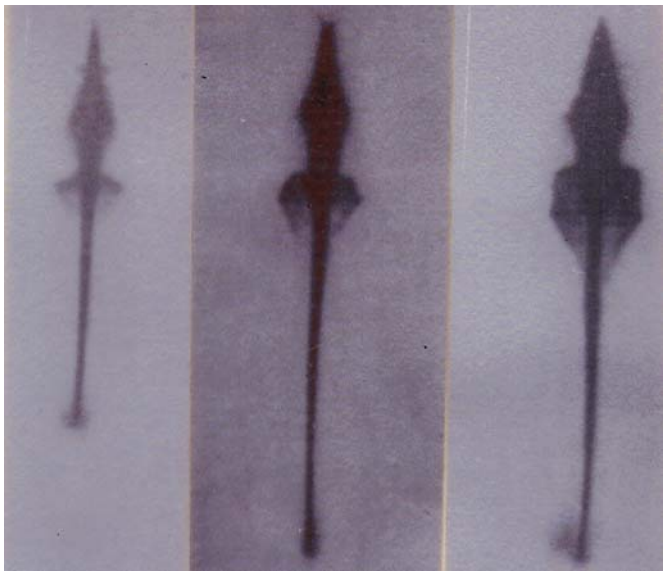

.030" wall .060" wall .090" wall

Figure 146. Flash radiographs of 60° pure cadmium liners of varied wall thickness, 25 µs after detonation wave reached apex.

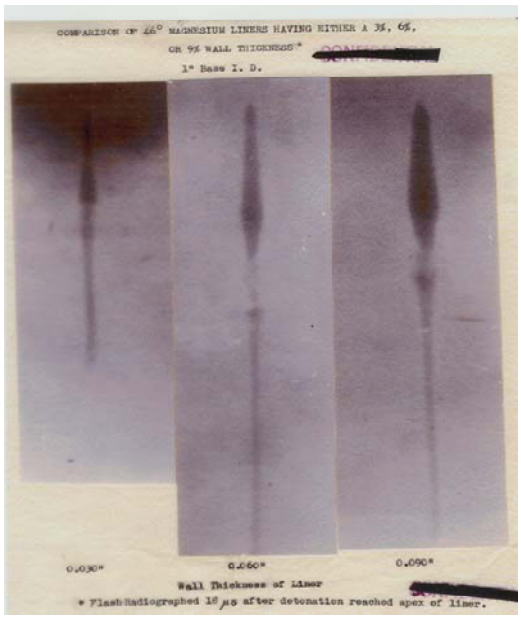

Figure 147. Flash radiographs of 44° pure magnesium liners of varied wall thickness.

Jet Velocity (km/sec) / Break-up Time (μsec)

Explosive		Liner (42°, 81mm)	
	Detonation Velocity, km/s	Coarse Grained ETP Deep Drawn ~ 100μm	Fine Grained OFHC Deep Drawn ~ 25μm
Comp B 150μ RDX	7.92	7.7/116	7.8/154
RX-08-FO 60μ HMX, NP	8.06	— —	8.0/157
RX-08-GB 8μ HMX, FEFO	8.24	— —	8.3/167
RX-08-GG 60μ HMX, FEFO	8.24	— —	8.1/173
OCTOL 75/25 470μ HMX	8.48	8.5/122	8.5/174
RX-08-EL 60μ HMX, FEFO	8.51	8.8/122	8.6/173

Figure 148. Metallurgical and explosive effects on jets.

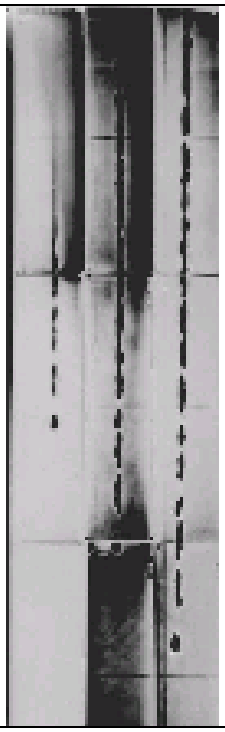

Figure 149. Oxygen-free high-conductivity copper.

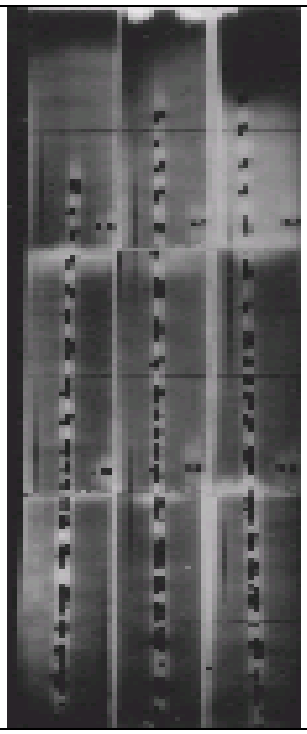

Figure 150. Electrolytic tough-pitch copper.

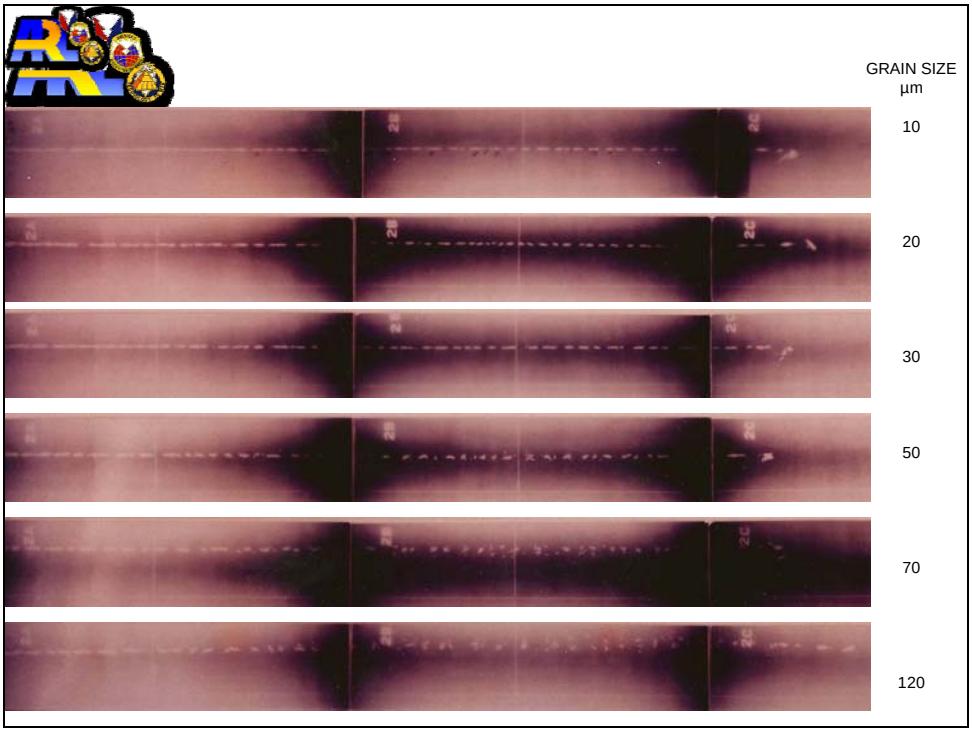

Figure 151. The effect of liner grain size on jet breakup (liner 105-mm M456, modified to BRL 81 dimensions).

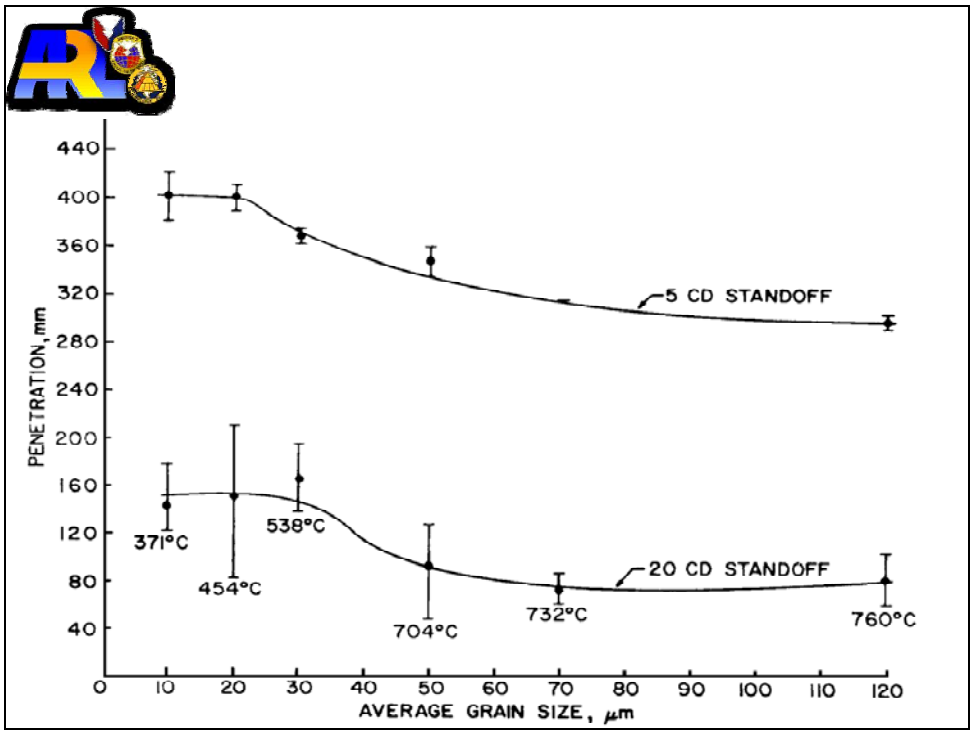

Figure 152. Effect of liner grain size on jet penetration (M456/BRL 81 mm).

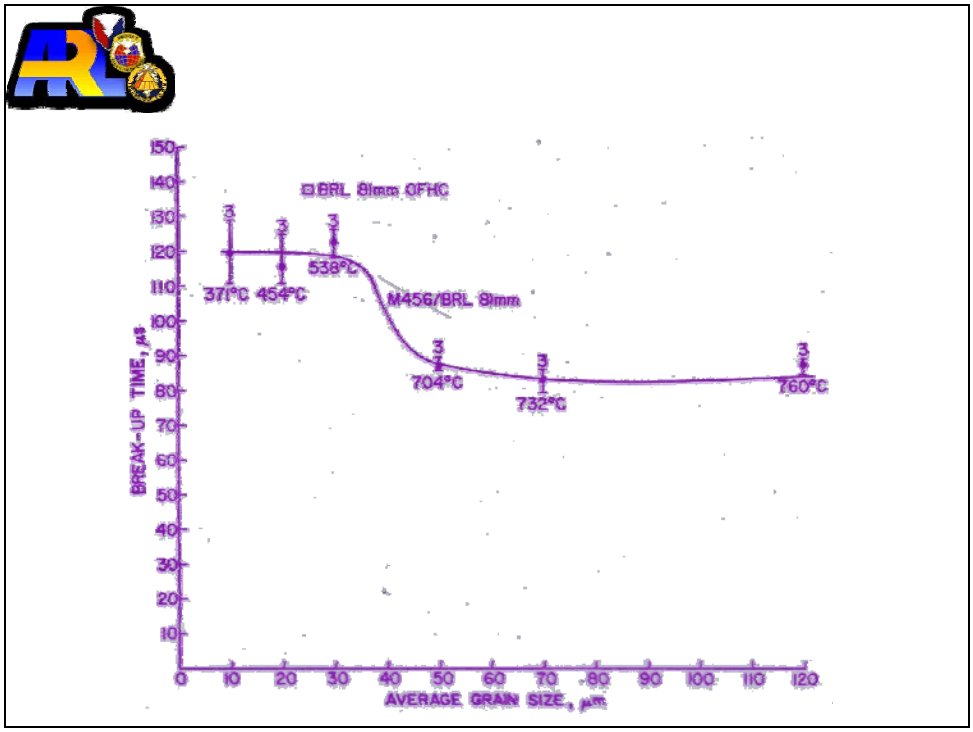

Figure 153. Effect of liner grain size on jet breakup time.

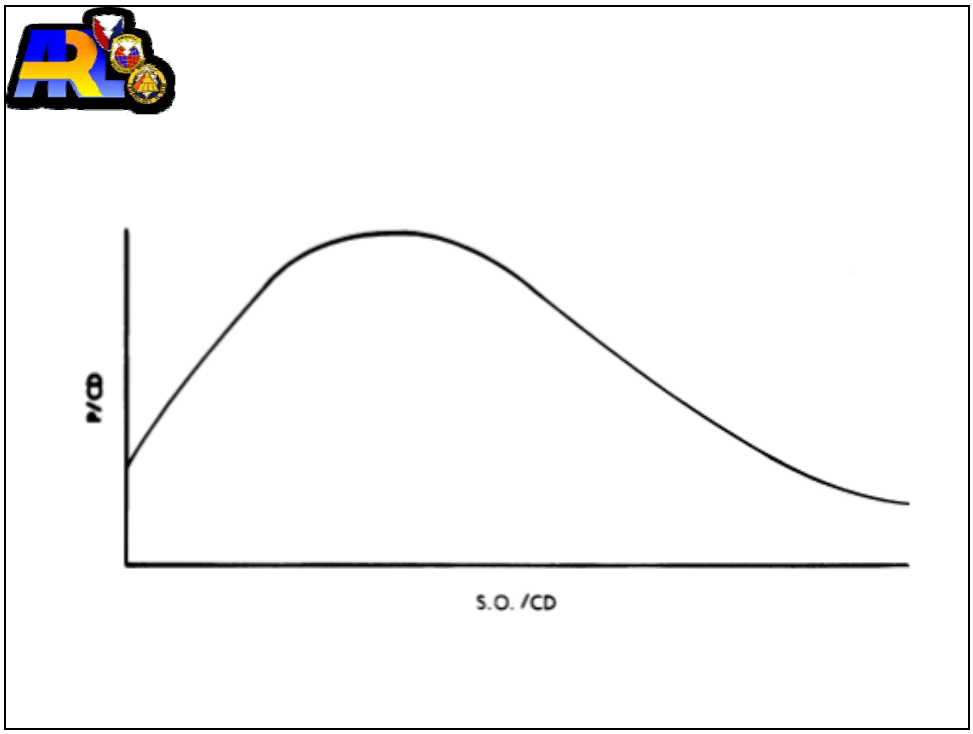

Figure 154. Penetration standoff curve.

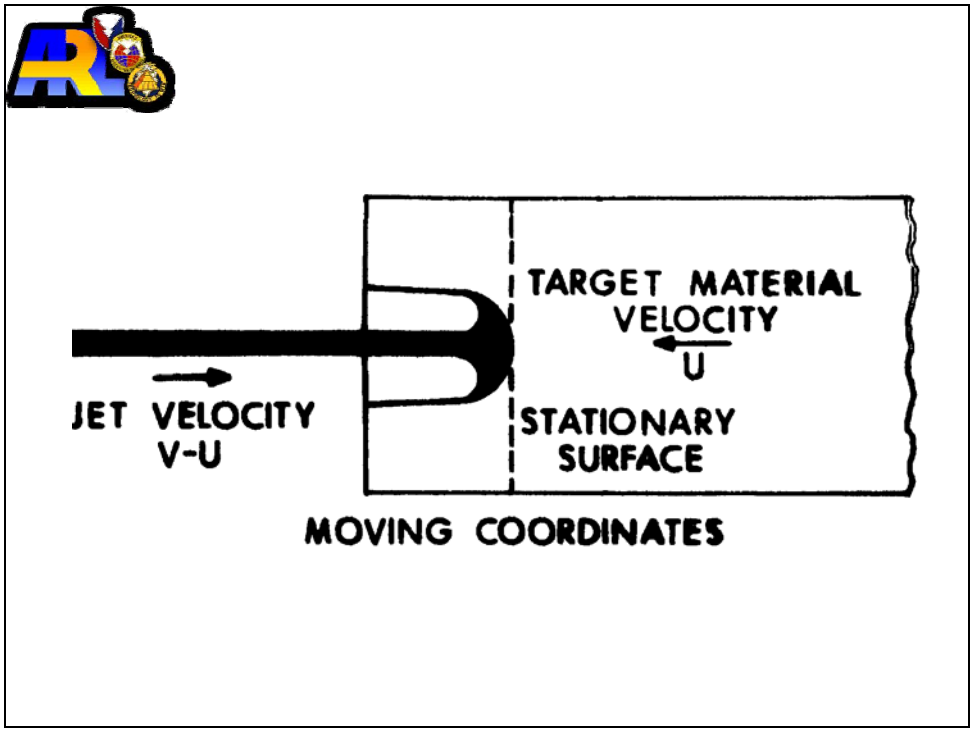

Figure 155. The coordinate system.

$$-\dot{u} \sim a + bu + cu^2$$

FOR BOTH CONSTANT VELOCITY PENETRATORS OR NON-ERODING PENETRATORS

ROBINS / EULER	$-\dot{u} \sim a$
PONCELET / EULER	$-\dot{u} \sim cu^2 + a$
RESAL	$-\dot{u} \sim cu^2 + bu$
GENERAL FORM / JOHNSON	$-\dot{u} \sim a + bu + cu^2$

Figure 156. Penetration formulations.

$$\frac{1}{2} \rho_j (V - U)^2 = \frac{1}{2} \rho_T U^2$$

Figure 157. Bernoulli's equation for coordinates moving at velocity U.

$$\frac{\ell}{V - U}$$

$$P = U \frac{\ell}{V - U} \text{ or,}$$

$$P = \ell (\rho_j / \rho_T)^{\frac{1}{2}}$$

Figure 158. Ideal penetration time (penetration stops as soon as the rear of the jet hits the target).

$$F/A = \rho_j (V - U)^2$$

PRESSURE IN TARGET MATERIAL AT POINT OF IMPACT =

$$\frac{1}{2} \rho_T U^2$$

Figure 159. Momentum equation.

$$\rho_j \, (V - U)^2 = \frac{1}{2} \rho_T \, U^2$$

Figure 160. Equating the two expressions.

THEN

$$P = \ell \left(\frac{\lambda \rho_j}{\rho_T} \right)^{1/2}$$

Figure 161. The penetration.

EICHELBERGER PROPOSED

$$\lambda \rho_j (V - U)^2 = \rho_t U^2 + 2\sigma$$

WHERE $\sigma = \sigma_t - \sigma_j$

Figure 162. Eichelberger's equation.

$$\lambda \rho_j (V-U)^2 = \rho_t U^2 + 2\sigma$$

$\lambda = 1$ for continuous jet

$\lambda < 1$ for broken jet

$$\sigma = \sigma_t - \sigma_j$$

where

σ_t and σ_j are the "resistance to plastic deformation" for the target and the jet; taken as

$$Y_t < \sigma_t < 3\, Y_t$$

Y_t is the yield strength of the target

Figure 163. Eichelberger's formula.

$$P = P_o' \left[\sqrt{2}\,(1 + \alpha S)^{\frac{1}{2}} / (1 + \beta S) \right]$$

P_o' IS P FROM BEFORE AT S = JET BREAKUP DISTANCE.

Figure 164. For fully particulated jets.

α ACCOUNTS FOR JET VELOCITY GRADIENT

S DENOTES STANDOFF

β ACCOUNTS FOR JET SPREAD

$$P = P_o \; (1 + \alpha S)/(1 + \beta S)$$

Figure 165. Semi-empirical models.

PACK AND EVANS TOOK TARGET MATERIAL STRENGTH INTO ACCOUNT

$$P = \left(\frac{\rho_j}{\rho_t}\right)^{1/2} L \left(1 - \frac{\alpha Y}{\rho_j V^2}\right)$$

Figure 166. Pack and Evans.

FOR PARTICULATED JETS, CHOU USES

$$dP' = dP \left(1 - \frac{g}{g_o}\right)$$

g IS THE DISTANCE BETWEEN PARTICLES,

and g_o = 6.5 FOR PRECISION CHARGES

= 4 TO 6 FOR NON-PRECISION CHARGES

Figure 167. Chou.

MATUSKA, FOR STEADY STATE JET PENETRATION USED,

$$\frac{\gamma}{2} \rho_j (V - U)^2 + \beta \sigma_j = \frac{\rho_t U^2}{2} + \alpha \sigma_t$$

Figure 168. Matuska.

ALEKSEEVSKII,

SANASARYAN, AND

SAGOMONYAN USE

$$H_D + k_T \rho_T U^2 = \sigma_{SD} + k_j \rho_j (V - U)^2$$

WHERE $k_T = k_j = 1/2$ AND

$$V_{min} = \sqrt{\frac{H_D - \sigma_{SD}}{k_j \rho_j}}$$

Figure 169. Alekseevski, Sanasaryan, and Sagomonyan.

CHRISTMAN AND GEHRING PROPOSED

$(2 < V < 6.7 \text{ km/s})$

$$\frac{P}{L} = \left(1 - \frac{D}{L}\right)\left(\frac{\rho_p}{\rho_t}\right)^{1/2} + 2.42\,\frac{D}{L}\left(\frac{\rho_p}{\rho_t}\right)^{2/3}\left(\frac{\rho_t\,V^2}{B_{max}}\right)^{1/3}$$

FOR PROJECTILES

Figure 170. Christman and Gehring.

DOYLE AND BUCHHOLZ MODIFIED THE CHRISTMAN-GEHRING FORMULA FOR EFP'S

$$\frac{P}{L} = \left(1 - \frac{D}{L}\right)\left(\frac{\rho_p}{\rho_t}\right)^{1/2} + \frac{0.13}{L}\left(\frac{\rho_p}{\rho_t}\right)^{1/3}\left(\frac{E_1}{B_{max}}\right)^{1/3}$$

Figure 171. Doyle and Buchholz.

For case (a), the total penetration depth *P* is

$$P = S\left[\left(\frac{V_0}{V_{\min}}\right)^{1/\gamma} - 1\right]$$

where *S* is the distance from the virtual origin to the target, or the effective standoff distance. In this case *S* is bounded by

$$0 \le S < V_{\min} t_b \left(\frac{V_{\min}}{V_0}\right)^{1/\gamma}$$

and

$$U_{\min} = \frac{V_{\min}}{1+\gamma}$$

Figure 172. The DiPersio, Simon, Merendino model.

For case (b), the penetration is

$$P = \frac{(1+\gamma)(V_0 t_b)^{1/(1+\gamma)} S^{\gamma/(1+\gamma)} - V_{\min} t_b}{\gamma} - S$$

where *S* is bounded by

$$V_{\min} t_b \left(\frac{V_{\min}}{V_0}\right)^{1/\gamma} < S < V_0 t_b$$

Figure 173. The DiPersio, Simon, Merendino model (continued).

Finally, for case (c), the penetration is

$$P = \frac{(V_0 - V_{\min})t_b}{\gamma}$$

for standoffs in the range given by

$$V_0 t_b < S < \infty$$

Recall that

$$\gamma = \sqrt{\rho_T / \rho_j}$$

Figure 174. The DiPersio, Simon, Merendino model (continued).

For case (a),

$$P = S\left[\left(\frac{V_0}{(1+\gamma)U_{\min}}\right)^{1/\gamma} - 1\right]$$

S is bounded by

$$0 \le S < (1+\gamma)U_{\min} t_b \left[\frac{(1+\gamma)U_{\min}}{V_0}\right]^{1/\gamma}$$

Figure 175. The DiPersio, Simon, Merendino model (continued).

For case (b), the penetration is now

$$P = \frac{(1+\gamma)(V_0 t_b)^{1/(1+\gamma)} S^{\gamma/(1+\gamma)} - \sqrt{(1+\gamma)U_{\min} t_b (V_0 t_b)^{1/(1+\gamma)} S^{\gamma/(1+\gamma)}}}{\gamma} - S$$

where *S* ranges from

$$(1+\gamma)U_{\min} t_b \left[\frac{(1+\gamma)U_{\min}}{V_0}\right]^{1/\gamma} < S < V_0 t_b$$

Figure 176. The DiPersio, Simon, Merendino model (continued).

For case (c), when the jet particulates before penetration begins,

$$P = \frac{V_0 t_b - \sqrt{U_{\min} t_b (V_0 t_b + \gamma S)}}{\gamma}$$

where *S* lies in the interval

$$V_0 t_b < S \le \frac{V_0 t_b}{\gamma}\left(\frac{V_0 - U_{\min}}{U_{\min}}\right)$$

Figure 177. The DiPersio, Simon, Merendino model (continued).

$$(\rho_P/2)(v-u)^2 + Y_P = (\rho_T/2)u^2 + R_T$$

$$\frac{dv}{dt} = \frac{-Y_P}{l\rho_P}$$

$$\frac{dl}{dt} = u - v$$

$$u = \frac{dp}{dt} \qquad \text{or} \qquad p = \int u dt$$

Where:

v *is the penetrator velocity,*
$\boldsymbol{\rho_P}$ *is the penetrator density,*
$\boldsymbol{Y_p}$ *is the penetrator strength term,*
l *is the instantaneous penetrator length,*

u *is the penetration velocity*
$\boldsymbol{\rho_T}$ *is the target density*
$\boldsymbol{R_T}$ *is the target strength term*
t *is time*

Figure 178. The Tate model.

$$\frac{d}{dt}(M\,U) = \pi r_{min}^2\,[\sigma - \sigma_T] + \pi r_{min}^2\,\rho(t)(V - U)^2$$

$$- \pi r_{min}^2 \rho_{To}\,U^2 - 2\,\pi\,\mu\,U\,(H_o + P_p),$$

where $M = \pi r_{min}^2\,(P_p + H_o)\,\rho(t)$.

Figure 179. The Walters and Majerus model.

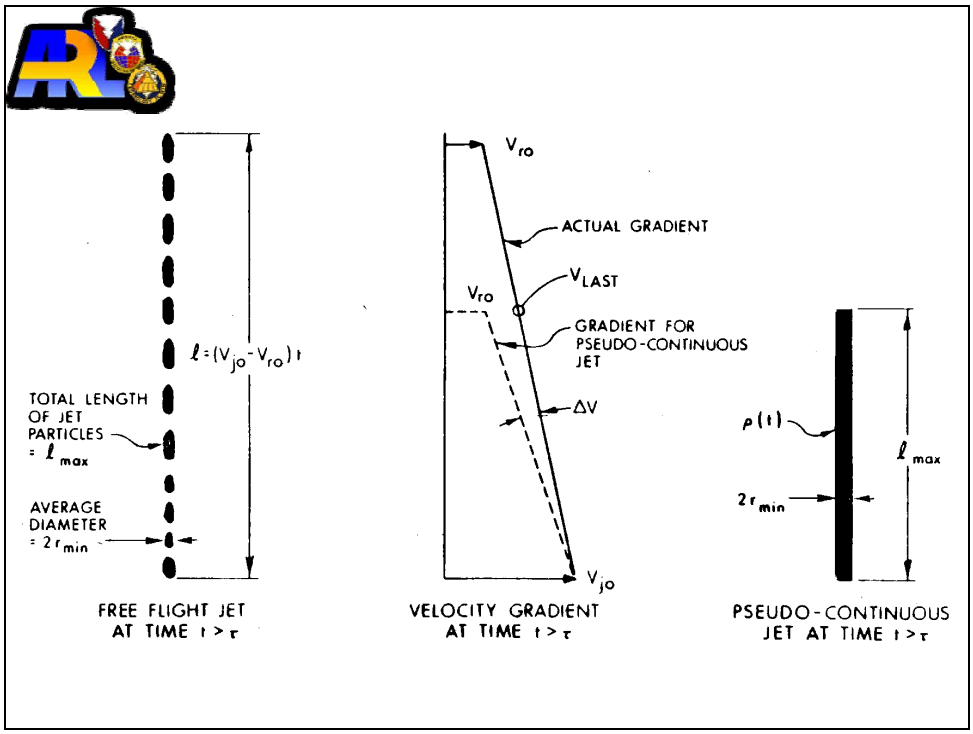

Figure 180. The Walters and Majerus model (continued).

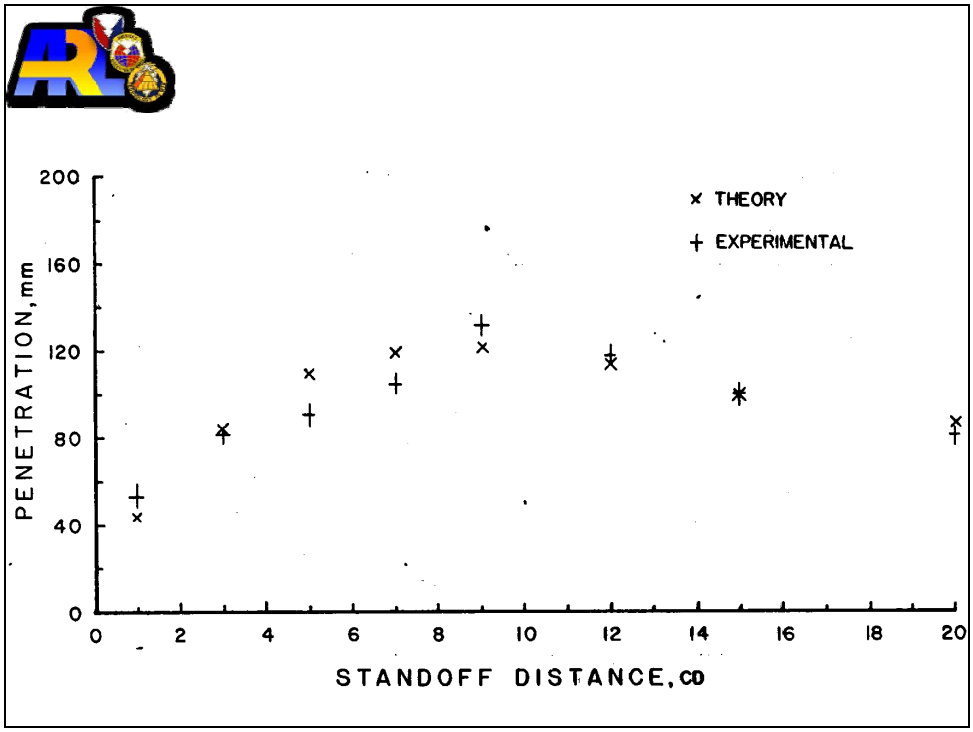

Figure 181. Analytical and experimental penetration vs. standoff curve for aluminum jet impacting a steel target.

Target Thick. (mm)	Mat.	Standoff Distance (LD)	Exit Velocities (km/s) Experimental				Avg.	Calc.	Percent* Diff.
25	RHA	2		6.79			6.79	6.92	1.9
38			6.68	6.61	6.62		6.64	6.64	0
76			6.05	5.99	6.01	5.91	5.99	5.90	-1.5
152			4.91	4.90	4.86	4.81	4.87	4.84	-0.6
191			4.42	4.38	4.28	4.36	4.36	4.43	1.6
51	GRP	2	7.01	6.98			6.99	7.00	0.1
254	MS	2	3.73	3.74			3.73	3.89	4.2
305			3.35	3.35			3.35	3.65	9.0
356			2.93				2.93	3.21	9.6
Target 5+		1	5.90	5.31			5.86	5.45	-7.1
6			5.01	4.90			4.96	4.93	-0.6
7			5.28	5.11			5.20	5.35	2.9

$$*\frac{CALC - AVG}{AVG} \times 100\%$$

+Multiple element targets

Figure 182. Experimental and calculated exit velocities for charge type 1.

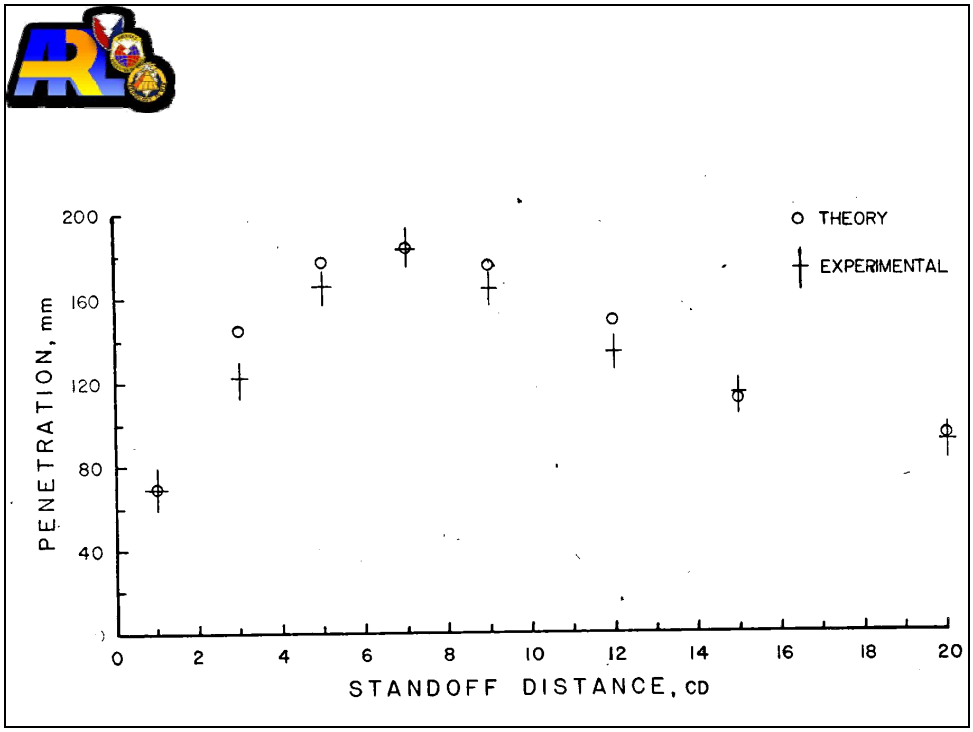

Figure 183. Analytical and experimental penetration vs. standoff curve for a copper jet impacting a steel target.

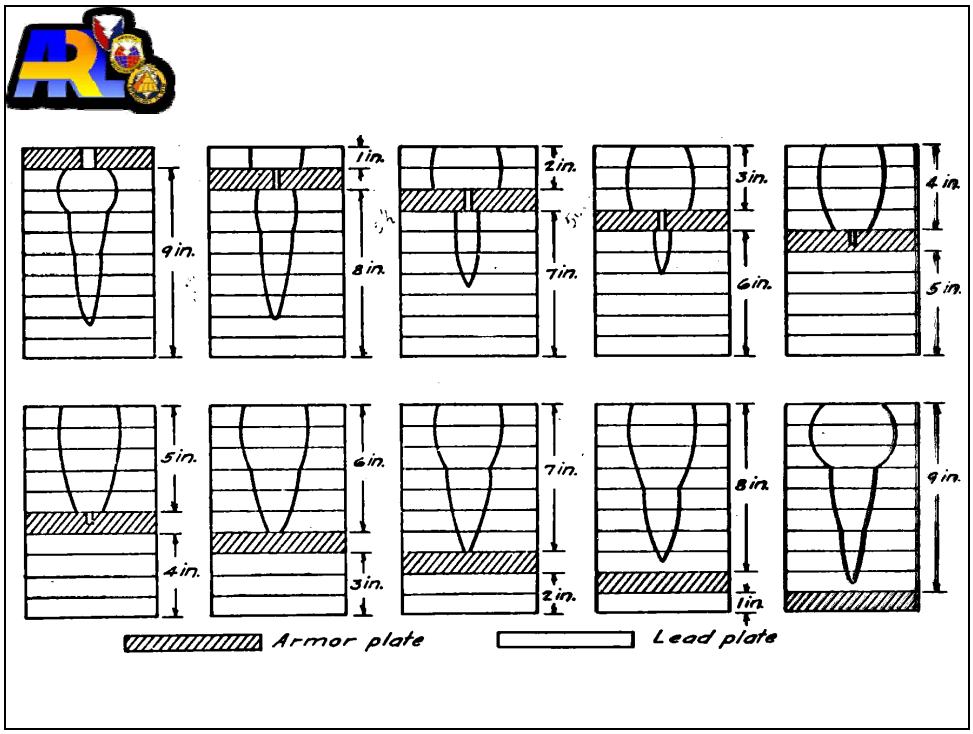

Figure 184. Hole profiles in combination lead-plate, armor-plate targets. The distance from the top of the pile to the top of the armor plate is designated A in the discussion.

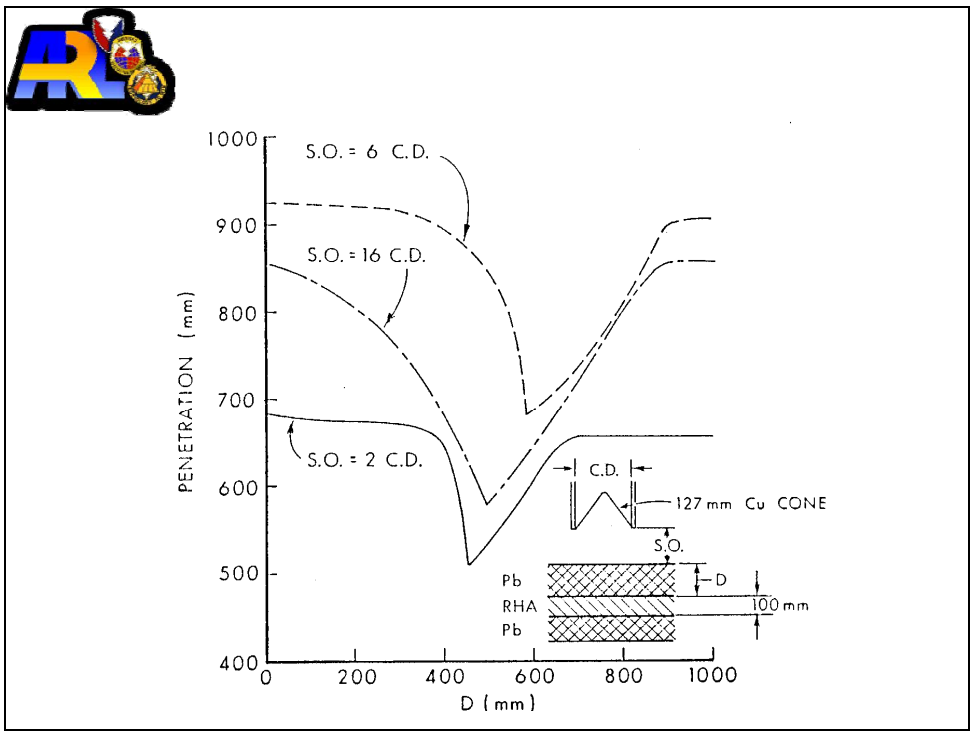

Figure 185. Predicted penetration vs. a layered target.

Metal Jets Impacting Metal Targets

- Metals have low compressibilities
- Penetration predicted well by incompressible model
- Therefore, compressibility has been neglected

Metal Jets Impacting Plastics and Liquids

- Plastics and liquids are much more compressible
- Penetration less than predicted by incompressible model
- Compressibility must be taken into account

Figure 186. Compressibility effects.

* **Jet/target density ratio** - incompressible, 1-D hydrodynamic theory states $P = L(\rho_j / \rho_t)^{1/2}$

* **Target strength** - at very high velocities, strength not important; at lower velocities, the greater the target strength, the smaller the penetration

* **Transient or unsteady effects** - interaction at start and finish of penetration process

* **Dispersion and tumbling** - jet segments and penetraters do not always follow ideal paths

Figure 187. Major factors in the penetration process.

* **Compressibility** - not important for metal targets; for highly compressible targets (e.g., Plexiglas), penetration can be 10 to 35% less than incompressible penetration

* **Rod foreshortening** - when passing through spaced armor, rods often shorten due to disturbance setup by skirting plate

* **Transverse disturbances** - certain special targets cause material to disturb the jet or penetrator laterally

Figure 188. Major factors in the penetration process (continued).

Types	Distance in ϕ	Crater		$\sum_{1}^{n}$ Volume in ϕ^3
		Depth in ϕ	Width in ϕ	
Blast Charge 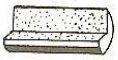	0	0.2–0.4	0.8–1.0	$\frac{0.9^2 \times \pi}{4} \times 0.3 \sim 0.19$
Hollow Charge 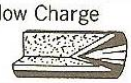	1.5–6	5–9	0.1–0.3	$\frac{0.2^2 \times \pi}{4} \times 6 \sim 0.19$
Flat Cone Charge	3–8	2–3	0.25–0.40	$\frac{0.3^2 \times \pi}{4} \times 2.7 \sim 0.19$
Projectile Charge	$1–10^3$	0.55–0.60	0.6–0.7	$\frac{0.65^2 \times \pi}{4} \times 0.57 \sim 0.19$
Fragment Charge 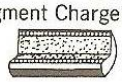	$1–10^3$	0.05–0.10	0.05–0.15	$\frac{0.10^2 \times \pi}{4} \times 0.08 \times 300 \sim 0.19$

Figure 189. Types of charges.

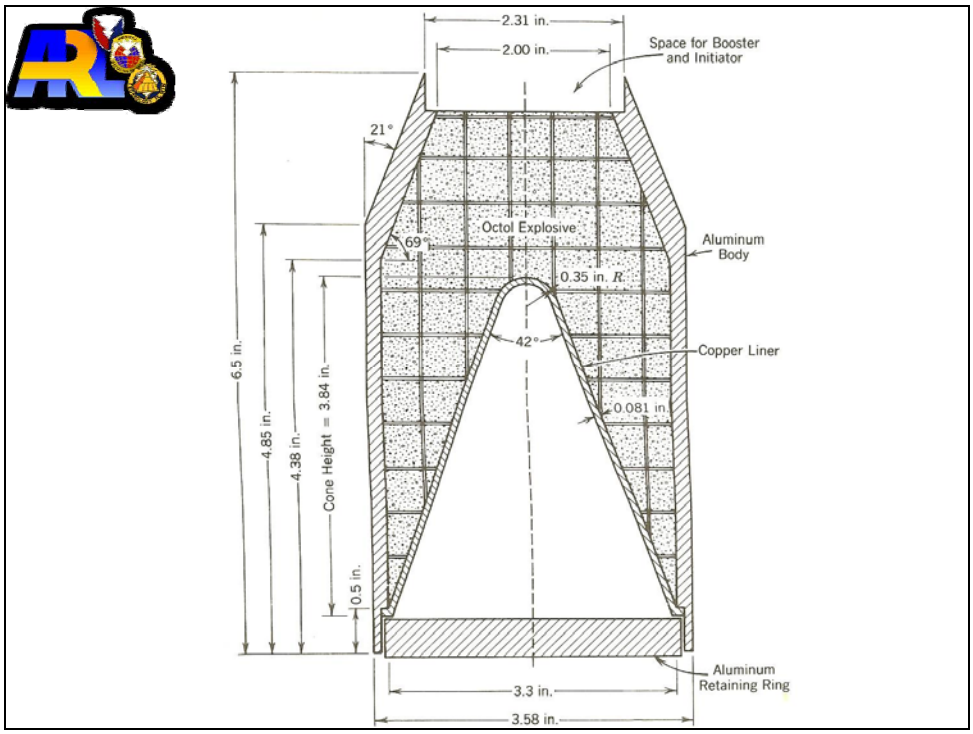

Figure 190. Diagram of standard shaped charge.

STANDARD (CD)	AVERAGE PENETRATION (CD)	MINIMUM PENETRATION (CD)	MAXIMUM PENETRATION (CD)	STANDARD DEVIATION (CD)
2	4.81 (29 SHOTS)	4.50	5.19	0.17
5	5.36 (5 SHOTS)	5.00	5.69	0.26
7	5.42 (5 SHOTS)	4.84	5.91	0.34
10	4.81 (65 SHOTS)	3.19	5.88	0.55
15	3.09 (5 SHOTS)	2.47	3.88	0.47
20	2.59 (24 SHOTS)	1.34	4.31	0.67

Figure 191. Precision shaped-charge performance.

A shaped charge requires precision in the assembly and fabrication of its components. Precision tolerances for a typical 81-mm copper cone require that the wall thickness in the transverse plane be held to ±0.0002 in, the concentricity to the casing or TIR (total indicated readout) be held to ±0.002 in, and the maximum variation in wall thickness be held to ±0.001 in. For a typical nonprecision charge of the same diameter, the wall thickness in the transverse plane has a tolerance of ±0.002 in, a concentricity (TIR) of ±0.004 in, and a maximum variation of liner wall thickness of ±0.004 in. Note that liner tolerances are not absolute but should scale with charge diameter.

Figure 192. Shaped-charge precision assembly.

Thus, for small liners, precision tolerances are difficult to achieve. These small precision tolerances are required to eliminate poor performance, especially at long standoff distances (>5 CD). The processes of jet collapse, jet formation, and penetration are strongly dependent on the maintenance of axisymmetric flow. In other words, radial velocity components must be avoided.

Figure 193. Shaped-charge precision assembly (continued).

Many aspects of shaped charge fabrication and assembly can cause radial jet velocity components. These aspects include variations of the liner wall thickness, variations in the case thickness or asymmetric confinement of the high explosive, inhomogeneities in the explosive fill, and misalignment of the liner axis with respect to the warhead axis of symmetry or the axis of symmetry of the detonation wave.

Figure 194. Shaped-charge precision assembly (continued).

	Precision Charge	Nonprecision Charge
Wall thickness variation in any liner transverse plane (in.)	0.00007	0.0043
Maximum variation in wall thickness throughout the liner (in.)	0.0010	0.0040
Concentricity of liner with casing (in.)	0.0020	0.0036

Note: The loading procedure was kept the same for both groups of charges.

Figure 195. The gauging data for the precision and nonprecision charges.

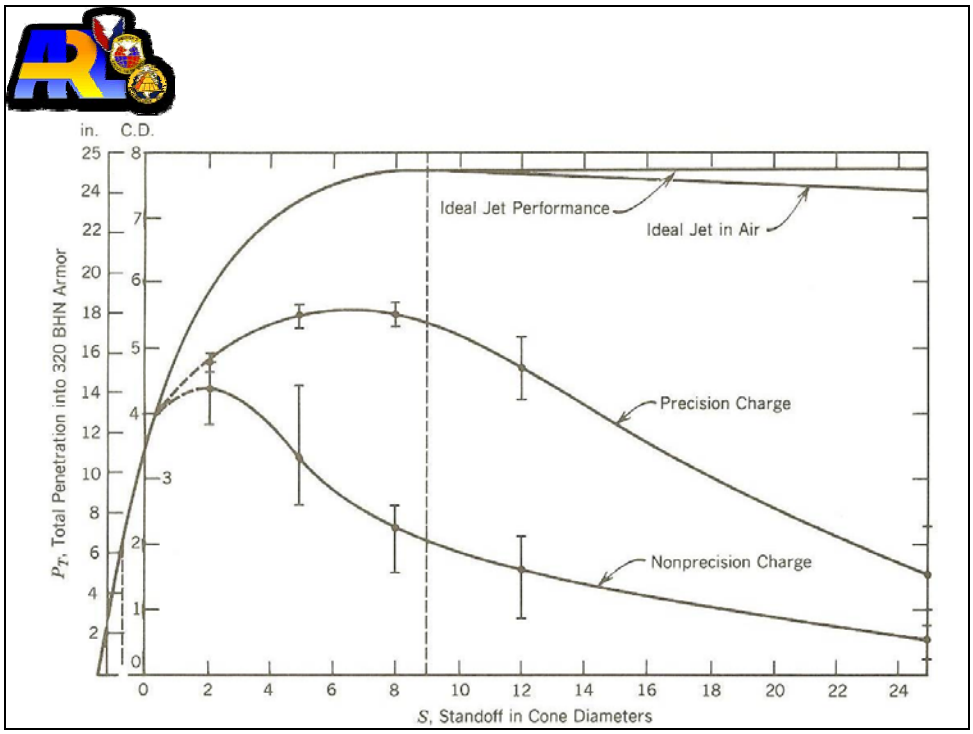

Figure 196. Penetration performance of the standard charge.

"There Is No Problem That Can't Be Solved by the Proper Application of High Explosives"

Sign in the office of Dr. J. Carleone,
Former Vice President, Aerojet Corporation

Figure 197. The solution.

Jet Velocity (km/sec) / Break-up Time (μsec)

Explosive		Liner (42°, 81mm)	
	Detonation Velocity, km/s	Coarse Grained ETP Deep Drawn ~ 100μm	Fine Grained OFHC Deep Drawn ~ 25μm
Comp B 150μ RDX	7.92	7.7/116	7.8/154
RX-08-FO 60μ HMX, NP	8.06	— —	8.0/157
RX-08-GB 8μ HMX, FEFO	8.24	— —	8.3/167
RX-08-GG 60μ HMX, FEFO	8.24	— —	8.1/173
OCTOL 75/25 470μ HMX	8.48	8.5/122	8.5/174
RX-08-EL 60μ HMX, FEFO	8.51	8.8/122	8.6/173

Figure 198. Metallurgical and explosive effects on jets.

	LX-14	PBXW-110	Octol	Comp B	Pentolite	Amatex 40	TNT
Density (g/cm^3)	1.835	1.75	1.80	1.72	1.67	1.63	1.61
Detonation rate (m/s)	8830	8480	8300	7900	7470	6900	6800
Detonation pressure (kbars)	358	315	310	268	233	194	186

From Simon and DiPersio (1971)

Figure 199. Explosive properties.

45° Conical Steel Liner

CD = LD = 4.1 cm

L = 12.5 cm

Pentolite Load

t_w = 0.094 cm

Liner Weight = 28.932g

Jet d_j = 2 - 3 mm

m_j = 5 g

V_{jo} = 7.5 km/s, V_s = 0.5 km/s

M. A. Cook, Xavier de Callatäy, R. T. Keyes, "Behavior of Metals Under Impact Loading and the Mechanism of Cratering", Explosives Research Group, Institute for the Study of Rate Processes, University of Utah, Salt Lake City, Technical Report No. II, October 15, 1956.

Figure 200. Liner description.

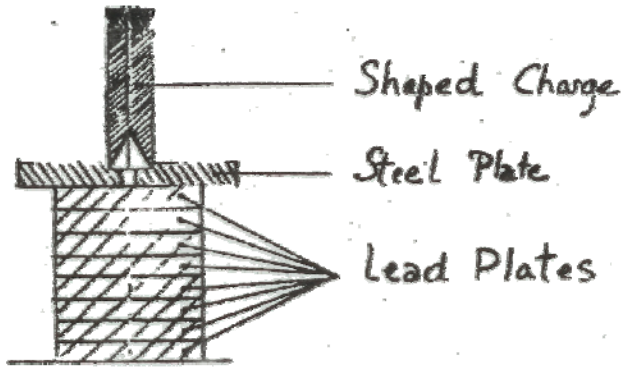

Figure 201. Disposition of a shaped charge to be fired in lead plates.

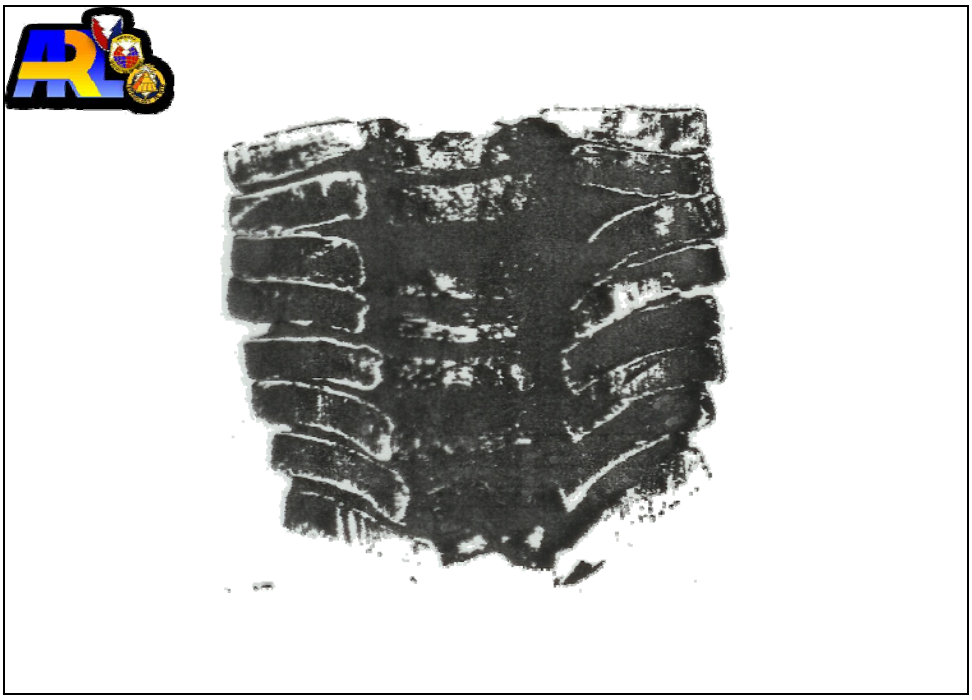

Figure 202. Photograph of a stack of lead plates penetrated by a jet from a steel conical liner. The circular plates have been cut after the firing. The 15.5-cm-diameter plates were 1.5 cm thick.

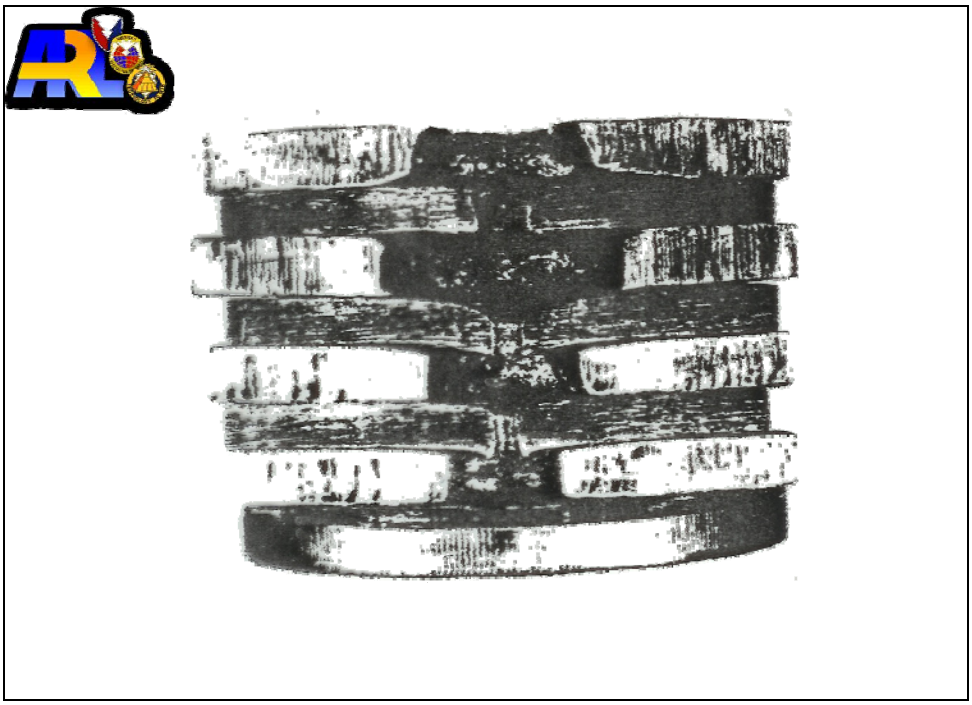

Figure 203. Photograph of a stack of plates penetrated by a jet from a steel conical liner. The circular plates, except the last one, have been cut after firing. The plates are alternately lead and steel; the top plate is lead, the next is steel, the third is lead, etc. The 15.5-cm-diameter lead plates were 1.5 cm thick; the 15.35-cm-diameter steel plates were 1.27 cm thick.

Pb Plate	Steel Plate
15.5 cm diameter	15.35 cm diameter
x 1.5 cm	x 1.27 cm
ρ = 11.35 g/cc	ρ = 7.8 g/cc
M = 3212.48 g	M = 1833.18g
In all Pb target	In Pb/S/Pb/S...target
1st plate lost 27.7g 2nd plate lost 7.0g	1st Pb plate lost 30g 2nd Pb plate lost 5.2g
No other mass loss	No steel mass lost, no other Pb mass lost

Figure 204. Plate mass loss.

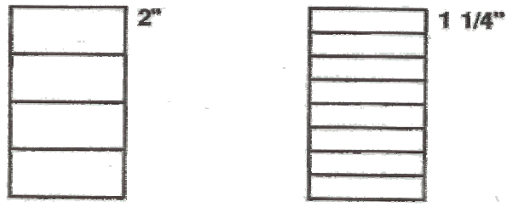

M 42 @ BISO (0.72")

FTR	
$\bar{P}$ = 2.76" (2.7 - 2.85)	$\bar{P}$ = 2.62" (2.55 - 2.70)
Ramal	
$\bar{P}$ = 2.79" (2.7 - 2.88)	$\bar{P}$ = 2.58" (2.55 - 2.63)

(5 Shot Average)

Figure 205. Thin vs. thick plates.

Element	ρ (g/cm³)	C_o (km/s)	T_m (°C)
Al (24ST)	2.79	5.35	660
Cu	8.9	3.96	1082
Fe	7.86	3.82	1535
Pb	11.34	2.03	327
Au	19.3	3.08	1063
Ag	10.5	3.24	960
Ni	8.9	4.65	1455
Co	8.9	4.75	1495
Cd	8.6	2.44	320

Figure 206. Materials table.

Element	ρ (g/cm³)	C_o (km/s)	T_m (°C)
Sn	7.28	2.64	232
Ta	16.6	3.37	2996
W	19.3	4.01	3370
U	18.95	2.49	1133
Mg	1.74	4.49	651
Zn	7.14	3.05	419
Zr	6.4	3.77	1857
Be	1.8	7.98	1278
Pt	21.4	3.67	1774
Mo	10.2	5.16	2620

Figure 207. Materials table (continued).

- HIGH MELT TEMPERTURE
- HIGH DENSITY
- HIGH SOUND SPEED
- FINE GRAIN, PROPER GRAIN ORIENTATION, GOOD ELONGATION
- AVAILABILITY

Figure 208. Favorable characteristics of shaped-charge liner materials.

- CHEAP
- EASY TO FABRICATE
- NON-TOXIC
- HIGH DYNAMIC STRENGTH

Figure 209. Favorable characteristics of shaped-charge jet materials.

- Jet tip velocity and jet tail velocity
- Velocity gradient
- Breakup time or breakup time distribution
- Jet diameter
- Jet length

Figure 210. Shaped-charge jet parameters.

- Ductile
- Coherent
- Straight
- Massive
- Fast

Figure 211. Favorable jet characteristics.

- High strength
- Favorable velocity gradient
- Long breakup time
- Special conditions (spaced, large tip, etc.)

Figure 212. Favorable jet characteristics (continued).

NO. OF COPIES	ORGANIZATION
1 (PDF ONLY)	DEFENSE TECHNICAL INFORMATION CTR DTIC OCA 8725 JOHN J KINGMAN RD STE 0944 FORT BELVOIR VA 22060-6218
1	US ARMY RSRCH DEV & ENGRG CMD SYSTEMS OF SYSTEMS INTEGRATION AMSRD SS T 6000 6TH ST STE 100 FORT BELVOIR VA 22060-5608
1	DIRECTOR US ARMY RESEARCH LAB IMNE ALC IMS 2800 POWDER MILL RD ADELPHI MD 20783-1197
3	DIRECTOR US ARMY RESEARCH LAB AMSRD ARL CI OK TL 2800 POWDER MILL RD ADELPHI MD 20783-1197

ABERDEEN PROVING GROUND

1	DIR USARL AMSRD ARL CI OK TP (BLDG 4600)

NO. OF COPIES	ORGANIZATION
105	DIR USARL
	AMSRD ARL WM BA
	G BROWN
	AMSRD ARL WM BC
	I CELMINS
	M CHEN
	S SILTON
	AMSRD ARL WM BD
	E BYRD
	J CIEZAK
	W MATTSON
	C MUNSON
	S HOWARD
	J SCHMIDT
	AMSRD ARL WM BF
	P BUTLER
	C PATTERSON
	AMSRD ARL WM MA
	A BUJANDA
	C HUBBARD
	R JENSEN
	W KOSIK
	D OBRIEN
	J SNYDER
	M VANLANDINGHAM
	AMSRD ARL WM MB
	K CHO
	R EMERSON
	D GRAY
	L KECSKES
	H MAUPIN
	M MINNICINO
	B POWERS
	D SNOHA
	AMSRD ARL WM MC
	R ADLER
	C MILLER
	B PLACZANKIS
	P SMITH
	AMSRD ARL WM MD
	J CAMPBELL
	K DOHERTY
	C FOUNTZOULAS
	S GHIORSE
	P HUANG
	M KLUSEWITZ
	J MONTGOMERY
	J SANDS
	B SCOTT
	D SPAGNUOLO
	S WALSH
	AMSRD ARL WM T
	P BAKER

NO. OF COPIES	ORGANIZATION
	AMSRD ARL WM TA
	V HERNANDEZ
	T JONES
	D LITTLE
	M LOVE
	S HUG
	AMSRD ARL WM TB
	R EHLERS
	B KRZEWINSKI
	B MCANDREW
	N MEHTA
	T PIEHLER
	AMSRD ARL WM TC
	N BRUCHEY
	T EHLERS
	H RICGESTER
	D WEEKS
	R COATES
	W WALTERS (10 CPS)
	AMSRD ARL WM TD
	D CASEM
	Y HUANG
	AMSRD ARL WM TE
	T KOTTKE
	AMSRD ARL SL
	J FEENEY
	AMSRD ARL SL BB
	N HUTTON
	C KUHNS
	M ROTHWELL
	C STANCOFF
	P WILLARD
	B YOUNG
	L BOMBOY
	AMSRD ARL SL BD
	T HOLDREN
	E SNYDER
	A DRYSDALE
	D LOWRY
	B MILLS
	T POANDL
	J VALEK
	AMSRD ARL SL BE
	S ALMOURADI
	G DIETRICH
	L DOUGHERTY
	J GREENBERG
	P HORTON
	R VALENTINE
	AMSRD ARL SL BM
	C BARKER
	D CARABETTA
	D FARENWALD

NO. OF COPIES	ORGANIZATION
	P FEDELE
	R GANGLER
	T MAK
	K MANNIX
	M OMALLEY
	A VOGT
	B WOLFE
	AMSRD ARL SL BS
	J AUTEN
	M MAR
	AMSRD ARL SL EM
	C GARRETT